Thermal Management of a High Efficiency Electrical Energy Conversion Unit

A Thesis

Presented in Partial Fulfillment of the Requirements for the

Degree of Master of Science

with a

Major in Chemical Engineering

in the

College of Graduate Studies

University of Idaho

by

Rachel Peterson

Major Professor: Mark Roll, Ph.D.

Committee Members: Herbert Hess, Ph.D.; Vivek Utgikar, Ph.D.

Department Administrator: D. Eric Aston, Ph.D.

August 2017

Authorization to Submit Thesis

This thesis of Rachel Peterson, Submitted for the degree of Master of Science with a Major in Chemical Engineering and titled "**Thermal Management of a High Efficiency Electrical Energy Conversion Unit**," has been reviewed in final form. Permission, as indicated by the signatures and dates below, is now granted to submit final copies to the College of Graduate Studies for approval.

Major Professor: _____ Date: _____

Mark Roll, Ph.D.

Committee Members: _____ Date: _____

Herbert Hess, Ph.D.

_____ Date: _____

Vivek Utgikar, Ph.D.

Department Administrator: _____ Date: _____

D. Eric Aston, Ph.D.

Abstract

Power conversion units are used any time there is an electrical energy conversion or a nominal voltage change, which makes them a crucial part of everyday modern life. The thermal management of these devices can be difficult with the push toward higher density electronics. In this work, heat sink sizing techniques are used to evaluate the required cooling needs of a multi-stage, multi-phase, high-efficiency power conversion unit. Traditional parallel plate finned heat sinks in both forced and natural convection environments are evaluated using finite element analysis, and analytical correlations, and further compared to experimental results. The feasibility of heat recovery within the realm of power electronic devices, specifically with thermoelectric generation is also presented. With the use of a thermal core heat sink design, a compact thermal solution is developed and modeled using analytical correlations and finite element simulations.

Acknowledgements

I would like to first thank my major professor Dr. Mark Roll for guiding me through this process and making my graduate studies enjoyable. The many hours spent lingering in the graduate student office to discuss research shows how important student progress is to Professor Roll, and I am grateful to have had the opportunity to work in his lab.

I would also like to thank my committee members Dr. Herbert Hess and Dr. Vivek Utgikar for taking the time out of their busy schedules to read, listen and provide feedback on this work. I would additionally like to thank Professor Hess for allowing me to be apart of his project and fostering collaborative research among engineering disciplines.

Further, I would like to thank Amrit Dahal for his work on the electrical side of the project, and whose work made this project possible. Amrit Dahal's guidance from the electrical engineering perspective was very helpful. I would also like to thank Dr. Gabriel Potirniche for his guidance and feedback on simulation and thermoelectric generation.

Additionally, I would like to thank the undergraduate senior design team (James Sutton, Conner Trulock, Caleb Jo) whose manufacturing and testing work enabled multiple functioning heat sink designs.

Dedication

I would like to dedicate this work to my parents, for their unwavering support and encouragement throughout my academic career, and
to Trevor MacLean for his feedback, love and encouragement.

Table of Contents

List of Figures

List of Tables

Chapter 1: Introduction & Background

Power electronics are an essential aspect of our modern world. They are used any time there is a nominal voltage change or a conversion from AC to DC or DC to AC. There have been many advances in power electronic technology as well as significant growth in the global market for power electronics [1]. One challenging aspect of power electronic design is dissipating the high heat loads produced by conduction and switching losses while maintaining high overall efficiency.

When a current passes through an electrical resistance it produces heat. This heat must be removed in order to keep electronics at manageable operating temperatures. As electronic components become more efficient, less power is lost as heat. However, this also means more components can be added to the same substrate, ultimately increasing the power density, but also creating an increase in heat output. Gordon Moore predicted in 1965 that electronic complexity would double every year [2]. He later clarified that in the modern age electronic complexity doubles at a rate of about two years [3]. He also went on to say that Moore's law has become a standard for electronic manufacturing technologies and if it is not being met, there is a sense of falling behind the technology [3]. The switch from small-scale integration (SSI) with less than 100 devices per chip to very-large integration (VLSI), fewer than 10^7 devices per chip, as well as ultra-large scale integration (ULSI), more than 10^7 devices per chip, has created significant challenges in thermal management [4]. Thermal management is a crucial aspect of any electronic components as it can ensure the functionality of the component, reliability of the circuits, and can increase the speed of the device. The leading cause for device failure is high temperature, followed by vibration, humidity and dust [4]. At high temperatures the device performs poorly and can catch on fire. In order to keep up with the rapid progress in electronic complexity, thermal management techniques must also be improving.

The work presented in this thesis is funded through an SBIR grant with the goal of developing a multi-stage, multi-phase, high efficiency electrical energy conversion unit. In the energy conversion unit, the current switching device is of most concern from a thermal management perspective. The thermal management design will be

focused around the switching device location. The purpose of the work to follow is to explore traditional cooling solutions for the power electronics within the energy conversion unit as well as to consider unique thermal management designs, which include waste heat recovery through thermoelectric generation. Consideration of these thermal management techniques will be explored using analytical correlations, and finite element analysis simulations with some experimental validation. This research will help in determining the present limits of convective cooling and potential directions for future electronic thermal management, including heat recovery.

The remainder of Chapter 1 reviews heat dissipation aspects of current power electronic devices, as well as traditional heat sink sizing practices and basic heat transfer physics. Chapter 2 looks specifically at parallel plate heat sink analysis methods. Comparisons between theoretical correlations and finite element simulation are considered for forced and natural convection. Some experimental results are also compared. Chapter 3 addresses heat recovery, specifically the current state of thermoelectric generation as a waste heat management option. The final power converter thermal management design and areas for future progress and improvement of thermal performance are presented in Chapter 4.

1.1 Electronic Packaging and Heat Flow:

The electrical device of most concern in the electrical energy conversion unit is the switching device, as this device will have the highest heat density. The electrical team selected silicon carbide (SiC) MOSFETs as the power-switching devices for the multi-stage, multi-phase, high efficiency electrical energy conversion unit. A MOSFET is a transistor type, whose name is derived from an acronym meaning metal-oxide semiconductor field-effect transistor [5]. SiC MOSFETs have higher voltage, lower on-resistance, and faster switching speeds than the traditional silicon MOSFET [1]. Therefore, the use of SiC can be used to help improve the efficiency of the device over traditional silicon devices. SiC devices can also operate relatively efficiently at higher temperatures due to their wide bandgap [6], which is advantageous in heat recovery applications.

A typical electronic package consists of a processing chip, or multiple chips, set inside a substrate connected to a heat spreader with some type of thermal interface material that is as thermally conductive as possible, while still being electrically insulating. Electronic packaging is a fundamental discipline in the electronic industry and involves many considerations, such as protection, mechanical stress, cooling, and noise emission [7]. While thermal management within the package is recognized as a crucial part of the thermal solution, custom packages were not considered at this phase of the project. The thermal modeling and design process of the project was focused on system level cooling, or cooling outside of the electronic package. In order to determine the necessary system level cooling needs, some information about the package must be understood, specifically the heat dissipation rate and the junction to case thermal resistance.

The heat dissipation rate is directly related to the drain to source on-resistance (or on-resistance for short) of the device. The on-resistance is the sum of the individual resistances between the drain and the source during the ON state [8]. For the case of power MOSFETs, one desires electronic packages that have low drain to source on-resistance and sufficiently high blocking voltages. Wolfspeed operated by CREE introduced the first packaged 1700V, 45mΩ SiC MOSFET in 2016. Other packaged SiC MOSFETs had been developed at this blocking voltage. However, these previously packaged devices were limited by drain to source on-resistances nearly two orders of magnitude higher. The drain to source on-resistance of 45mΩ for a blocking voltage of 1700V is the same as Wolfspeed's advertised bare die. From a thermal management perspective, this packaged device is the best commercially available choice.

Estimation of the heat dissipation, or power loss, of the device is not a trivial task. Poor estimation of power dissipation is often the leading cause of incorrect predicted device temperatures [9]. Understanding the power dissipation starts with understanding the behavior of the electronic device within the package. Integrated electrical and thermal, electro-thermal, simulations are quickly becoming the best practice of predicting heat dissipation at certain operating conditions next to actual experimental testing. These integrated solutions are needed because electrical performance is related to the operating junction temperature, and the heat removal is

related to the electrical performance. The device on-resistance is a function of the junction temperature and gate-source voltage [8]. The drain to source on-resistance dependence on junction temperature is referred to as the temperature coefficient. This coefficient is positive for power MOSFETs [10]. As the temperature of the MOSFET junction increases the drain to source on-resistance also increases. The on-resistance is then used to determine the conduction power losses by [8]:

$$P_{cond} = {I_{out}}^2 R_{rds(on)} \frac{V_{out}}{V_{in}} \tag{1.1}$$

where $\frac{V_{out}}{V_{in}}$ is the duty cycle, $R_{rds(on)}$ is the drain to source on-resistance, and I_{out} is the operating current. For power MOSFETs, there are additional losses due to switching. However, because switching losses are often small in SiC MOSFET devices [6], these additional losses are not included in the analysis.

Electro-thermal simulations are beyond the scope of the current research and require a greater understanding of the physics within the electronic devices. However, based on datasheet values, the heat dissipation as a function of junction temperature at specified operating conditions can be estimated. The datasheet provided by Wolfspeed under CREE for the 1700V SiC MOSFET (part number: C2M0045170D) [11], gives a drain to source on-resistance versus junction temperature for various gate voltages at a drain source current of 50A. It also provides on-resistance versus drain source current plots at various junction temperatures for a gate voltage of 20V. These figures are used to estimate the on-resistance and ultimately the power loss as a function of the junction temperature for specific operating conditions.

The predicted operating conditions for the device is a gate voltage of 20V and a drain current of 20A. In order to reproduce the plot of on-resistance versus junction temperature at a drain current of 20A as opposed to 50A, data points from the on-resistance versus drain source current plot were taken at 20A at each junction temperature plotted. The on-resistances from these data points were then compared at the corresponding junction temperatures of the on-resistance versus junction temperature plot. The difference in the on-resistance at each temperature plotted is

used to scale the on-resistance from a drain current of 50A to 20A at a gate voltage of 20V. The corresponding plot of on-resistance as a function of junction temperature for a drain current of 20A and gate voltage of 20V is given in Figure 1.1. Using Equation 1.1, the heat output, based on conduction power loss, is plotted as a function of the junction temperature in Figure 1.2. The duty cycle was taken to be 50% as advised by the electrical engineering team. A duty cycle of 50% is considered a maximum, or worst-case scenario.

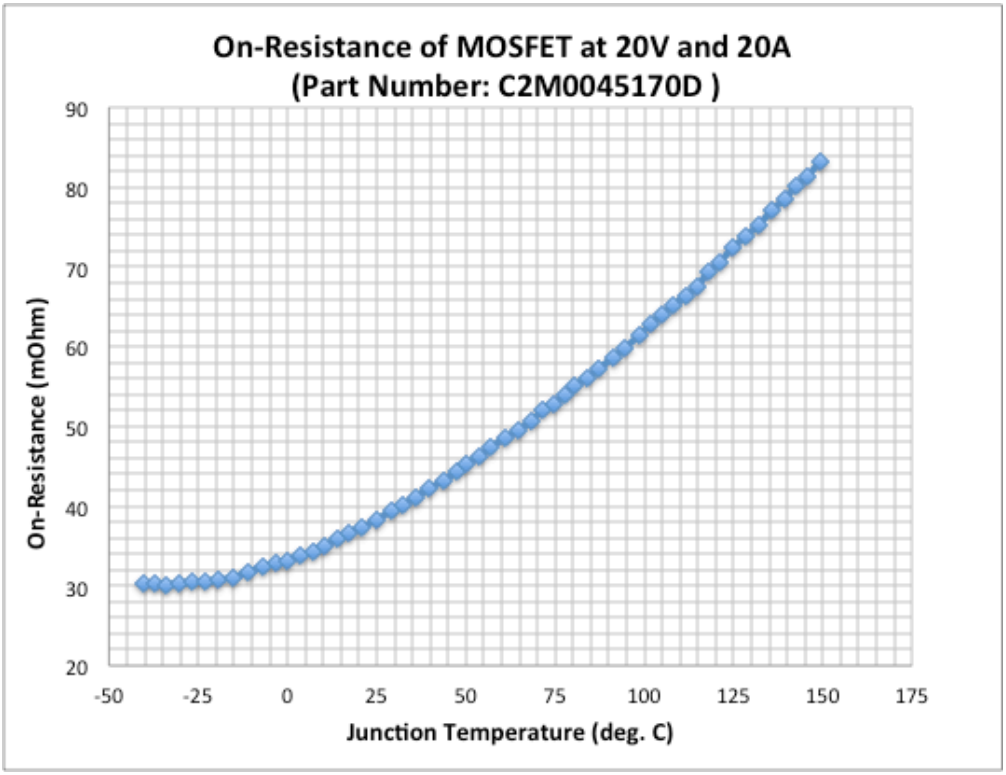

Figure 1.1 – Estimated on-resistance versus junction temperature for the chosen packaged MOSFET at a drain source current of 20A and a gate voltage of 20V. Established from the 1700V SiC MOSFET [11].

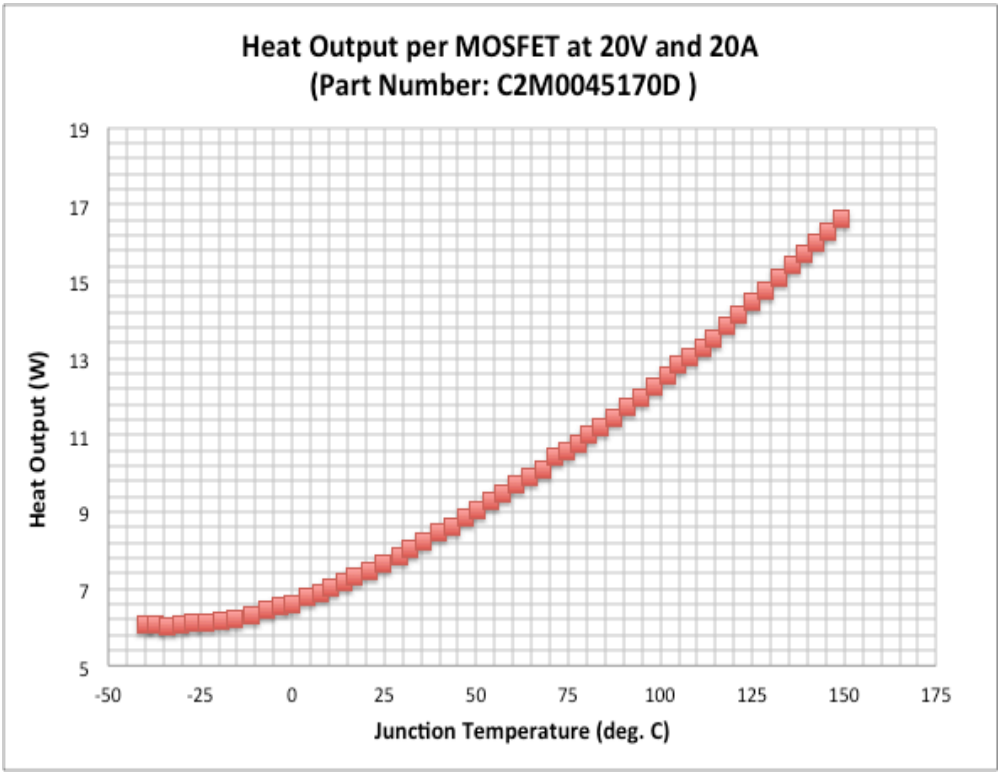

Figure 1.2 - Heat dissipation (power loss) based on Equation 1.1 with on-resistance values from Figure 1.1. The duty cycle is a worst-case scenario of 50%.

The thermal resistance is a quantitative measurement of the heat transfer efficiency across a boundary in a thermal matrix. It is analogous to electrical resistance and defined mathematically as [12]:

$$R = \frac{\Delta T}{Q} \tag{1.2}$$

where Q is the rate of heat flow and ΔT represents the temperature difference across the considered region. In a cooling system, there is a thermal resistance associated with each layer or component. A typical thermal matrix has a thermal resistance associated with the electronic package, the interface between the package and the heat sink, and the heat sink itself. A simple cooling matrix is shown in Figure 1.3. Where R(HS) refers to the heat sink thermal resistance, R(TIM) refers to the interface thermal resistance, and R(jc) refers to the package thermal resistance, or the resistance from the device junction to the case. The device junction temperature is taken as the temperature of the component die. The die is the heat-dissipating portion of the electronic device.

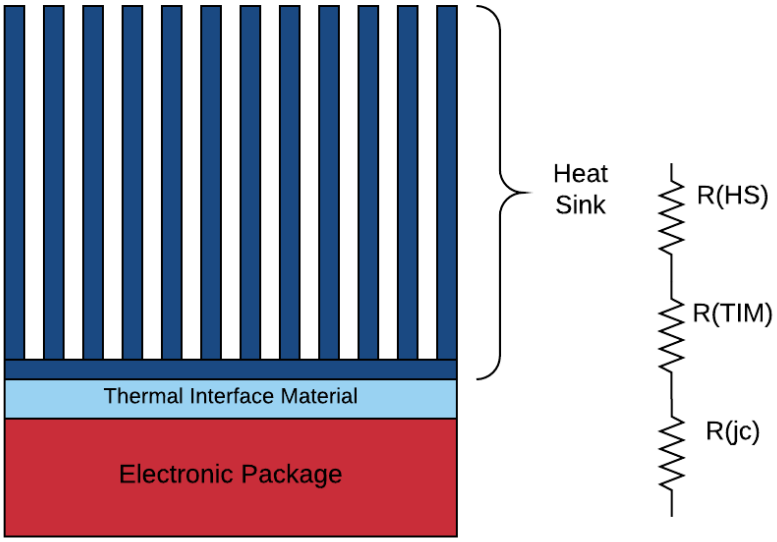

Figure 1.3 - Traditional system level cooling with analogous electrical circuit depiction.

For commercially packaged devices, junction to case thermal resistance is usually given as a single value in the datasheet. However, this value is often difficult to determine, and more complex than a single value. Often times there are multiple paths within a package, which affect the local resistances from the chip junction to the external case [13]. Nordstog et al. [14] show that the junction to case thermal resistance can vary by the location on the die. The variation is attributed to the difference in thermal resistance from the changes in bond line thickness of the thermal interface material due to package warping in temperature cycling situations.

As stated before, R(TIM) is the thermal resistance of the interface between the package and the heat sink. This resistance arises, because no two surfaces can be in perfect thermal contact, due to irregularities and surface roughness of materials. An exaggerated depiction of surface roughness and irregularities is shown in Figure 1.4. In order to reduce the interface resistance, a thermal interface material is placed between the two contacting surfaces to fill the gaps that otherwise would be filled with air, a poor thermal conductor.

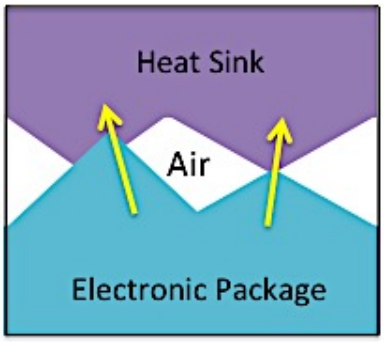

Figure 1.4 - Depiction of contact between electronic package and heat sink without interface material.

There are many types of thermal interface materials ranging from thermal grease to phase change materials. Thermal greases are generally made of silicone with thermally conductive metals or metal oxides. The grease fills voids created at the interface of the two solids to decrease the contact resistance [15]. Phase change interface materials contain a low-melting temperature metallic alloy. Ideally, the melting temperature is just below the operating temperature of the joint and when the joint becomes heated, the liquid metal flows to fill the voids at the interface. Once cooled, the metal hardens and the two components become essentially welded together [15]. In addition to thermal grease and phase change materials, there are thermoplastic as well as carbon nanotube based interface materials [16]. While the thermal interface material reduces the thermal resistance across the interface, it is still often one of the highest thermal resistance layers [16]. The thermal interface material typically must be thermally conductive, and electrically insulated. Unfortunately, electrical conductivity and thermal conductivity are intimately related material properties.

The improvement in thermal resistance with the addition of a phase change thermal interface material is observed experimentally. Heat sink testing was conducted with and without the Laird Technologies Tpcm™ 580. Experimental conditions, test set up, and data will be presented further in Chapter 2. The phase change material was found to improve the thermal resistance from the case to ambient by an average of 1.90°C/W over the course of all tests. Based on the thermal conductivity of air at the operating temperature and a first approximation of the phase change material thermal resistance, the average thickness of air between the heat sink and package is approximately 19.2μm. Surface irregularities can have waves ranging from 20 to 40μm

and surface roughness can range from 0.05 to 25μm [15]. The approximated average air gap predicted from experimental values is within the observed range of surface irregularities and roughness. Therefore, it can be concluded that the predicted thermal resistance improvement of 1.90°C/W is within the expect range. Thermal interface material was not a large focus of the project, however, its importance in the thermal matrix is understood.

In Figure 1.3, thermal resistances are shown in series, much like electrical resistances may be in series in an electrical circuit. When thermal resistances are placed in series, as shown in Figure 1.3, the total thermal resistance is defined as the sum of the individual thermal resistances. As given by:

$$R_{tot} = \sum R_i \tag{1.3}$$

For the typical system shown in Figure 1.3, the thermal resistance can be expressed as [12]:

$$R_{ja} = R_{jc} + R_{TIM} + R_{HS} = \frac{T_j - T_a}{Q} \tag{1.4}$$

Where R_{ja} refers to the total thermal resistance from the junction to the ambient condition and T_j and T_a refer to the junction and ambient temperature respectively. Using the definition of thermal resistance given in Equation 2, one obtains the right most side of Equation 1.4. This is the fundamental simplification in heat sink sizing analysis.

1.2 Heat Sink Sizing:

The required heat sink thermal resistance can be determined with the knowledge of the interface and package thermal resistances, the operating temperatures and the device heat dissipation. Rearranging Equation 1.4 to solve for the required thermal resistance of the heat sink gives the required heat sink thermal resistance as [12]:

$$R_{HS} = \frac{T_j - T_a}{Q} - R_{jc} - R_{TIM} \tag{1.5}$$

For the case of the TO-247 packaged SiC MOSFETs, the junction to case thermal resistance given in the datasheet is 0.22°C/W, with a maximum junction to case thermal resistance value of 0.24°C/W [11]. As a worst-case scenario, the maximum junction to case thermal resistance given in the datasheet will be used to evaluate the heat sink required thermal resistance.

The thermal interface material that was purchased for the power converter prototype is Tpcm™ 580 Series Phase Change Material produced by Laird Technologies®. Based on the thickness and thermal conductivity of the phase change material and the face area of the power MOSFET in the TO-247 package (21.10 mm by 16.13 mm), the thermal resistance of the interface material is estimated to be 0.06°C/W. This provides a first approximation estimate of the thermal resistance of the interface with the phase change thermal interface material. The solid-to-solid contact points as well as bond line thickness and gaps between thermal interface material and contacting solids are not taken into account. To account for these aspects further knowledge of the contacting surfaces as well as the thermal interface material is required and is not within the scope of the current project. It is likely that the interface resistance with the thermal interface material is slightly higher than the first approximation of 0.06°C/W.

Taking the worst-case scenario junction to case thermal resistance (0.24°C/W), and the first approximation of the thermal interface using Tpcm™ 580 Series Phase Change Material (0.06°C/W), the required thermal resistance at desired junction temperatures can be determined using Equation 1.5 for a given ambient temperature. Table 1.1 shows the required heat sink thermal resistance at three different junction temperatures for an ambient temperature of 20°C. The heat dissipation for the evaluation is obtained from Figure 1.2. The required heat sink thermal resistance is evaluated for one MOSFET as well as for sixteen MOSFETs. The power converter prototype will have a total of sixteen MOSFET devices. The thermal resistance for one MOSFET is the maximum required thermal resistance for individual heat sinks on each

MOSFET. The thermal resistance for sixteen MOSFETs is the thermal resistance for a unified heat sink that could cool all sixteen MOSFET devices thermally in parallel with each other. The actual thermal resistance of the chosen heat sink will need to be equal to or less than the value calculated in Table 1.1 to operate below the corresponding junction temperature. Because the heat output is a function of the component junction temperature, for a known heat sink thermal resistance, predicting the actual junction temperature becomes and iterative problem.

Table 1.1 Required Heat Sink Thermal Resistances

Junction Temperature of Each MOSFET	Heat Output per MOSFET obtained from Figure 1.2 with duty cycle	Required Heat Sink Thermal Resistance for one MOSFET at ambient temperature of 20°C	Required Heat Sink Thermal Resistance for sixteen MOSFETs at ambient Temperature of 20°C
150°C	16.6W	7.53°C/W	0.47°C/W
125°C	14.5W	6.94°C/W	0.43°C/W
100°C	12.3W	6.21°C/W	0.39°C/W

Once the necessary heat sink resistance is calculated, the next step is determining a heat transfer method that achieves the necessary thermal resistance. The next section will focus on the fundamental ideas of determining or predicting thermal performance, and specifically determining the thermal resistance.

1.3 Heat Transfer Physics:

Heat can be dissipated by conduction, convection or radiation. In an electronic cooling system, often all three forms of heat transfer are at work. The following section will consider the fundamentals of the three forms of heat transfer and their relation to thermal resistance and thermal performance.

Conduction is the transfer of internal energy, or heat, by means of contact between two bodies. Heat transfer occurs from higher energy molecules to lower energy molecules, or from hot to cold. Fourier's law gives the governing equation for the rate of heat transfer by conduction. For the one-dimensional case, where thermal conductivity is assumed to be constant through the direction of heat flow, Fourier's law becomes [17]:

$$q = -kA\frac{dT}{dx} \tag{1.6}$$

where k is the thermal conductivity of the medium, A is the area normal to the direction of heat flow, and q is the heat transfer rate. For a system with conduction length, L, separated by temperatures T_1 and T_2, separation and integration of Equation 1.6 gives:

$$q = -kA\frac{T_2 - T_1}{L} \tag{1.7}$$

Rearranging Equation 1.7 in terms of the thermal resistance as defined in Equation 1.1 gives:

$$R_{cond} = \frac{T_1 - T_2}{q} = \frac{L}{kA} \tag{1.8}$$

where R_{cond} is the thermal resistance due to conduction. Equation 1.8 is used to determine the thermal resistance across materials in thermal contact.

Convection is essentially conduction through fluids with flow. At the solid-fluid interface, heat is conducted to a certain boundary layer and then is swept away by the flow of fluid. The general equation describing convective heat transfer, which is often referred to as Newton's law of cooling, is [17]:

$$q = hA(T_w - T_{ref}) \tag{1.9}$$

where T_w is the wall temperature, T_{ref} is a reference temperature of the fluid, often the ambient fluid temperature, A is the surface area available for convective heat transfer and h is the convective heat transfer coefficient. Rearranging Equation 1.9 in terms of the thermal resistance defined in Equation 1.1 gives what is known as the film thermal resistance:

$$R_{film} = \frac{T_w - T_{ref}}{q} = \frac{1}{hA} \tag{1.10}$$

In convective heat transfer, the film resistance can be thought of as the thermal resistance between the fluid and solid interface. The convective heat transfer coefficient

is a function of the fluid properties, geometry and fluid flow. It is often expressed in dimensionless form in terms of the Nusselt number $\left(Nu = {hL_c}/{k}\right)$, where L_c is the characteristic length and k is the thermal conductivity of the fluid. The Nusselt number can then be written as a function of Reynolds and Prandlt number for forced convection or Grashof and Prandtl number for natural convection. The functions of these correlations between dimensionless parameters depend on fluid flow type and channel geometry [17]. The dilemma in predicting convective heat transfer lies in the accuracy of determining the convective heat transfer coefficient. Correlations for laminar flow through simple geometries have been developed and will be discussed further in Chapter 2, however, for more complex systems, numerical analysis, computational fluid dynamics or finite element analysis is needed to estimate the convective heat transfer coefficient. Convective heat transfer will be covered in greater detail in Chapter 2.

Pressure drop is an important aspect of convective heat transfer. Whenever there is fluid flow there is an accompanying fluid restriction or drag that must be overcome for the fluid to move. While pressure drop is not a concern in natural convection, the ability for fluid to move freely through extended surfaces, such as heat sink fins, is still of great importance. Correlations that relate natural convection take this into account and will be further discussed in Chapter 2.

In forced convection, the pressure drop is used in conjunction with a fan curve to predict the fluid flow rate, and once predicted, the convective heat transfer coefficient is estimated using correlations. Pressure drop is calculated first by determining the system head loss. The pressure difference is calculated by multiplying the estimated head loss by the density of the fluid and acceleration due to gravity. For steady flow through a pipe or a duct, a simple force balance gives pipe head loss, h_f, as [18]:

$$h_f = 4f_f \frac{L}{D}\frac{V^2}{2g} \tag{1.11}$$

where V is the velocity of the fluid, g is the acceleration due to gravity, L is the length of the pipe, D is the diameter of the pipe, and f_f is the Fanning friction factor. Equation 1.11 can also be used for noncircular ducts [19], such as parallel plates often

encountered in traditional finned heat sinks. For parallel plates, L is the length of the plate, and D is the hydraulic diameter, defined as $D = \frac{4A}{P}$ where A is the cross-sectional area and P is the wetted perimeter.

The Fanning friction factor is a dimensionless ratio of shear stress acting at the wall divided by the kinetic energy flow per unit volume [18]. The Fanning friction factor is often determined by correlations in terms of the Reynolds number. For hydrodynamically developing flow, an apparent Fanning friction factor can be used. The apparent friction factor takes into account skin friction and change in momentum rate due to change in the shape of the velocity profile in the entrance region [20]. For the case of parallel plates, there are additional component head losses due to contraction and expansion of the flow as it enters and exits the channels. Correlations for the Fanning friction factor and the apparent Fanning friction factor as well as how to account for expansion and contraction of fluid flow will be further discussed for parallel plate geometry in Chapter 2.

Radiation heat transfer is often neglected in the heat transfer analysis of electronics cooling. However, radiation heat transfer can be a significant component in some natural convection systems. Thermal radiation for an ideal blackbody, or perfectly emitting body, is given by the Stefan-Boltzmann equation [17]:

$$q_r = A\sigma T^4 \tag{1.12}$$

where q_r is the rate of radiant emission, A is the body surface area, T is the absolute temperature of the body's surface, and σ is the Stefan-Boltzmann constant with a value of 5.67E-8 W/m^2K^4. However, for the case of a heat sink in the atmosphere, there will be radiation from the surroundings as well. Radiation between two gray bodies can be described as [21]:

$$q_{1-2} = A_1 \Im_{1-2} \sigma \left({T_1}^4 - {T_2}^4 \right) \tag{1.13}$$

where q_{1-2} is the net radiative heat exchange between the two bodies, and $\Im_{1-2}$ is the gray body view factor, which is a function of the emissivity of the two surfaces and the view factor of the radiating bodies. Assuming that there is no radiation from the

surroundings, and that the heat sink is at the maximum temperature of the MOSFET, 150°C, or 423.15K, the maximum rate of radiant heat transfer given by a perfect emitting body would be:

$$\frac{q_r}{A} \leq \left(5.67E-8\frac{W}{m^2K^4}\right)(423.15K)^4 = 0.18\frac{W}{cm^2}$$

The actual heat flux dissipation by thermal radiation will be less than the value stated above, as the dissipating body is not a perfectly emitting black body, and would receive radiation from the surrounds. The black body thermal radiation rate without taking into account background radiation is quite small when compared to typical heat flux dissipation rates by conduction and convection. Based on typical values of convective heat transfer coefficients, an ambient temperature of 30°C and a wall temperature of 150°C, heat transfer by even free convection is about two orders of magnitude greater than heat transfer by radiation [22]. If the temperature is high enough, with little convection, radiation heat transfer may play a key role in thermal management. However, for the application of power MOSFETs with a maximum temperature of 150°C, radiation will not be significant. Therefore, radiation is not further considered.

1.4 Current Trends in System Level Cooling:

System level cooling of electronics has not changed significantly since the introduction of computers [23]. Air-cooled heat sinks still dominate the industry, as other exotic cooling methods such as liquid cooled manifolds, spray-cooled enclosures, and vapor-compression refrigeration have proven to be complex, power exhausting and costly for practical commercial applications [23].

Typical heat sink designs focus on two strategies. The first is increasing surface area available for convective heat transfer, typically accomplished by extended objects, while the second is to decrease the fluid flow resistance. Both concepts involve reducing the film thermal resistance, or increasing heat dissipation by convective heat transfer. Air-cooled forced convection is one of the most common heat sink types. Although air has a relatively low thermal conductivity, its low viscosity and availability make it a desirable working fluid in electronic heat transfer design.

Increasing the power density of power converting devices is a large topic that comes with large thermal problems. Recently, Google and IEEE launched an open challenge called the “little box challenge” [24]. The goal of the competition was to design and build a kilowatt scale power inverter with the highest power density possible. The top team had an impressive power density of 143W/in^3. The technical approach documents of the top three finalist on the “little box challenge” website, show traditional heat sinking designs. The winners used a forced air-cooling approach with a honeycomb shaped copper heat sink [25]. The remaining two finalists also use forced air-cooling. One of the two remaining finalists made the casing out of copper to double as additional heat sink area assisting the internal heat sinks [26].

Liquid cooling as well as two phase cooling is gaining popularity in electronic heat transfer applications. Liquid cooled cold plate often involve similar finned or pin heat sink designs, but use a liquid as a cooling fluid, often water, as opposed to air [27]. Water-cooled cold plates can have thermal resistances that are much lower than a typical air-cooled heat sink. However, the liquid in a cold plate system needs additional cooling outside of the system; typically this is often left to an air-cooled radiator. Another drawback of liquid cooling is that higher pumping costs are needed to overcome the high pressure drop of liquids [27]. Before using a cold plate system it is necessary to evaluate if the required thermal resistance cannot be accomplished through traditional air-cooled systems, which have lower energy consumption. This is especially important when minimizing the overall efficiency of the device.

Heat pipes and vapor chambers are the most widely used two-phase heat transfer devices. Heat pipes are vacuumed sealed hollow tubes that may be flattened or bent. They contain a wicking structure on the inner diameter. In a heat pipe, the working fluid is evaporated at the heat source and then condensed in a colder region of the heat pipe. The wicking structure moves the condensed liquid back to the heat source to be vaporized [28]. Heat pipes should be used to move heat to a location where it can be more easily dissipated.

Vapor chambers are vacuumed sealed flat metal structures that contain a working fluid. Much like heat pipes they use a wicking structure to bring the liquid to the heat source where it is then vaporized. Vapor chambers, unlike heat pipes can

transfer heat in any direction along the chamber. Vapor chambers are typically used for effective heat spreading. They are advantageous in height limited, low airflow or high ambient situations. They are typically used in conjunction with air-cooled heat sinks.

A common trend in board configuration is to place the highest heat dissipating components as far apart as possible. However, the idea of having a unified thermal core, with one heat sink connected to the highest heat dissipating devices at a central location is gaining interest. Having one heat sink for the highest heat dissipating devices does increase the heat load that must be dissipated by the heat sink. However, it often provides more available space to dissipate heat and can create a more compact thermal solution. Central core heat dissipation will be discussed further in Chapter 4, as this is the approach taken for the final converter heat sink design.

While new technologies are rising, the importance of air-cooling, especially forced air-cooling, is significant. Even with the use of heat pipes, vapor chamber, or cold plates, there is still a need for further cooling that often involves forced convection of air. Chapter 2 will focus on convective heat transfer with special focus on parallel plates, which are often encountered in heat sink geometries. The final converter design has both a liquid and air cooled solution, which will be further discussed in Chapter 4.

References:

[1] J. Parry, "Power Electronics: The Hidden Revolution," *Engineering Edge*, vol. 2, pp. 16-17, 2013.

[2] G. E. Moore, "Cramming more components onto integrated circuits," *Electronics*, vol. 38, no. 8, Apr. 1965.

[3] "Excerpts from a conversation with Gordon Moore: Moore's Law," *Intel: Video Transcript*, 2005.

[4] L.T. Yeh and R. C. Chu, "Introduction," in *Thermal Management of Microelectronic Equipment: Heat Transfer Theory, Analysis Methods, and Design Practices*, New York: ASME Press, 2002, ch. 1, pp. 1-8.

[5] (2003). *The Free Dictionary* [Online]. Available: http://acronyms.thefreedictionary.com/MOSFET

[6] ROHM Semiconductor, Appl. Note 14103EBY01, pp. 8-17.

[7] X. C. Tong, "Thermal management fundamentals and design guides in electronic packaging," in *Advanced Materials for Thermal Management of Electronic Packaging*. New York: Springer, 2011, ch. 1, pp. 1-58.

[8] R. Murugan et al., "System-Level Electro-Thermal Analysis of $R_{DS(on)}$ for Power MOSFET," in *33rd SEMI-THERM Symposium*, 2017, San Jose, CA., pp. 52-56.

[9] R. Bornoff, J. Parry, 33rd SEMI-THERM Symp. Short Corse, Topic: "A History of Commercial CFD from Bernoulli to Spalding and Beyond, with a Focus on Electronics Cooling." Mar. 13, 2017.

[10] A. Satter. *Power MOSFET Basics* [Online]. Available: http://www.ixys.com/Documents/AppNotes/IXAN0061.pdf

[11] CREE, "Silicon Carbide Power MOSFET C2M™ MOSFET Technology," C2M0045170D datasheet, Jun. 2016.

[12] S. Lee. (1995, June). *How to Select a Heat Sink* [Online]. Available: http://www.electronics-cooling.com/1995/06/how-to-select-a-heat-sink/

[13] B. Guenin. (2005, Aug.). *A Funny Think Happened on the Way to the Heatsink* [Online]. Available: https://www.electronics-cooling.com/2005/08/a-funny-thing-happened-on-the-way-to-the-heatsink/

[14] T. Nordstog et al., "Junction to Case Thermal Resistance Variability Due to Temperature Induced Package Warpage," in *33rd SEMI-THERM Symposium*, 2017, San Jose, CA., pp. 235-245.

[15] L.T. Yeh and R. C. Chu, "Thermal Interface Resistance," in *Thermal Management of Microelectronic Equipment: Heat Transfer Theory, Analysis Methods, and Design Practices*, New York: ASME Press, 2002, ch. 9, pp. 141-167.

[16] S. Narumanchi et al., "Thermal Interface Materials for Power Electronics Applications," in *Itherm*, 2008, Orlando, Fl.

[17] J. R. Welty, C. E. Wicks, R. E. Wilson, G. L. Rorrer, "Fundamentals of Heat Transfer" in *Fundamentals of Momentum, Heat, and Mass Transfer, 5th ed.,* Jefferson City, MO: John Wiley & Sons, Inc., 2008, ch. 15, pp. 201-213.

[18] C.T. Crow, D.F. Elger, B.C. Williams, J.A. Roberson, "Flow in Conduits," in *Engineering Fluid Mechanics,* Jefferson City, MO: John Wiley & Sons, Inc., 2009, ch. 10, pp. 315-351.

[19] F.M. White, "Viscous Flow in Ducts," in *Fluid Mechanics, 7th ed.*, New York, NY: McGraw-Hill, 2011, ch. 6, sec. 6.8, pp. 379-388.

[20] R.K. Shah and A. L. London, "Parallel Plates," in *Laminar Flow Forced Convection in Ducts*, United Kingdom: Academic Press, 1978, ch. 6, pp. 153-195.

[21] L.T. Yeh and R. C. Chu, "Radiation Between Gray Isothermal Surfaces," in *Thermal Management of Microelectronic Equipment: Heat Transfer Theory, Analysis Methods, and Design Practices*, New York: ASME Press, 2002, ch. 4, sec. 4.4, pp. 58-61.

[22] *Convective Heat Transfer* [Online]. Available: http://www.engineeringtoolbox.com/convective-heat-transfer-d_430.html

[23] T. A. Johnson, J. P. Koplow, W. L. Staats, D. B. Curgus, M.T. Leick, D. Matthew, M. D. zinnerman, M. Arienti, P.E. Gharagozloo, E. Hecht, N. Spencer, J.W. Vanness, R. Gorman, "Development of the Sandia Cooler," SNL> Albuquerque, NM. Rep. SAND2013-10712, 2013.

[24] R. Koningstein. (2016). *And the winner of the $1 Million Little Box Challenge is… CE+T Power's Red Electric Devils* [Online]. Available: https://research.googleblog.com/2016/02/and-winner-of-1-million-little-box.html

[25] O. Bomboir et al. "Technical Approach Document: CE+T Power," in *The Little Box Challenge*, 2014.

[26] J.S. Lai et al., "Technical Approach Document: Virginia Tech.," in *The Little Box Challenge*, 2014.

[27] L.T. Yeh and R. C. Chu, "Advanced Cooling Technologies I; Single-Phase Liquid Cooling," in *Thermal Management of Microelectronic Equipment: Heat Transfer Theory, Analysis Methods, and Design Practices*, New York: ASME Press, 2002, ch. 14, pp. 261-279.

[28] G. Meyer, 33rd SEMI-THERM Symp. How-To Course, Topic: "Practical Guidelines for Using Heat Pipes and Vapor Chambers in Heat Sinks." Mar. 15, 2017.

Chapter 2: Parallel Plate Finned Heat Sinks

Convective heat transfer is a fundamental topic in thermal engineering and design. It incorporates heat transfer and fluid flow, which makes it a challenging phenomenon to describe analytically. The primary focus here is to understand the thermal resistance of the heat sink. The thermal resistance from the heat sink to the ambient environment is governed by both conduction and convection. Conductive heat transfer occurs from the base of the heat sink and through the fins. Choosing a heat sink made of a highly conductive material is beneficial in minimizing the thermal resistance due to conduction. With a high thermal conductivity material, the greatest thermal resistance between the heat sink and the ambient environment becomes the film resistance, or the resistance from the heat sink solid to the cooling fluid. From Equation 1.9, it can be seen that both increasing the convective heat transfer coefficient as well as increasing the area available for convective heat transfer can reduce the film thermal resistance. Increasing the surface area available for heat transfer often involves increasing the heat sink volume. However, with the push for higher power densities, the heat sink volume is often strictly limited.

One of the most common methods used to increase the surface area, without significantly increasing the heat sink volume footprint is to use extended objects. Parallel plates are described as the thermal "building block" of extended objects, and are the most common among in heat sink design [1]. Parallel plates increase the surface area available for convective heat transfer, which in turn reduces the thermal resistance across the heat sink by reducing the thermal barrier between the heat sink, air interface. Parallel plate heat exchangers are used in both forced and natural convection applications. With the use of concepts in fluid mechanics coupled with heat transfer, parallel plate heat exchangers can be effectively described by theory. The following chapter will focus on parallel plate heat exchanger correlations in gasses and liquids, primarily air and water, and for both forced and natural convection. Analytical results as well as finite element analysis (FEA) simulations will be compared to each other and to experimental data.

2.1 Forced Convection:

Forced convection can first be broken into two distinct flow types, internal and external. Internal convective heat transfer involves the flow of a viscous fluid through a closed conduit, such as a rectangular duct. External convective heat transfer refers to fluid flow over a surface, or a flow that is not confined to a finite sized passage. The passage walls define the boundary conditions of internal heat transfer problems, whereas external boundary conditions are related to free-stream values at a certain distance from the solid wall [2]. However, typical parallel plate heat sinks have fins that are spaced close together in attempt to maximize the surface area over a given area footprint. Therefore, most correlations established for parallel plate heat sinks use an internal flow type analysis.

As a viscous fluid flows through a duct, a velocity boundary layer develops along the internal surfaces of the duct. When the velocity boundary layers fill the entire duct, the flow is considered hydrodynamically fully developed. When the flow is fully developed the boundary layer thickness is described as half the diameter of the pipe, or half the width of the channel. The hydrodynamic entrance region is the region in which the flow is still developing and the boundary layers have not encompassed the entire duct. The length of this region is referred to as the hydrodynamic entrance length, L_h, and is often difficult to predict. If the flow transitions to turbulent before the boundary layers fill the entire duct, then the flow remains turbulent throughout the full-developed region. If it does not transition to turbulent, the then flow is laminar throughout the duct [2]. Transition from turbulent to laminar flow occurs at a critical Reynolds number. For closed conduits, the critical Reynolds number is approximately 2300 $\left(Re = \frac{\rho V d}{\mu} \cong 2300\right)$. For non-circular ducts, the critical Reynolds number depends on the cross-sectional geometry of the duct. However, for most applications, the use of circular duct critical Reynolds number can be used to indicate transition from laminar to turbulent flow, when the diameter is replaced by the hydraulic diameter [2]. The hydraulic diameter is defined as $d_h = 4\frac{A}{P}$ where A is the cross-sectional area, and P is the wetted perimeter. For the case of a fully wetted rectangular channel, the hydraulic diameter

becomes $d_h = \frac{2ab}{a+b}$ where a is the longer edge and b is the shorter edge of the rectangular cross-section [2].

For flow that is being heated, such as the case for flow through a heat sink, there also exists a thermal boundary layer. The thermal boundary layer, like the velocity boundary layer, develops along the inside of the duct. Assuming uniform temperature of inlet fluid, the thermal entrance length, L_t, is defined as the duct length required to have a local Nusselt number equal to 1.05 times the Nusselt number for fully developed flow [2]. The Nusselt number is a dimensionless parameter relating the convective heat transfer to the conductive heat transfer and is described by $Nu = {}^{hL_c}/_{k}$, where h is the convective heat transfer coefficient, L_c is the characteristic length and k is the thermal conductivity of the fluid.

Fully developed flow is flow that is both hydrodynamically and thermally developed. When heating or cooling starts from the inlet of the duct, as would be the case for most parallel plate heat sink configurations, the velocity and temperature profile develop simultaneously. The rate at which the heat and momentum diffuse from the wall is defined by the Prandtl number, $Pr = \frac{C_p \mu}{k} = \frac{\alpha}{\nu}$ where $\left(\alpha = \frac{k}{\rho C_p}\right)$ is the thermal diffusivity and $\left(\nu = \frac{\mu}{\rho}\right)$ is the kinematic viscosity. The special case of $Pr = 1$ or $\alpha = \upsilon$, describes the condition when the viscous and thermal effects diffuse through the fluid at the same rate. For external flows this condition produces thermal and velocity boundary layers of the same thickness. However, for internal flows, when $Pr = 1$, the thermal and velocity boundary layers are not the same thickness, since the governing momentum and energy equations do not converge [2].

There are two main boundary conditions to consider when analyzing convective heat transfer through ducts, which lead to different solutions of the Nusselt number. These two boundary conditions are constant wall temperature (isothermal wall), denoted by subscript T, or constant heat flux. Constant heat flux boundary condition can be further broken into two conditions. One condition is having constant wall heat transfer rate in the axial direction, and constant wall temperature in the peripheral direction at any cross-section. This condition is denoted by subscript H_1. The other heat

flux boundary condition is denoted by H_2 and has constant wall heat transfer in both axial and peripheral directions [2]. Figure 2.1, reproduced from [2], shows the three different boundary conditions graphically. Energy balance solutions for the Nusselt number for different rectangular aspect ratio ducts for each of the three boundary conditions in fully developed, laminar flow conditions are given in [2].

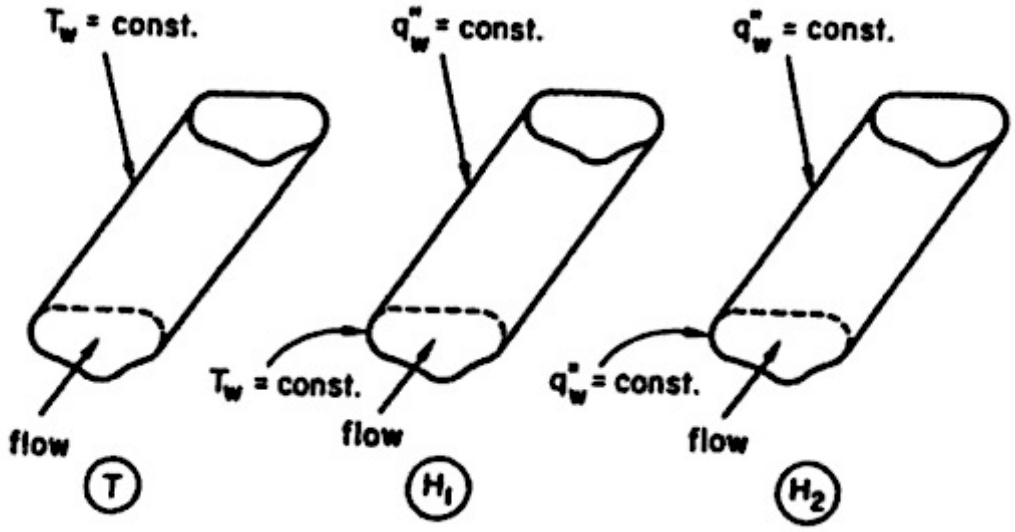

Figure 2.1 - Important boundary conditions in duct flows. Image is reproduced from [2].

There are many types of correlations that can be used to describe parallel plate heat sinks. Reference 3 provides a comprehensive table of Nusselt number correlations for various flow types, boundary conditions, fully developed and developing flows for a wide variety of geometries. The type of system and boundary conditions of the heat sink will determine the most appropriate correlation to use.

Commercially available, parallel plate heat sinks that match the specifications of the power MOSFET to be used in the prototype were analyzed by:

- Experimental tests in air
- FEA simulations with air, helium and water
- Analytical correlations with air, helium and water

The thermal resistance and pressure drop through the heat sink are compared for the three different studies.

2.1.1 Experimental Testing:

The commercially available heat sinks used for testing are black anodized W series Ohmite heat sink (part number: WA-T247-101E). The power MOSFETs used in the power converter prototype are available in TO-247 packages. Therefore, resistors in a TO-247 package were used as the heat source during testing.

Three different operating orientations with and without phase change thermal interface material were tested. The first two orientations were to test natural convection of the heat sink. The results from these tests will be discussed further in the next section. The third orientation has heat sink fins perpendicular to the table surface, or vertically oriented fins. A fan was placed under the board to blow air up through the fins. The testing apparatus for the forced air experiment can be seen in Figure 2.2.

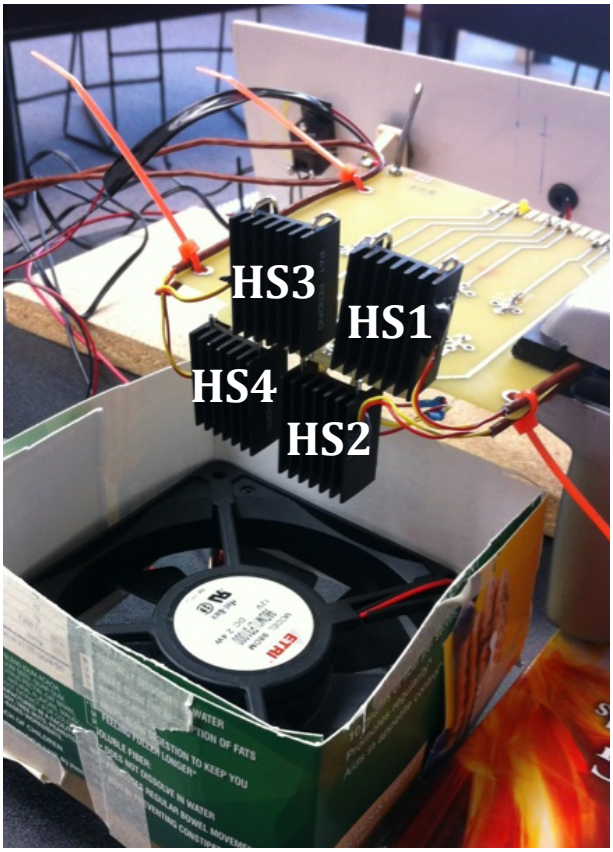

Figure 2.2 - Testing configuration for forced convection experiment with vertically oriented fins.

The heat sinks are labeled as HS1, HS2, HS3, and HS4. This is to denote which temperature corresponds to which heat sink. The temperatures of HS1 and HS3 will be

higher than the temperature of HS2 and HS4 as the air passing through the top heat sinks, HS1 and HS3, has already been heated by the bottom heat sinks, HS2 and HS4. Each test was conducted three times and the measured temperature for each test was averaged.

Thermocouples were mounted on the outer sides of the heat sink with the assumption that the entire heat sink will be about the same temperature as the resistor. Because the heat sink is made of aluminum, which is a conductive metal, the assumption that the entire heat sink is the same temperature as the resistor is a reasonable assumption. The ambient temperature was recorded before and after each test. The temperature on each heat sink was recorded over period of time until the temperature no longer rose and the system was assumed to be at steady state (approximately 30 minutes). To normalize the temperature data, the rise in temperature above the average ambient temperature was calculated and used for further analysis. Experimental tests with and without thermal interface material were performed.

With no phase change thermal interface material, a target temperature no greater than 100°C steady state for each orientation was attempted. The power input that was required to achieve a maximum temperature of 100°C was recorded and used for the following test. The power input that was used for the forced convection orientation was 8.32W. It was assumed that all input power to the resistor is converted to heat dissipation. Three trials with and without thermal interface material were run and the average temperature for each test was determined. Averaged thermal resistance results are shown in Table 2.1 for tests with and without thermal interface material.

It was observed that the thermal resistance of HS 1 and HS 3 are higher than HS 2 and HS 4. This is because the thermal resistance is calculated based on a temperature difference from ambient. However, the temperature of the air entering the top heat sinks, HS 1 and HS 3 has been first heated by the bottom heat sinks, HS 2 and HS 4. Taking into account the temperature rise of the fluid through the first heat sinks, HS 2 or HS 4, can be done using the simple energy balance $q = \dot{m}C_p\Delta T$ where $q = 8.32W$, and C_p is the heat capacity of air evaluated at the bulk mean temperature and $\dot{m}$ is the

approximated mass flow rate of air in the experiment produced by the fan. Using this approach, the corrected thermal resistances of each of HS 1 and HS 3 are presented in the last column of Table 2.1.

Table 2.1 - Averaged thermal resistance values obtained from experiments. The first value is the result without phase change interface material, and the second value is the result with phase change material.

Heat Sink Position	Thermal Resistance (°C/W)	Corrected Thermal Resistance (°C/W)
HS 1	10.2/9.2	9.4/8.5
HS 2	5.8/4.2	5.8/4.2
HS 3	8.9/5.5	8.1/4.8
HS 4	5.4/3.6	5.4/3.6
Average:	**7.6/5.6**	**7.2/5.3**

2.1.2 Finite Element Analysis Simulations:

The commercial heat sink was also modeled in COMSOL Multiphysics, drawn to the dimensions given in the datasheet. The heat source was given the same dimensions as the TO-247 package. An entrance region of 1X the length of the heat sink and an exit region of 5X the length of the heat sink is used to prevent undesired entrance and exit effects as recommended by Bons [4]. The heat source is modeled as a volume heat source of the same size as the TO-247 packaged resistors. An inlet velocity of 3.75m/s was applied at the channel inlet. This air velocity corresponds to a volumetric flow rate of 30L/s for the case of four heat sinks. A zero outlet pressure condition was applied at the exit. One heat sink, as opposed to all four, was simulated for simplicity. The duct sides have a symmetric boundary condition, which accounts for only modeling a portion of the full system. The symmetric boundary condition does not treat these boundaries as walls in the fluid flow, as it prescribes vanishing shear stresses [5]. Figure 2.3 shows the geometry and boundary conditions of the COMSOL model. Figure 2.3A shows a side view of the heat sink, while Figure 2.3B shows a top down view of the heat sink in the COMSOL model.

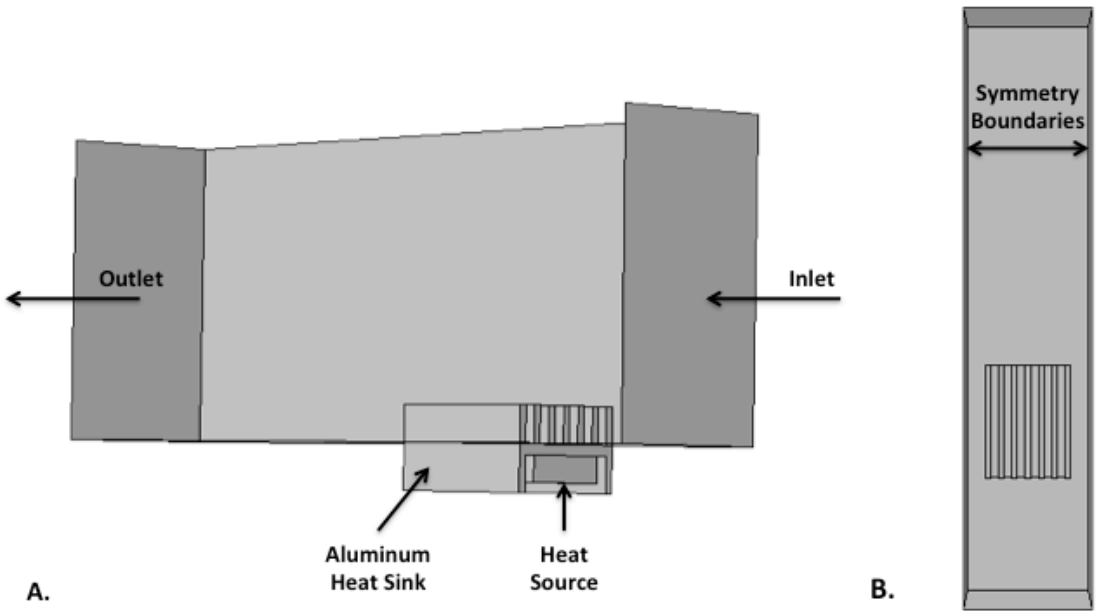

Figure 2.3 - COMSOL model geometry and boundary conditions.

The mesh is an automated physics-controlled mesh with 'Fine' sized elements. The elements are a combination of tetrahedrals, pyramids and prisms. The minimum element quality is 0.04. This is lower than the recommended minimum element quantity of 0.1 [6]. The average element quality is near 0.7, which is reasonable for a good mesh [6]. Thermal resistance values at a 'Normal' physics controlled mesh are compared to the 'Fine' physics controlled mesh in Table 2.2. The values between the two mesh types are less than 10%. Unfortunately, smaller than 'Fine' element sizes in the mesh lead to convergence errors and significantly longer computational time. Therefore, a 'Fine' sized mesh is used for the computations.

In order to ensure that the thermal resistance in the COMSOL model is independent of the heat source input, three different heat input values were applied to the model. The thermal resistance was nearly the same for each heat source value. Thermal resistance results are summarized in Table 2.2.

Table 2.2 - Comparison of thermal resistance values using two different meshes at different heat inputs.

Heat Input (W)	COMSOL Results/ Normal Mesh (°C/W)	COMSOL Results/ Fine Mesh (°C/W)	Percent Increase in Resistance Between Mesh Types
10	3.7	4.0	9.0%
8.32	3.6	4.0	9.4%
4	3.6	3.9	8.9%

A visual output of the simulation results is shown in Figure 2.4. Figure 2.4 shows the temperature profile with velocity magnitude streamlines of the COMSOL model solution for a heat source of 4W. Air enters at the back of the air channel and exits through the front as shown by the velocity streamline arrows.

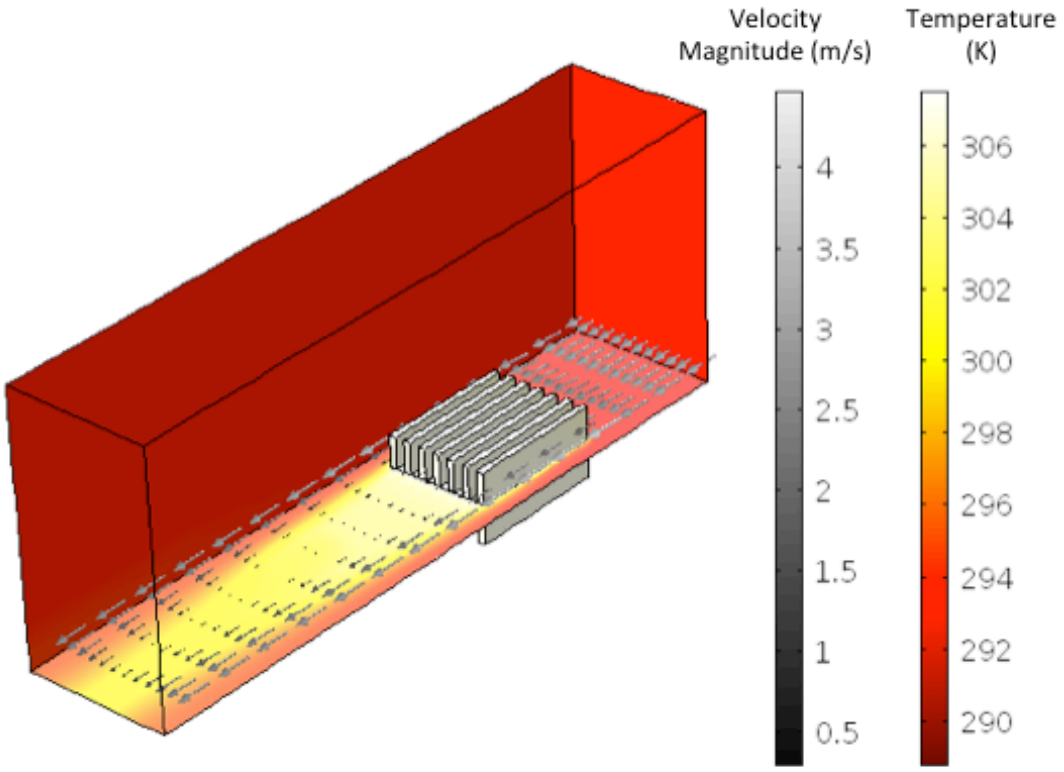

Figure 2.4 - Temperature profile with velocity streamlines for a heat input of 4W.

In order to model the interface between the heat source (resistor) and the heat sink that were experimentally tested, three different simulation cases were run. The first had perfect insulation between the heat source (resistor) and the aluminum heat sink. This simulation provides a theoretical minimum of the thermal resistance. The second had a thin interface resistance applied to the layer between the heat source and the heat sink to model the case of thermal interface material. As a first approximation, the thermal resistance of the interface material tested is estimated based on the thickness and thermal conductivity of the phase change material and the face area of the resistor in the TO-247 package (21.10 mm by 16.13 mm). This value is calculated to be 0.06°C/W, and was input into the COMSOL model.

The final model attempts to simulate the case of no interface material. The average drop in thermal resistance with the addition of phase change thermal interface material was experimentally observed to be 1.90°C/W. Taking the first approximation of the thermal resistance of the phase change material (0.06°C/W), an estimated thermal resistance of the interface without phase change material is 1.84°C/W. Based on the thermal conductivity of air, the average thickness of air between the heat sink and package is approximately 19.2μm, which is a reasonable value for surface roughness and irregularities and is discussed in more detail in Chapter 1. This condition was modeled in COMSOL as a thin layer of air with a defined thickness of 19.2μm.

2.1.3 Analytical Correlation Analysis:

It was also desired to model the experimentally tested case using theoretical correlations. The correlation chosen for this analysis is a composite developing and fully developed flow solution for a wide range of Reynolds numbers presented by Teerstra et al. [7]. The correlation is developed specifically for simultaneously developing flow in isothermal ducts. The correlation is said to hold true for working fluids with Prandtl numbers close to unity. This assumption holds true for most gases, including air and helium with Prandtl numbers close to 0.7. Unfortunately, for liquids, such as water, the Prandtl number has a much larger range with temperature. For water the Prandtl number ranges from 13.6 at 0°C to 1.7 at 100°C [8].

Teertstra et al. combine the fully developed and developing flow asymptotes into a composite solution for the Nusselt number with a characteristic length defined as the fin spacing, b, as:

$$Nu_b = \left[\frac{1}{\left(\frac{{Re_b}^{\star} Pr}{2}\right)^n} + \frac{1}{\left(0.664\sqrt{{Re_b}^{\star}} Pr^{\frac{1}{3}} \left(1 + \frac{3.65}{\sqrt{{Re_b}^{\star}}}\right)^{\frac{1}{2}}\right)^n} \right]^{-\frac{1}{n}} \tag{2.1}$$

where ${Re_b}^{\star} = Re_b \frac{b}{L}$ and the exponent is determined by the authors to be $n = 3$ to minimize the root mean square between modeled and numerically simulated data

performed by Teerstra et al. [7]. The subscript b in the dimensionless parameters indicates that the characteristic length is the fin spacing, b. The first term in the summation is the fully developed contribution, while the second term in the summation is the simultaneously developing flow solution presented originally by Sparrow [9].

The pressure drop for fully ducted flow is determined based on the calculations presented by Simons [10] as:

$$\Delta P = \left(K_c + 4f_{app}\frac{L}{D_h} + K_e\right)\rho\frac{V^2}{2} \tag{2.2}$$

where L is the length of heat sink channels in the flow direction, D_h is the hydraulic diameter of the flow channels, ρ is the density of fluid, V is the average velocity of fluid flowing through the channels. f_{app} is the apparent Fanning friction factor, and K_c and K_e are expansion and contraction loss coefficients.

The apparent Fanning friction factor is used to account for skin friction and changes in momentum rate, due to the changes in the shape of the velocity profile in the hydrodynamic entrance region. The Fanning friction factor used by Simons [10] is estimated based on the analysis by Muzychka and Yovanovich [11]. Muzychka and Yovanovich develop a relationship to encompass any duct length for a wide range of geometries by combining the relationships presented by Shah and London [12] for short and long ducts. Muzychka and Yovanovich determined an optimal exponent based on minimization of root mean square with other proposed models. The following is the optimized equation determined by Muzychka and Yovanovich [11]:

$$f_{app}Re = \left\{\left(\frac{3.44}{(L^{\star})^{\frac{1}{2}}}\right)^{n} + {fRe_{fd}}^{n}\right\}^{1/n} \tag{2.3}$$

where n is determined to be approximately 2, and fRe_{fd} is the fully developed friction factor. The relationship used by Culham and Muzychka [13] as well as Simons [10] for the fully developed friction factor is:

$$fRe_{fd} = 24 - 32.527\lambda + 46.721\lambda^2 - 40.829\lambda^3 + 22.954\lambda^4 - 6.089\lambda^5$$

where λ is the aspect ratio of the parallel channels, defined as the fin spacing divided by the fin height.

For parallel plate channels, the flow experiences compression and expansion losses at the entrance and exit of the channels. White [14] describes the sudden expansion as a theoretical loss by:

$$K_e = \left(1 - \frac{d^2}{D^2}\right)^2 \tag{2.4}$$

The sudden expansion coefficient can be described theoretically because the shear stress in the corner, dead fluid region, is negligible. Sudden contraction fluid flow is described by the vena contracta, where the main stream is forced to contract through a minimum diameter called the vena contracta. Unfortunately, this theory is complicated and not well described. The loss coefficient for sudden contraction is described as an empirical formula [14]:

$$K_c \approx 0.42\left(1 - \frac{d^2}{D^2}\right) \tag{2.5}$$

The empirical formula described experimental data well for values up to $\frac{d}{D} = 0.76$. For both Equation 2.4 and Equation 2.5, d is the width of the smaller region, and D is the width of the larger region.

The Nusselt number correlation (Equation 2.1) was used to predict the convective heat transfer coefficient of a commercially available heat sink. A flow rate was chosen for the analysis and the pressure drop was determined. The pressure drop calculated from the chosen flow rate is compared to the pressure drop given by the fan curve for the fan used in the experiment at the particular flow rate. This process was also used to evaluate the flow rate in the COMSOL simulation.

The chosen flow rate for simulation is 30L/s. This flow rate corresponds to the area of the fan itself. However, for both the COMSOL simulation and analytical analysis, only $1/4^{th}$ of the experimental system is evaluated (one of the four heat sinks). The 30L/s is scaled to $1/4^{th}$ the area of the fan to determine the flow rate corresponding to the COMSOL simulation and the analytical correlation. Both the analytical and COMSOL simulation have the same approach velocity, or free stream velocity. However, the analytical correlation does not take into account bypass flow, therefore the channel

velocity will be greater than the channel velocity in the COMSOL model, which does allow for bypass flow. A higher channel velocity will correspond to a higher pressure drop through the channel, which is observed. The experimental conditions most closely match those of the COMSOL model with bypass flow. Table 2.3 shows the results of the calculated pressure drop from the COMSOL simulation and the analytical correlation.

From the fan curve, the achievable volumetric flow rate at 1 mm H_2O is approximately 30L/s. The pressure drop corresponds well to the pressure drop calculated in COMSOL. The pressure drop in the COMSOL model is evaluated as a surface maximum as well as a surface average at the entrance plane of the channels. The exit is defined as zero pressure. The two values for pressure drop in the COMSOL simulation refer to the surface maximum (Max:) and surface average (Avg:).

Table 2.3 - Pressure drop results corresponding to a volumetric flow rate of 30 L/s based on the area of the fan.

COMSOL Results	Max: 11.2 Pa - Avg: 7.66 Pa (1.1-0.8mm H_2O)
Analytical Correlations	16.1 Pa (1.6 mm H_2O)

2.1.4 Experimental, Correlated and Simulated Results (Air):

Results for the experiment, COMSOL simulation, and analytical correlations are summarized in Table 2.4. The average of the experimental results for the bottom heat sinks, HS2 and HS4, and the corrected thermal resistance of the top heat sinks, HS1 and HS3, make up the average experimental result listed in Table 2.4.

Table 2.4 - Results from COMSOL simulation, experimental results and numerical correlation results for forced convection of simple finned heat sink.

Interface Resistance	**Average Experimental Results (°C/W)**	**Analytical Correlations (°C/W)**	**COMSOL Simulation Results (°C/W)**
Perfect conduction at interface	-	4.74	3.97
PCM thermal interface material	5.3	4.80	4.03
No thermal interface material, air gap ~21μm	7.2	6.76	5.92

It can be seen from Table 2.4 that the analytical and finite element analysis simulations give thermal resistance values that are slightly lower than the experimental results. The discrepancy may be due to incorrect assumption in the flow rate. For the analytical and COMSOL simulations the inlet condition is defined as a velocity. The velocity is calculated from a guessed volumetric flow rate that is based on the fan area. However, in the actual test experiment, the board blocks a portion of the fan flow area. In the experimental testing, the location of the fan greatly influenced the temperatures on the heat sink. If the heat sinks were placed centrally with respect to the fan, the temperature was higher than if they were in line with the perimeter of the fan. There is likely a stagnation zone in the center of the fan, which causes less flow through the fins and more flow around the outside of the fins. The average inlet velocity estimated from the fan curve is likely incorrect. Performing the experiments in a wind tunnel, or taking anemometer readings, would give a better estimate of the experimental flow rate and comparison between experimental and correlations and simulations would be more meaningful.

The COMSOL simulation predicts thermal resistance values that are slightly lower than the analytical correlations as can be observed in Table 2.4, but the simulation gives some insight into the flow through the channels and the air duct. Figure 2.5 shows a top down view of the velocity component in the y-direction, or the velocity through the fins. Some recirculation is observed at the exit of the channels as indicated by the negative velocity values in the y-direction (indicated by the dark blue color), causing more heat to be pulled off the ends of the fins than expected. The analytical model only accounts for convective heat transfer from the sides of the fin channels, and does not account for heat loss through the back of the fin. Figure 2.5 also shows that the velocity around the perimeter of the heatsink is much faster than the velocity between the fins. The analytical model does not take into account the additional heat transfer seen on the outside of the fins, due to the increased velocity, or through the fin tip. This additional heat transfer may account for the lower thermal resistance values in the COMSOL simulation.

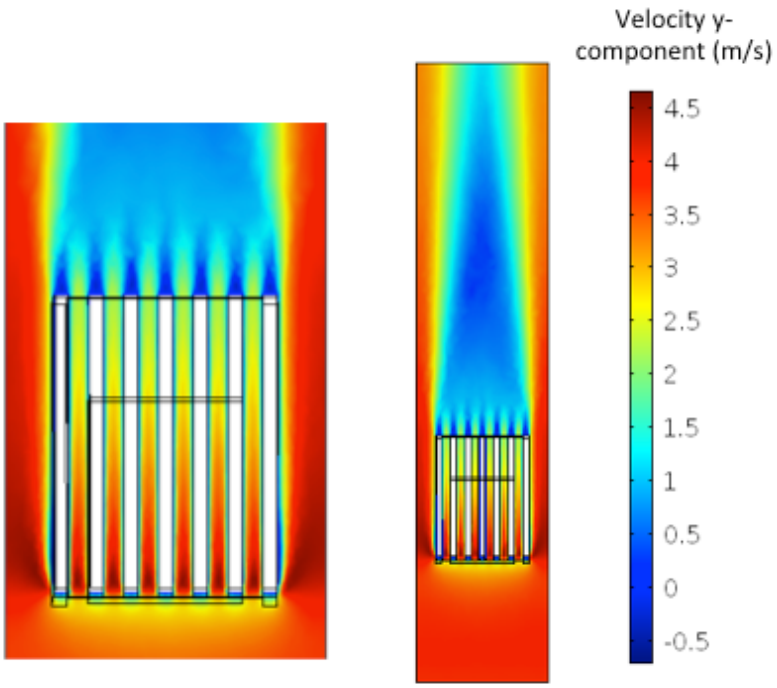

Figure 2.5 - Top down view of the velocity profile through the heat sink fins for air simulation

Figure 2.6 shows a side view of the velocity magnitude streamlines, and there is some flow bypass over the fins. This would cause the velocity through the fins to be lower than that imposed on the analytical model, which should cause a thermal resistance to be higher than that predicted by the analytical model. However, this is not the case, as the thermal resistances predicted by the analytical correlations are slightly higher than those predicted by the COMSOL model. The flow bypass would also cause the pressure drop through the fins to be less than that predicted in the analytical model, which is observed, and shown in Table 2.3. Overall, the COMSOL and analytical results for thermal resistance are near 10% of each other, which indicates good agreement.

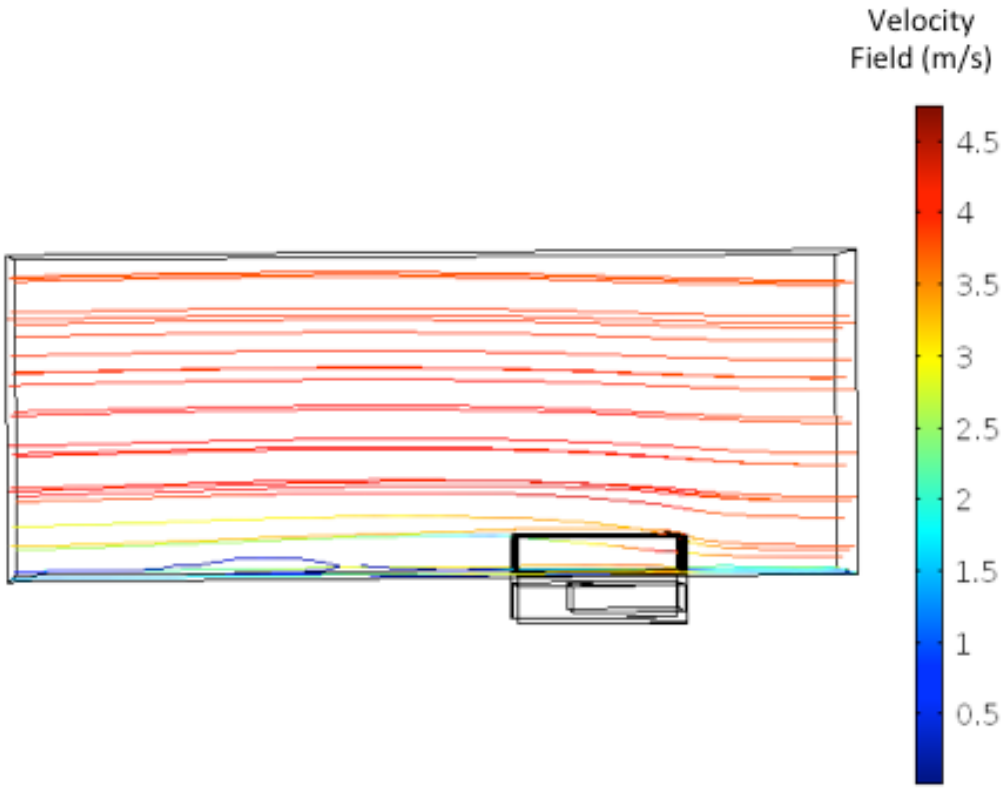

Figure 2.6 - Velocity streamlines in the Y-direction, viewed from the YZ-plane for air simulation

2.1.5 Correlated and Simulated Results (Helium & Water):

To compare COMSOL simulations to analytical correlations of different fluids, two additional fluids were considered. Helium gas is chosen for its low viscosity and relatively high thermal conductivity compared to other gases. Liquids have higher thermal conductivities than gases, however, they also have higher viscosities, which lead to greater pumping costs. In heat transfer applications, water has been the most popular choice among working fluids for its low cost and availability as well as its high heat capacity and thermal conductivity [15].

The COSMOL model is the same as the previously considered model with perfect insulation between the heat source and the heat sink. The model was run at a heat source of 8.32W and a normal inflow velocity of 3.75m/s for air, helium and water. Thermal resistance and pressure drop solutions from the COMSOL simulations are

shown in Table 2.5. Results from the analytical model for each fluid are given in Table 2.6.

Table 2.5 - Thermal resistance and pressure drop results from finite element simulation.

	Air	Helium	Water
Thermal Resistance (°C/W)	3.97	5.24	0.0980
Pressure Drop (Pa)	11.2 (max.) 7.66(avg.)	1.78 (max.) 1.07(avg.)	8540 (max.) 6020(avg.)

Table 2.6 - Thermal resistance and pressure drop results from the analytical correlation

	Air	Helium	Water
Thermal Resistance (°C/W)	4.42	2.06	0.0404
Pressure Drop (Pa)	16.1	6.86	6780

An interesting result is observed for helium in the COMSOL simulation. While it is expected that with thermal conductivity nearly an order of magnitude higher than air, the helium system would prove to have a lower thermal resistance than air. This result is observed in the analytical solution; however, the opposite result is observed in the finite element simulation.

The viscosity and the Prandlt number of air and helium are nearly the same in the temperature region of concern. The density of helium is lower than air so a slight decrease in pressure drop is expected. This is observed in the analytical solution and in the finite element simulation. However, pressure drop decreases to a much greater extent in the finite element simulation.

A closer look at the velocity streamlines in the finite element simulation offers some insight into the discrepancy. Figure 2.7 shows the streamlines of the velocity field, which can be compared to the velocity streamlines of air in Figure 2.6. It appears that there is more bypass flow in the case of the helium system than in the air simulation. There is also significant recirculation at the exit of the channels in the helium system. More bypass flow indicates less fluid flow between the channels, which would cause an

increase in the thermal resistance due to a decrease in the convective heat transfer. Figure 2.8 shows a top down view of the velocity component in the y-direction, or the velocity through the fins, which can be compared to Figure 2.5 for the simulation with air. It is clear from this view that less flow is going through the channels. A large portion of the helium that enters the channel exits the channel before it reaches the end of the fin. This would cause the thermal resistance as well as the pressure drop to be significantly lower than that predicted from the analytical correlation. The analytical correlation assumes a perfectly ducted geometry and does not consider bypass flow.

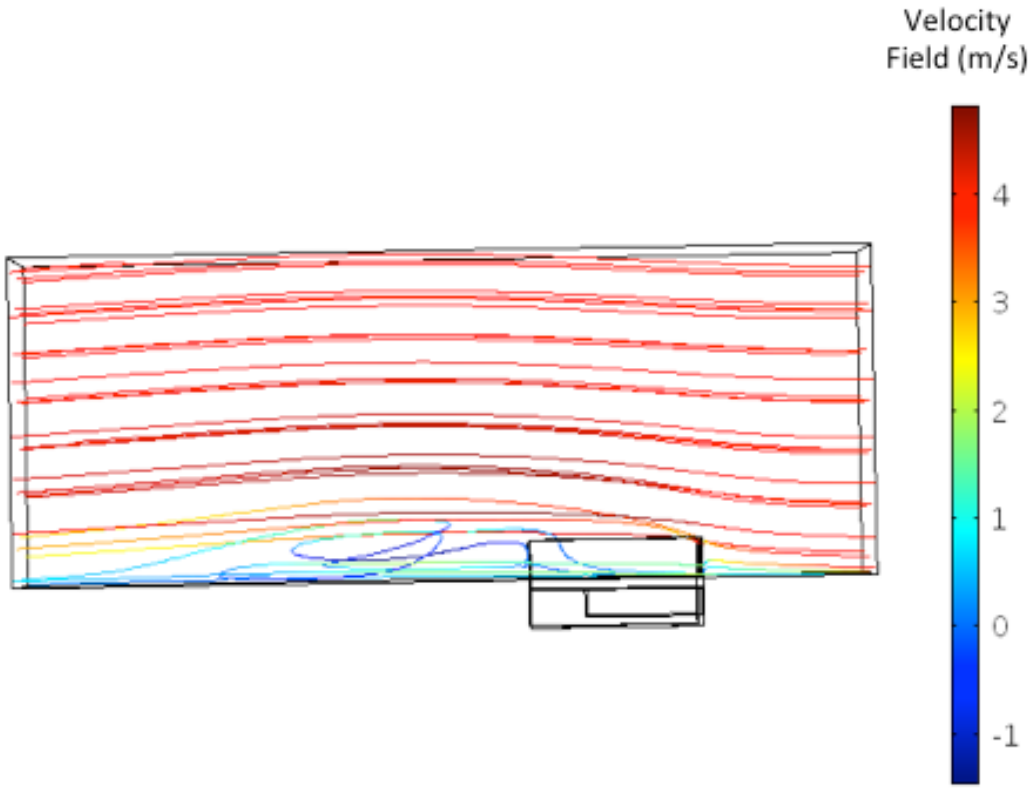

Figure 2.7 - Velocity streamlines in the Y-direction shown from the YZ-plane for the helium simulation

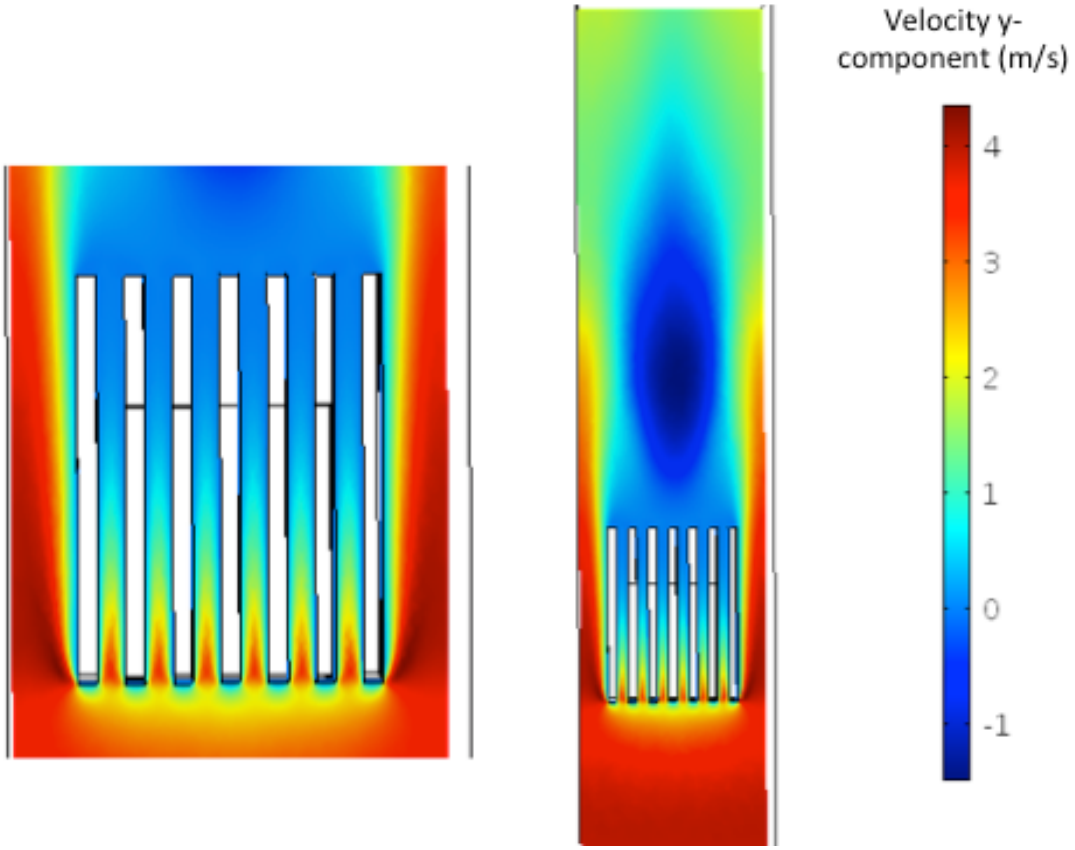

Figure 2.8 - Top down view of the velocity profile through the fins for the helium simulation

It is expected that the thermal resistance of the heat sink using water as the working fluid would significantly decrease, while the pressure drop significantly increases due to water's high thermal conductivity and viscosity when compared to air and helium. This result is observed in both the finite element simulation and analytical correlation. The thermal resistance predicted by the finite element model gives a thermal resistance that is slightly higher than the analytical correlation. Recall that the correlation is valid for fluids with Prandlt numbers near unity. The Prandlt number of water at the bulk mean temperature is 6.96. A Prandlt number greater than one indicates that the viscous diffusion rate is greater than the thermal diffusion rate. Therefore, the thermal boundary is developing at a slower rate than the viscous boundary layer, and the assumption of simultaneously developing flows at the same rate is no longer valid. The analytical model is assuming a faster thermal diffusion with respect to the viscous diffusion. This corresponds to predicted higher heat transfer

ability, which in turn results in lower thermal resistance predictions. The analytical model does predict a lower thermal resistance when compared to the COMSOL model.

That being said, the analytical model does not deviate from the COMSOL simulation by a significant amount. Therefore, it can be concluded that for reasonable temperature ranges, this particular analytical correlation that was developed for Prandlt number near unity can be used to obtain a reasonable approximation for a systems with higher Prandlt numbers. The pressure drop calculated analytically is near the average pressure drop observed in the COMSOL simulation. The analytical pressure drop analysis is not limited to fluid type, only fluid flow type. Therefore, as long as the system has laminar flow, one would expect the analytical prediction of pressure drop to be near that of the COMSOL simulation.

2.1.6 Liquid Cooling in Microchannel Geometries:

As seen from the previous comparison between air and helium gases to liquid water, liquid cooling can have much lower thermal resistance values. However, liquids also have higher viscosities, which cause the required pumping power to be greater than that for gases, such as air and helium. Liquid cooling can be advantageous in high heat applications that are space limited. There are many correlations that have been established to predict the convective heat transfer coefficient of liquid cooled systems. Reference 16 provides a good summary of liquid cooled correlations for typical cold plate geometries.

One area where liquid cooling is well-explored is in microchannel applications. Liquid cooled microchannels can have very high heat dissipation rates for very little area footprint. There is also interest in applying liquid cooled microchannel heat transfer to electronic packaging design for direct chip cooling, since microchannels may be etched into the electronic die and cooled at the chip level.

Tuckerman and Pease [17] were the first to look at microchannel forced convection for the cooling of electronics at the package level. Their studies looked at forced convection with water in chemically etched microchannels, and showed the need for small channel widths, and propose that a lower limit on channel size is determined

by fluid viscosity. With a practical limit on pressure drop, an optimum channel width, D, is determined to minimize the thermal resistance.

Tuckerman and Pease based their optimal geometry on a water-cooled silicon heat sink on a 1cm by 1cm substrate base, with a water pressure of P=30psi. Based on these system conditions, they obtained optimal geometry, summarized in Table 2.7 for a volumetric flow rate of $f = 11cm^3/s$, where w_c and w_w are the channel width and fin width respectively, and z is the depth of the channel. θ is the predicted thermal resistance. A drawing of their microchannel geometry is shown in Figure 2.9.

Table 2.7 - Tuckerman and Pease [17] optimized geometry

Tuckerman & Pease Optimum Geometry	
$w_c = w_w$	57μm
z	365μm
θ	0.086°C/W

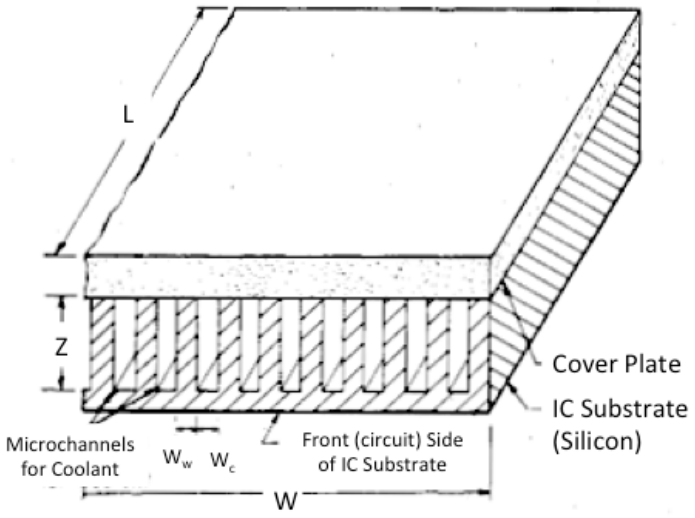

Figure 2.9 – Tuckerman and Pease [17] geometry

Tuckerman and Pease performed three experiments at near optimum conditions. The microchannels were etched vertically into silicon wafers using KOH. A Pyrex cover plate was bonded over the channels, using deionized water at 23°C, and a thin-film WSi_2 resistor of 1cm by 1cm to supply heat to the channels. Inlet and outlet water temperatures were measured as well as the heater resistor at the downstream

end in attempt to record the highest temperature of the resistor. Tuckerman and Pease were able to confirm that the thermal resistance was independent of power level [17].

Using the same geometry, finite element analysis in the program COMSOL, showed reasonable agreement with the experimental data obtained by Tuckerman and Pease. The finite element analysis model consisted of one hundred microchannels each with a width of w_c and depth of z, spaced w_w apart. The top and bottom plates were 0.05cm in thickness, and the entire system has an area of 1cm by 1cm to replicate the Tuckerman and Pease experiments. The channel walls, top and bottom plates of the model are specified as silicon and the fluid within the channel is specified as water. The fluid flow is defined as an entrance pressure at the inlet of each channel, where as the outlet is defined as zero pressure. A boundary inward heat flux is applied to the bottom of the bottom plate and inlet fluid temperature is defined as 23°C at the entrance of each channel.

The mesh consisted of a free triangular boundary mesh on the outer edge of the first channel wall. This boundary mesh was then swept through the domains of each channel and channel wall, and then swept upward and downward through the top and bottom plates. Corner and boundary layer mesh refinements were also used. A stationary study was performed for each experiment performed in the Tuckerman and Pease analysis. Results and comparison of the COMSOL model and the experimental data obtained by Tuckerman and Pease is given in Table 2.8.

Table 2.8 - Finite element analysis simulation results compared to results obtained by Tuckerman and Pease [17]

Expt	Wc(um)	Ww(um)	z(um)	Heat Flux (W/cm^2)	Experimental Thermal Resistance (deg C/W)	COMSOL Model Thermal Resistance (deg C/W)	Percent Error from Model to Experiments
1	56	44	320	181	0.110	0.094	17%
2	55	45	287	277	0.113	0.094	20%
3	50	50	302	790	0.090	0.069	30%

It can be seen from the Table 2.8 that the COMSOL model predicts thermal resistances that are approximately 0.02°C/W lower than what Tuckerman and Pease found in their laboratory experiments. This may be explained by the nature of modeling

itself. The COMSOL model is an idealized case, as opposed to the real laboratory experiments. The COMSOL model does not take into account contact resistance between the top plate and the channels. It also does not take into account viscous heating of the fluid or any heat losses that may be experienced from the top, bottom, and sides of the heat sink that would occur in a laboratory setting.

Tuckerman and Pease asserted that in their experiments the thermal resistance was independent of power level. Using the parameters of the third experiment, the heat flux input from the COMSOL model was varied from 100W/cm^2 to 800W/cm^2. It was found that the thermal resistance decreased with an increase in heat flux. The decrease in thermal resistance could be due to an increase in temperature and therefore a variation of the fluid properties of water, which are temperature dependent in the COMSOL model. Two further studies were conducted, one with constant fluid properties that are calculated at a temperature of 26.5°C and one with constant fluid properties that are calculated at 50.5°C. These two temperatures correspond to the bulk mean temperature as calculated from the temperature dependent properties for 100W/cm^2 and 800W/cm^2 respectively. A plot of thermal resistance versus heat flux input for both constant fluid properties and fluid properties as a function of temperature is shown in Figure 2.10. It can be seen from Figure 2.10 that the constant fluid properties are nearly independent of the inward heat flux. However, there is a deviation at low heat fluxes.

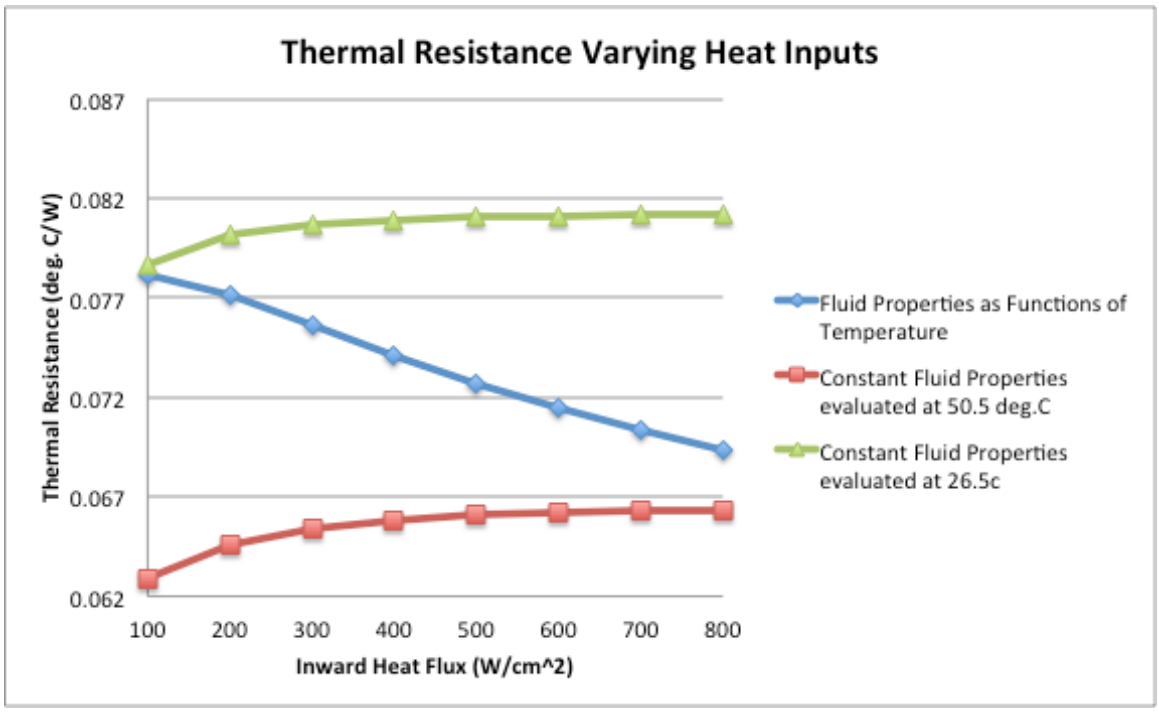

Figure 2.10 - Thermal resistance as a function of the heat input into the finite element simulation. Fluid properties are evaluated using different methods.

A better way of evaluating the COMSOL data to obtain the thermal resistance may be to look at a plot of the rise in temperature above ambient as a function of the heat flux. The slope of this plot would give the rise in temperature divided by the heat flow, which is the definition of the thermal resistance. For the COMSOL simulation with fluid properties as a function of temperature, the plot of rise in temperature as a function of the heat flux is shown in Figure 2.11. It can be seen from this plot that the temperature rise as a function of the heat flux is nearly linear, with a slope of 0.0712°C/W. This value of thermal resistance shows reasonable agreement with the value calculated at 600W/cm^2.

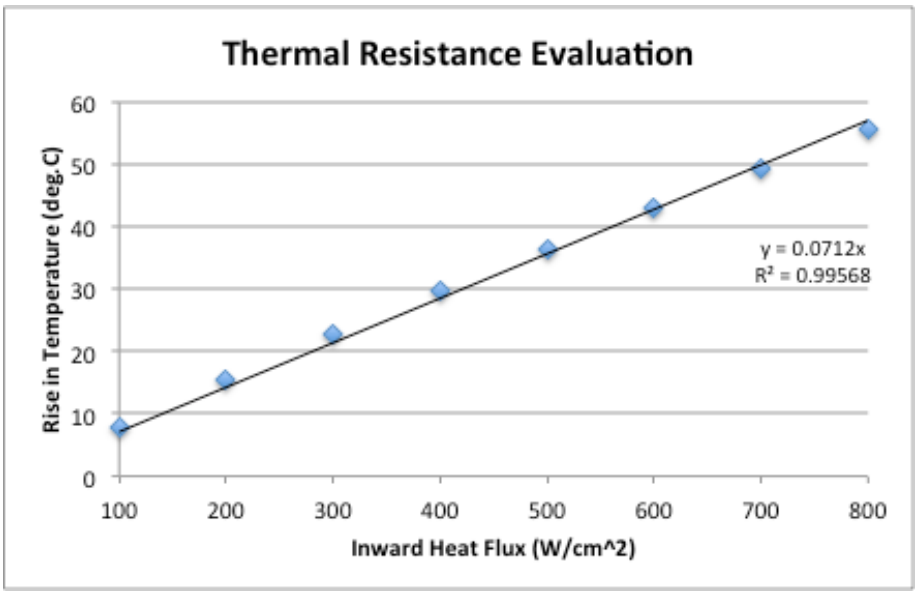

Figure 2.11 - Temperature difference between ambient fluid and heat sink surface as a function of the heat input to the finite element simulation.

While microchannels greatly reduce the thermal resistance, they are not typically used because of the high-pressure drop associated with small hydraulic diameters. Another difficulty experienced with microchannels is that there are typically large temperature gradients across from the inlet to outlet location causing inconsistent cooling throughout the heat sink [18]. There are also manufacturing limitations; wall thickness of 35μm represents the minimum thickness that can be easily manufactured with typical fabrication technology [19].

Another parametric sweep was performed on the third experiment from the Tuckerman and Pease analysis. This time the inlet water temperature was varied from 23°C to 58°C, as it has been shown that warm water-cooling can improve the efficiency of the cooling system [20]. Warm water-cooling has been successfully used to cool data centers [21] with less energy input. The results of the parametric sweep of the Tuckerman and Pease microchannel are shown in Figure 2.12. The thermal resistance is plotted in Figure 2.12 as a way to measure the thermal efficiency. The results here indicate that using warmer water is more thermally efficient than using cold water as the thermal resistance decreases as the inlet water temperature increases. However, when trying to cool something below a specified temperature, such as in electronics, using warmer water may not be feasible. In the parametric sweep simulation, the maximum temperature of the heat sink does increase with an increase in water

temperature. However, the temperature of the heat sink does not increase by the same amount as the inlet temperature. As the inlet temperature increases, the difference between the heat sink temperature and inlet temperature decreases, causing a decrease in the thermal resistance or efficiency of the heat sink. If the system can be maintained at a reasonable temperature with the use of warmer water, the overall efficiency of the cooling system can be increased. This becomes an optimization problem based on the required temperatures.

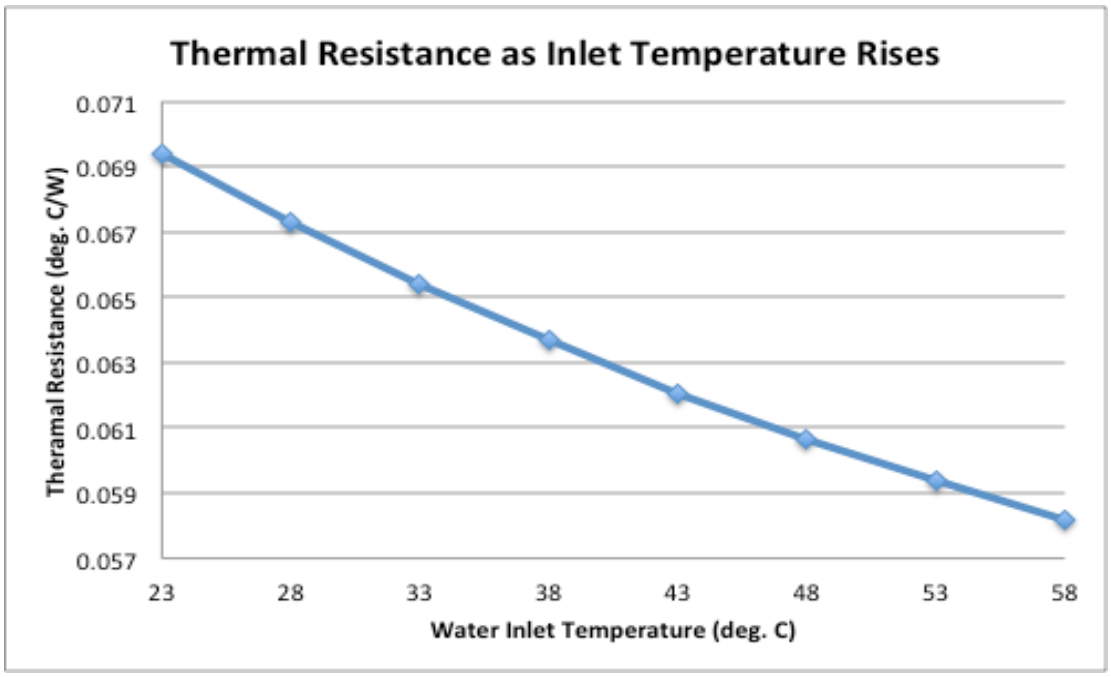

Figure 2.12 - Finite element simulation results for a parametric sweep of inlet water temperature on the Tuckerman and Pease microchannel system.

2.2 Natural Convection:

Similar to the analysis done for forced convection, experimental tests, finite element analysis simulations, and analytical correlations are used to characterize the commercially available parallel plate heat sink in a natural convection environment. In natural convection, orientation with respect to gravity can have a significant effect on thermal performance. Both horizontally oriented and vertically oriented fins are considered in experiment and finite element simulation.

2.2.1 Experimental Testing:

In addition to the forced convection orientation, two natural convection orientations were tested. One experiment was conducted with horizontal fins, fins parallel to the table's surface, and perpendicular to the direction of gravity. A top down view of this orientation can be seen in Figure 2.13. The other experiment was conducted with vertical fins, fins perpendicular to the table's surface and parallel to the direction of gravity. A side view of this orientation can be seen in Figure 2.14. The experiments were conducted using the same method as the forced convection tests. Starting with no phase change thermal interface material, a target of no greater than 100°C steady state temperature for each orientation was achieved. The power input that was required to reach 100°C steady state temperature was 4.05W for the horizontal fins and 4.26W for the vertical fins. The same power input was used for the tests with thermal interface material and without thermal interface material. Three trials of each orientation with and without thermal interface material were run and the average temperature for each test was determined. Averaged thermal resistance results are shown in Table 2.9.

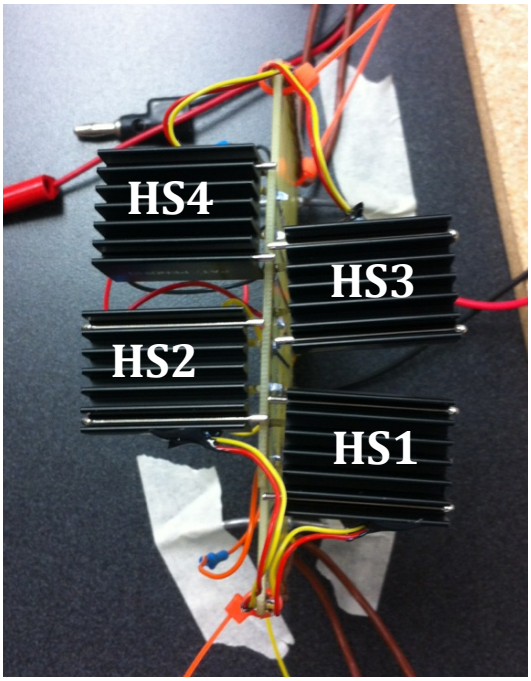

Figure 2.13 – Test set-up for fins that are perpendicular to gravity (horizontally oriented fins)

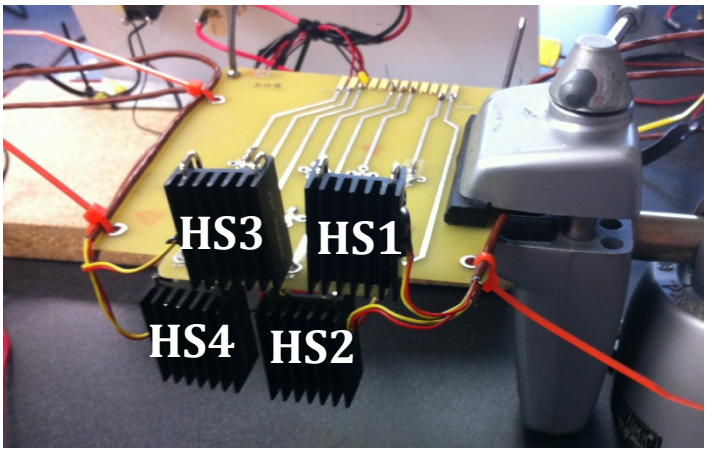

Figure 2.14 – Test set-up for fins that are parallel to gravity (vertically oriented fins)

Table 2.9 - Averaged thermal resistance values obtained from experiments. First number is results without phase change interface material, and the second number is the result with phase change thermal interface material.

Heat Sink Position	Horizontally Oriented Fins (°C/W)	Vertically Oriented Fins (°C/W)
HS 1	18.82/ 17.47	19.10/17.68
HS 2	17.91/16.80	16.63/14.91
HS 3	17.99/14.69	19.74/15.82
HS 4	17.91/16.88	17.24/14.96
Total Average:	**18.16/16.46**	**18.18/15.84**

From Table 2.9 it can be seen that the horizontally oriented finned heat sinks have roughly the same temperature between positions, whereas the vertically oriented finned heat sinks in position HS1 and HS3 have higher thermal resistances than the heat sinks in position HS2 and HS4. In the forced convection condition, the top heat sinks are receiving warmer inlet air than the bottom heat sinks (HS2 and HS4), and an estimate of this rise in fluid temperature is used to correct the heat sink thermal resistance. However, in natural convection the top heat sinks are warmer due to density changes in air. When air is heated, the density decreases, and the warm air rises, toward the top heat sinks, whereas the cooler air sinks, toward the bottom heat sinks. This is why the top heat sinks have observably higher thermal resistances than the bottom heat sinks.

2.2.2 Finite Element Analysis Simulation:

A finite element simulation for natural convection was also conducted in COMSOL Multiphysics. For natural convection simulation, a spherical ambient domain

of three to five times the diameter of the component is recommended [4]. The commercial aluminum heat sink, drawn in COMSOL using the dimensions given by the manufacturer is centrally placed in a spherical air domain with a diameter of 150mm, which is about five times the longest length of the heat sink. An open boundary temperature condition of 300K is imposed on the surface of the spherical air domain. An open flow boundary is also imposed on the surface of the spherical air domain. A block, corresponding to the dimensions of the TO-247 package, is placed on the backside of the heat sink and is assigned a volume heat flux. A fluid volume force is assigned to the entire spherical air domain, which accounts for the effects of gravity.

Two distinct simulations were performed. One had the gravity volume force in the Z-direction, with the fins oriented perpendicular to gravity or with the length of the fins going in the Y-direction. This corresponds to horizontally oriented fins. The other has a volume force with gravity acting in the Y-direction, with the fins oriented parallel to the Y-direction, which corresponds to vertically oriented fins. These two different simulations were performed to capture the two different natural convection orientations that were performed. For the horizontal fin simulation, the volume heat flux applied to the heat source block is 4.05W. For the vertical fin simulation, the volume heat flux applied to the heat source block is 4.26W. These correspond to the heat that was input into the resistors for the experimental tests. Both simulations were additionally performed with a 10W heat source to compare to the heat sink datasheet. The heat sink manufacturer gives a rated thermal resistance of 12°C/W at 10W heat dissipation [22].

Unfortunately, the simulation was unable to converge on a steady state solution. This is likely due to the unsteady nature of natural convection fluid flow. Results from a time dependent solutions are shown in Figure 2.15. From Figure 2.15 it can be seen that a steady state solution is approached for each simulation. The approached steady state solutions are summarized in Table 2.10.

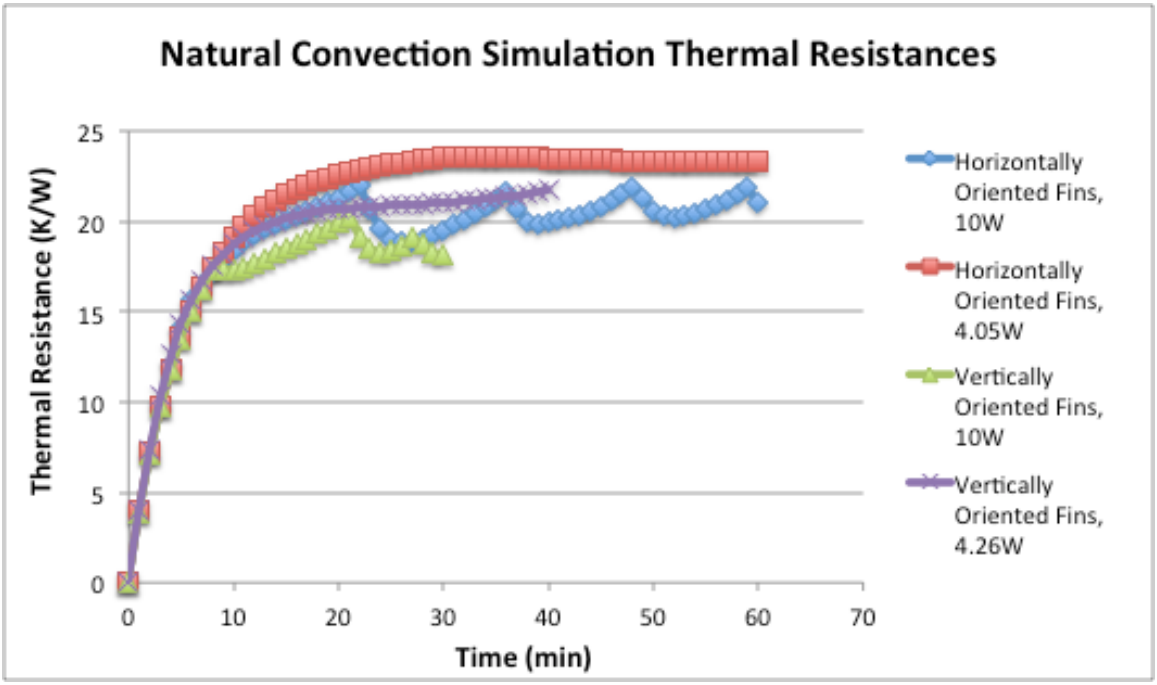

Figure 2.15 - Finite element time dependent solutions for natural convection analysis

Table 2.10 - Approached steady state solutions for natural convection finite element simulations

	Horizontally Oriented Fins (10W)	**Horizontally Oriented Fins (4.05W)**	**Vertically Oriented Fins (10W)**	**Vertically Oriented Fins (4.26W)**
Thermal Resistance (°C/W)	20.5	23.4	19.0	21.0

The thermal resistance obtained from the COMSOL simulation are quite a bit higher than the value of 12°C/W given in the datasheet for natural convection at 10W heat dissipation. Because it is unclear how the heat sinks were tested, it is difficult to compare the differences. As expected, the thermal resistance for the vertically oriented fins is lower than the thermal resistance for the horizontally oriented. For the case of the vertically oriented fins, the fins are parallel to the direction of gravity, and fluid moves through the fin channels, as opposed to horizontally oriented fins, where the fluid only moves from the base of the heat sink to the tip of the fin.

The thermal resistance should be independent of the heat load. However, as seen for the case of forced convection with water, the fluid properties at different temperatures can play a role in determining the thermal resistance. Because natural convection relies

on temperature dependent properties, it is expected that the thermal resistance may vary with the magnitude of the heat load. At higher heat source values, 10W, the temperature difference between the ambient condition and the heat sink temperature is greater. Therefore, more fluid flow is induced causing greater heat transfer and lower thermal resistance values, which is observed in the simulation results. From Figure 2.15 it can be observed that there is more variability in the thermal resistance at the high heat source value of 10W. This may also be due to the increased fluid motion at higher heat fluxes due to a greater temperature gradient in the fluid.

2.2.3 Experimental & Simulation Results:

Experimental results with thermal interface material are compared to the simulation results for thermal resistance in Table 2.11. The simulation did not take into account contact resistances and therefore should more closely represent the experimental results with thermal interface material than without interface material. The simulation results for both orientations provide higher thermal resistance values than the experimental results. This is the opposite of what is expected, as the simulation does not take into account the additional resistance that would be observed due to the imperfect thermal contact between the resistor and the heat sink. It is likely that the experimental tests were not solely natural convection tests. The experimental results were conducted in the summer months. The room in which the experiment was conducted had the air conditioning running, and cold air blowing out of the ducts likely caused more air circulation in the room than what would be expected solely by natural convection. The finite element analysis simulation is considering a perfectly controlled test environment. More airflow in the testing room would cause the thermal resistance to be less than what is predicted by the simulation.

Table 2.11 - Experimental and finite element analysis results of thermal resistance.

Thermal Resistance	Simulation	Experimental Results (HS2, HS4) with TIM	Experimental Results (HS1, HS3) with TIM
Horizontal Fins (4.05W)	23.4 °C/W	16.84 °C/W	16.08 °C/W
Vertical Fins (4.26W)	21.0 °C/W	14.94 °C/W	16.75 °C/W

2.2.4 Analytical Correlations:

Natural convection, much like forced convection, has been modeled using analytical correlations. Elenbaas is often considered the pioneer of parallel plate natural convection analysis [1]. His studies of vertical channel natural convection have been confirmed numerically, and proven to apply to both isothermal plates as well as constant heat flux conditions. Similar to forced convection, natural convection fluid flow can be described as either developing or fully developed. Long narrow channels have flow that develops quickly through the channel, while short channels may have a significant portion of developing flow. Fully developed flow occurs when both the momentum and thermal boundary layers between plates interact. In fully developed flow the heat transfer coefficient can be assumed to be constant along the fin. However, this assumption implies temperature independent fluid properties [1]. The fin gap based Nusselt number is often related to the fin gap based Rayleigh number often referred to as the Elenbaas number:

$$Ra_b = El = \frac{\rho g \beta c_p b^4 (T_w - T_\infty)}{\mu k L} \tag{2.6}$$

for isothermal plates, where b is the space between the plates, T_w is the wall temperature, T_∞ is the ambient fluid temperature, L is the length of the channel, β is the coefficient of thermal expansion, g is acceleration due to gravity, and ρ, μ, and k are the density, viscosity and thermal conductivity of the fluid. Elenbaas established a well-known correlation that relates the gap based Nusslet number to fluid properties for relatively short plates, spaced a length z apart in air [1]:

$$Nu_0 = \frac{hz}{k} = \frac{El}{24}\left(1 - e^{-35/El}\right)^{3/4} \tag{2.7}$$

Reference 1 provides a summary of fully developed as well as the isolated plate limit of Nusselt number solutions for isolated plate natural convection in two-dimensional channels.

There have been many studies further progressing the Elenbaas correlation to apply to vertically oriented fins. Bilitzky [23] developed a correlation specifically for closely spaced, short fins, which typically exhibit higher convective heat transfer coefficients than the predicted Elenbaas correlation [1]. The higher heat transfer coefficients have been attributed to significant inflow from the open front edges of the channels. These types of low profile finned heat sinks are typical used in the electronic industry [1], which makes the Bilitzky correlation of special interest to this project. Bilitzky's correlation is built upon a correlation established by Van de Pol and Tierney [24]. Van de Pol and Tierney incorporated the channel aspect ratio as well as differences in fin thickness into the Elenbaas correlation by the introduction of an additional geometric parameter. Van de Pol and Tierney also made the change of using the hydraulic diameter as opposed to the fin spacing as the characteristic length in the Nusselt number. Bilitzky modified the geometric parameter established by Van de Pol and Tierney by adding a purely geometric factor that takes into account fin tip inflow to the overall channel. The geometric parameter is described as:

$$\psi_B = \frac{24\Lambda_1}{\left(\left(1 + \frac{a}{2}\right)(1 + \Lambda_2\Lambda_3)\right)^2} \tag{2.8}$$

Where:

$$\Lambda_1 = 1 - 0.483e^{-0.17/a} \quad \Lambda_2 = 1 - e^{-0.83a} \quad \Lambda_3 = 9.14a^{1/2}e^{-B} - 0.61$$

and a is the channel aspect ratio $\left(a = {}^{b}/_{h}\right)$, and B is the geometric factor introduced by Bilitzky [23]:

$$B = 1.25\left(1 + \frac{b}{2h}\right) \tag{2.9}$$

where h is the channel height and b is the channel spacing. The modified Elenbaas correlation with the use of the geometric parameter is then given by:

$$Nu_{d_h} = \frac{El_{d_h}}{\psi_B}\left(1 - e^{\left(-\psi_B\left(\frac{0.5}{El_{d_h}}\right)^{\frac{3}{4}}\right)}\right) \tag{2.10}$$

where the subscript d_h indicates the characteristic length is the hydraulic diameter, where for a channel $d_h = \frac{2hb}{2h+b}$.

The Elenbaas and Bilitzky correlations were solved for the vertically oriented experimentally tested heat sink. Because these correlations are based on an isothermal wall temperature, the wall temperature from the COMSOL simulations and experimental results is input into the model. This gave three different solutions for the correlations corresponding to the three different temperature conditions applied to the model. These three temperature conditions can be described as:

- COMSOL average temperature corresponding to 4.26W
- COMSOL average temperature corresponding to 10W
- Experimental average temperature results

The material properties are evaluated at the heat sink surface temperature, with the exception of the volume expansion coefficient, which is evaluated at the fluid temperature. The heat flux is then calculated based on the convective heat transfer coefficient and is compared to the heat flux input into the finite element simulation model and experimental test. The temperature difference between the wall and the ambient fluid is divided by the calculated heat flux to obtain the thermal resistance. This thermal resistance is then compared to the thermal resistance obtained experimentally and by finite element simulations.

Correlation results are summarized in Table 2.12- Table 2.14. The Elenbaas correlations consistently predict less heat transfer and therefore higher thermal resistance than the Bilitzky correlation predictions. The predicted thermal resistance values for the 10W solution are less than that for the 4.26W solution. This is consistent with what is observed in the finite element analysis simulations.

Both the Elenbaas and Bilitzky correlations predict lower heat transfer, higher thermal resistances, than the simulated results and the experimental results. The COMSOL simulation takes into account temperature dependent fluid properties. The results from the correlation assume constant fluid properties at the heat sink surface temperature, with the exception of the expansion coefficient, which is evaluated at the fluid temperature. The discrepancy between correlation results and simulation and experimental results could be due to the temperature dependence of the fluid properties. The correlations predict significantly higher thermal resistances for the experimental conditions than the experimental results. This further confirms the theory that the experimental test conditions had additional airflow that increased the heat transfer from the natural convection heat sinks.

Table 2.12 - Analytical correlation results evaluated with the heat sink surface temperature obtained from the finite element simulation with a heat input of 10W. The corresponding thermal resistance by COMSOL simulation was determined to be 19.0°C/W (from Table 2.10).

	Elenbaas Correlation	**Percent Rise in Correlation Result**	**Bilitzky Correlation**	**Percent Rise in Correlation Result**
Heat Flux (W)	5.9	41%	7.9	21%
Thermal Resistance (°C/W)	34.9	45%	25.9	26%

Table 2.13 - Analytical correlation results evaluated with the heat sink surface temperature obtained from the finite element simulation with a heat input of 4.26W. The corresponding thermal resistance by COMSOL simulation was determined to be 21.0°C/W (from Table 2.10).

	Elenbaas Correlation	**Percent Rise in Correlation Result**	**Bilitzky Correlation**	**Percent Rise in Correlation Result**
Heat Flux (W)	2.6	39%	3.3	23%
Thermal Resistance (°C/W)	37.3	44%	28.6	27%

Table 2.14 - Analytical correlation results evaluated with the experimental temperature conditions. The average thermal resistance obtained by experiment is 15.8°C/W (from Table 2.9) for a heat flux of 4.26W.

	Elenbaas Correlation	**Percent Rise in Correlation Result**	**Bilitzky Correlation**	**Percent Rise in Correlation Result**
Heat Flux (W)	1.6	62%	2.1	51%
Thermal Resistance (°C/W)	38.8	59%	30.3	48%

2.3 Conclusions:

This chapter considers methods of predicting thermal resistance values of parallel plate heat sinks. Heat transfer in parallel plate heat sinks is dominated by convection. Experimental results, finite element analysis simulations, and analytical correlations for both forced and natural convection parallel plate heat sinks were evaluated.

As seen from the examples presented in this chapter, heat sink correlations are helpful in getting an order of magnitude type solution. Unfortunately, they can be quite limited to highly simple geometries, such as parallel plates. They can also be limited by a vast number of assumptions, such as isothermal or adiabatic boundary conditions or even limited to the fluid type. Correlations are also difficult to use because there are a wide variety from which to choose. This is where computational fluid dynamics can be helpful. However, computational fluid dynamics usually requires expensive programs and a significant amount of time and expertise in running the programs. Experimental testing of prototype remains one of the most useful tools in heat sink characterization [25].

References:

[1] A. D. Kraus and A. Bar-Cohen, *Design and Analysis of Heat Sinks*, New York, NY: John Wiley & son, Inc., 1995.

[2] S. Kakac and Y. Yener, "Laminar Forced Convection in Pipes and Ducts," in *Convective Heat Transfer*, 2nd ed., Boca Raton, FL: CRC Press, Inc., 1995, ch. 6, pp. 119-180.

[3] L.T. Yeh and R.C. Chu, "Heat Transfer Correlations," in *Thermal Management of Microelectronic Equipment: Heat Transfer Theory, Analysis Methods, and Design Practice,* New York, NY: ASME Press, 2002, pp. 381-399.

[4] R. Bons. Siemens Webinar, Topic: "Best practices for forced & natural convection cooling simulation," Dec. 15, 2016.

[5] Fluid Flow Interfaces Reference Manual, "Symmetry," COMSOL Multiphysics® v. 5.1. COMSOL AB, Stockholm, Sweden. 2015.

[6] A. Griesmer. (2014). *Size Parameters for Free Tetrahedral Meshing in COMSOL Multiphysics* [Online]. Available: https://www.comsol.com/blogs/size-parameters-free-tetrahedral-meshing-comsol-multiphysics/

[7] P. Teertstra, M. M. Yovanovich, J. R. Culham, T. Lemczy, "Analytical Forced Convection Modeling of Plate Fin Heat Sinks." in *5th IEEE SEMI-THERM Symp.,* 1999, pp. 34-41.

[8] J. R. Welty, C. E. Wicks, R. E. Wilson, G. L. Rorrer, "Physical Properties of Gases and Liquids" in *Fundamentals of Momentum, Heat, and Mass Transfer, 5th ed.,* Jefferson City, MO: John Wiley & Sons, Inc., 2008, App. I, pp. 678-690.

[9] E.M. Sparrow, "Analysis of Laminar Forced-Convection Heat Transfer in Entrance Region of Flat Rectangular Ducts," *NACA Technical Notes 3331*, 1955.

[10] R.E. Simons (2003). *Estimating Parallel Plate-fin Heat Sink Pressure Drop* [Online]. Available: https://www.electronics-cooling.com/2003/05/estimating-parallel-plate-fin-heat-sink-pressure-drop/

[11] Y.S. Muztchka and M.M Yovanovich, "Modeling Friction Factors in Non-Circular Ducts for Developing Laminar Flow," in *Proc. 2nd AIAA Theoretical Fluid Mech. Meeting,* Albuquerque, NM, 1998.

[12] R.K. Shah and A. L. London, "Parallel Plates," in *Laminar Flow Forced Convection in Ducts*, United Kingdom: Academic Press, 1978, ch. 6, pp. 153-195.

[13] J.R. Culham, Y.S. Muzychka, "Optimization of Plate Fin Heat Sinks Using Entropy Generation Minimization". *IEEE Trans. Compon. Packag. Technol.,* vol. 24, no. 2, pp. 159-165, Jun. 2001.

[14] F.M. White, "Viscous Flow in Ducts," in *Fluid Mechanics, 7th ed.*, New York, NY: McGraw-Hill, 2011, ch. 6, sec. 6.8, pp. 379-388.

[15] S. Zimmermann et al., "Hot Water Cooled Electronics for Higher Exergetic Utility," in *Proc. Of the ASME Summer Heat Transfer Conference*, Rio Grande, Puerto Rico, 2012.

[16] L.T. Yeh and R. C. Chu, "Advanced Cooling Technologies I; Single-Phase Liquid Cooling," in *Thermal Management of Microelectronic Equipment: Heat Transfer Theory, Analysis Methods, and Design Practices*, New York: ASME Press, 2002, ch. 14, pp. 261-279.

[17] D.B. Tuckerman and R.F.W. Pease, "High-Performance Heat Sinking for VLSI". *IEEE Electron Device Lett.,* vol. 2, no. 5, pp. 126-129, Mar. 1981.

[18] J.H. Ryu, D.H. Choi, S.J. Kim, "Numerical optimization of the thermal performance of a microchannel heat sink," *J. Heat Trans.*, vol. 45, pp. 2823-2827, Nov. 2001.

[19] H.R. Upadhye and S. G. Kandlikar, "Optimization of Microchannel Geometry for Direct Chip Cooling using Single Phase Heat Transfer," in *2nd ASME International Conference on Microchannels and Minichannels*, Rochester, NY, 2004.

[20] Y. Hadad, "Numerical Modeling and Optimization of V-groove Warm Water Cold-plate," in *33rd IEEE SEMI-THERM Symp.,* 2017, pp. 314-319.

[21] M. Sahini, "Rack-level study of Hybrid Cooled Servers using Warm Water Cooling for Distributed vs. Centralized Pumping Systems," in *33rd IEEE SEMI-THERM Symp.,* 2017, pp. 155-162.

[22] Ohmite, "W Series Heatsinks for TO-220, TO-247, and TO-246 devices," WA-T247-101E.

[23] A. Bilitsky, "The Effect of Geometry on Heat Transfer by Free Convection from a Fin Array," MS Thesis, Dept. of Mech. Eng., Ben-Gurion University, Negev, Beer Sheva, Israel, 1986.

[24] D.W. Van de Pol and J.K. Tierney, "Free Convection Nusselt Number for Vertical U-Shpaed Channels," *J. Heat Trans.*, vol. 95, pp.439-444, 1973.

[25] J.M. Lasance, (2013). *Thermal Facts & Fairy Tales: How Useful Are Heat Sink Correlations for Design Purposes?* [Online]. Available: https://www.electronics-cooling.com/2013/12/heat-sink-correlations-design/

Chapter 3: Waste Heat Recovery using Thermoelectric Generation

Due to their high heat dissipation, the recovery of waste heat from microelectronic devices is gaining significant interest. Much of the research in thermal management of modern electronic devices is focused on heat dissipation as opposed to heat recovery. Typical heat recovery units are used to recovery energy from flue gasses in engines or steam in cooling towers [1]. In the case of recovering heat from exhaust gasses, the hot side temperature is kept as hot as possible to get high heat recovery. This is a stark contrast to electronic thermal management, where the hot side temperature must be tightly controlled and kept low enough to ensure electronic stability and reliability. This presents a significant challenge for thermal engineers trying to recover heat from electronic devices. Heat sources with a hot side temperatures near 100°C are typically considered low quality heat sources. Low quality heat sources are plagued by low-efficiencies power generation and the output power is often limited in use.

As with any heat engine, the efficiency is dependent on the achievable temperature differences. The maximum efficiency for a given temperature difference is often described by the infamous Carnot efficiency. The Carnot efficiency is defined as [2]:

$$\eta = 1 - \frac{T_c}{T_h} \tag{3.1}$$

where T_c and T_h are the cold and hot side temperatures respectively. A typical maximum junction temperature for power MOSFETs is approximately 150°C. Therefore, the hot side temperature for a heat recovery system would not be able to exceed 150°C. Assuming that a cold side temperature is near room temperature conditions, 20°C, a Carnot efficiency of 31% could be achieved. This is the maximum efficiency that a heat recovery system could achieve with the power MOSFET as the heat source. Unfortunately, the true system will only be able to achieve a fraction of this 31% efficiency.

Curzon and Ahlborn [3] as well as Miranda [4] considered a Carnot cycle with heat losses. They showed that the maximum efficiency of an ideal heat engine actually approaches the following relationship with respect to the achievable temperature differences:

$$\eta_{CA} = 1 - \sqrt{\frac{T_c}{T_h}} \tag{3.2}$$

Using this definition of the maximum achievable efficiency, the case of the power MOSFET heat source in ambient conditions now has a maximum achievable efficiency of 17%, which is significantly reduced from the Carnot efficiency. Rebhan [5] derived an efficiency of a Carnot cycle that takes into account losses due to friction as:

$$\eta_R = \frac{1}{2}\left(1 - \frac{T_c}{T_h}\right) \tag{3.3}$$

For solid-state heat engines, such as thermoelectric generators, where there are no moving parts, losses due to friction are not a concern. The relationship derived by Rebhan is considered a lower limit of efficiency. For the case of a MOSFET with a hot side temperature of 150°C and an ambient temperature of 20°C, the efficiency, as derived by Rebhan, gives 15%. Therefore, for the MOSFET in ambient conditions of 20°C, the actual efficiency will be between 17% and 15%.

There are many types of heat engines that could be used for heat recovery. Unlike other heat engines, the efficiency of a TEG does not degrade at low power levels [6]. This is an important aspect for low quality heat sources, such as electronic devices, where the expected output power is low.

The following chapter will focus on the fundamentals of TEGs in the realm of waste heat recovery of electronic devices. The chapter will introduce fundamental background knowledge of the thermoelectric effects as well as current module design. Commercial TEG modeling based on finite element analysis will be used to describe the power output as well as factors affecting the output power. Modeling the TEG will give a greater understanding of the steps needed to increase the effectiveness of conversion of electronic waste heat into electrical power to ultimately improve the efficiency of the electronic device. A TEG implementation design for the specific case of a power

converter will be considered. The limitations of this design will be discussed and areas for future progress in implementing TEGs to an electronic system will be considered.

3.1 The Thermoelectric Effect:

There are three main concepts within the realm of thermoelectric phenomena. The three concepts are the Seebeck, Peltier, and Thomson effect, each named after the scientists to first encounter these principles. The Seebeck effect refers to the conversion of heat into electrical energy between the junction of two dissimilar wires. The temperature gradient creates an electric current which induces an electric field around the wire. The current density can be described by a modified Ohm's law as [7]:

$$\boldsymbol{J} = \sigma(-\boldsymbol{\nabla} V + \boldsymbol{E_{emf}}) \tag{3.4}$$

where $\boldsymbol{E_{emf}}$ is an additional term that describes the electromotive field created by the Seebeck Effect. The term σ is the local electrical conductivity and V is the local voltage. The electromotive field created by the Seebeck effect is described by:

$$\boldsymbol{E}_{emf} = -S\boldsymbol{\nabla} T \tag{3.5}$$

where S is the Seebeck coefficient, and $\boldsymbol{\nabla} T$ is the temperature gradient. The Seebeck coefficient is described as the instantaneous rate of change of the electric potential generated within an isolated conducting material subjected to a temperature gradient with respect to temperature at a given temperature. Mathematically the Seebeck coefficient is defined as:

$$S = \frac{dV_s}{dT}_T \tag{3.6}$$

where V_s is the generated electric potential [7]. The Seebeck coefficient is a material property and has a slight dependence on temperature. The relative Seebeck coefficient is described as: $S_{ab} = S_a - S_b$, where the subscript a and b refer to metal a and metal b. The most common thermoelectric materials in commercial use are lead telluride and bismuth telluride. Bismuth telluride is most commonly used for room temperature applications [8].

For steady state conditions, when the current density approaches zero, the Seebeck effect can be described as:

$$-\boldsymbol{\nabla} V = S\boldsymbol{\nabla} T \tag{3.7}$$

At zero current density, or steady state conditions, the voltage is defined as the open circuit voltage. The relationship given in Equation 3.7 can be used to determine the open circuit voltage for a given temperature difference, and can be compared to the definition described in Equation 3.6.

The Peltier effect refers to the absorption or generation of heat at conducting junctions depending on the direction of the current flow [9]. The heat generated per unit area per unit time, $\dot{Q}$, at a junction of conductor A and conductor B is related to the electric current, I, from conductor A to conductor B by:

$$\dot{Q} = (\Pi_A - \Pi_B)I \tag{3.8}$$

where Π_A and Π_B are the Peltier coefficients of conductor A and B respectively [10]. The Peltier coefficient corresponds to the amount of heat carried per unit charge. The relative Peltier coefficient is described as $\Pi_{AB} = \Pi_A - \Pi_B$. The Peltier effect is considered to be the back-action counterpart to the Seebeck effect, and the relationship between the Seebeck coefficient and the relative Peltier coefficient is simply, $\Pi = TS$, where T is the temperature.

The Thomson effect is what relates the heating or cooling of a single homogeneous conductor when a current passes along it in the presence of a temperature gradient. The predicted heat production rate per unit volume, $\dot{q}$, is given as:

$$\dot{q} = -\beta \boldsymbol{J} \cdot \boldsymbol{\nabla} T \tag{3.9}$$

where β is the Thomson coefficient, described as, $\beta = T\frac{dS}{dT}$. The Thomson effect is linear with respect to the current density, $\boldsymbol{J}$, and can be positive or negative, indicating reversible heating or cooling [10].

The overall governing thermoelectric effects, upon combining Joule heating and ordinary heat conduction can be described by Equation 3.10. The Peltier and Thomson effects can be described in terms of energy flow. For the steady state condition when energy accumulation and current gradient are zero, the governing equation becomes [11]:

$$-\dot{q}_{ext} = \boldsymbol{\nabla} \cdot (\lambda \boldsymbol{\nabla} T) + \boldsymbol{J} \cdot (\sigma^{-1} \boldsymbol{J}) - T \boldsymbol{J} \cdot \boldsymbol{\nabla} S \tag{3.10}$$

Here, $\dot{q}_{ext}$ is any additional heat added to the system from an external source, and λ is the thermal conductivity of the material. The first term of Equation 3.10 refers to Fourier's heat conduction law, the middle term corresponds to Joule heating, and the last term includes the Peltier and Thomson effects. The Seebeck effect is taken into account with the substitution of Equation 3.4 into Equation 3.10 for $\boldsymbol{J}$, the current density. Without a current, there are no Peltier and Thomson effects, and the current is developed based on the Seebeck effect. Therefore, the Seebeck effect can be thought of as the driving force for the Peltier and Thomson effects [7].

3.2 Thermoelectric Generation:

It wasn't until 1885, that Rayleigh proposed using thermoelectric phenomena to produce energy. Although his method was slightly incorrect and not currently used today, Rayleigh was the first to attempt to calculate the efficiency of a thermoelectric generator [9]. In 1909 and 1911 Altenkirch produced a satisfactory model for thermoelectric generators and refrigerators that showed that materials with large Seebeck coefficients, low thermal conductivities, and low electrical resistances could be used effectively to generate electricity. He developed an effectiveness parameter known as the figure-of-merit, Z, which is described as [9]:

$$Z = S^2 \sigma / \lambda \tag{3.11}$$

This term can be made dimensionless by the multiplication of absolute temperature. The term ZT is useful in comparing materials in certain temperature ranges, and along with the Carnot efficiency determines the energy conversion efficiency of the device.

Electrical conductivity and thermal conductivity of a material are intimately related properties, most notably through the Wiedemann-Franz Ratio or the Lorenz number based on the kinetic theory of gases [12]. Thermal conductivity of a material describes both the heat transfer by phonons as well as the heat transfer by electrons. The Weidemann-Franz law describes thermal conductivity due to electron heat transfer as $\lambda_e = L\sigma T$, where L is the Lorenz factor. The Lorenz factor for thermoelectric materials can be estimated based on the Seebeck coefficient in V/K through [13]:

$$L = 1.5 + Exp\left[-\frac{|S|}{116}\right] \tag{3.12}$$

Because the electrical conductivity and thermal conductivity are closely related material properties, their ratio is difficult for materials engineers to increase.

There has been some success in developing materials with low thermal conductivities and relatively high electrical conductivities based on the phonon-glass, electron-crystal (PGEC) concept [14]. This concept asserts that crystal structured semiconductors can allow for efficient transport of electric charge, while also inhibiting the flow of heat by their lattice structure, similar to a glass [14]. Materials with PGEC like behavior have been observed to have thermal conductivities that approach the theoretical minimum for materials with given compositions, while still maintaining good electrical properties. This increases the ratio of electrical conductivity to thermal conductivity and ultimately increases the value of ZT. A remarkably high ZT value of 2.6 ± 0.3 at 923K was recently reported by Zhao et. al. in SnSe crystals [15]. The reported dimensionless figure of merit was achieved primarily by obtaining an extremely low thermal conductivity. Practical applications require a figure of merit close to one or larger [16]. A ZT value of about 4 is needed to be competitive with convectional compressor-based technologies [6]. However, some applications do not require such high ZT values to be practical over compressor-based technologies [17]. Unfortunately, the record high ZT values are usually achieved in narrow temperature ranges. Therefore, it is important to look beyond simply the achieved ZT value and look at the temperature ranges where these ZT values are obtained.

A typical thermoelectric module consists of multiple p-type and n-type semiconductors combined in series with metal junctions, often copper. A p-type leg is a positively doped semiconductor material with a corresponding positive Seebeck coefficient. An n-type leg is a negatively doped semiconductor material, with a negative Seebeck coefficient. Often the p-type and n-type materials have nearly the same Seebeck coefficient value, with opposite signs. As was discussed earlier, using dissimilar metals with opposite signed Seebeck coefficients maximizes the possible relative Seebeck coefficient for that material. The thermoelectric couples are then insulated

electrically with a ceramic such as alumina. A typical TEG module of two legs can be seen in Figure 3.1.

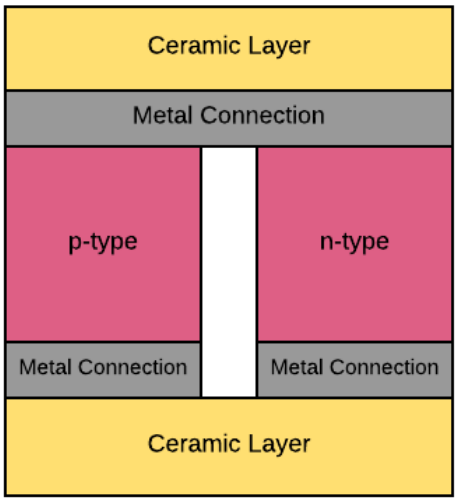

Figure 3.1 – Diagram of a typical TEG module. The ground would be defined at the bottom metal connection of the n-type leg. Current flows from the n-type to the p-type conductor through the metal connection at the top of the leg.

3.3 Modeling a Commercial TEG Module:

Modeling a TEG can be difficult, as it requires the coupling of heat transfer physics as well as electric current physics. There have been several recent studies that have been able to successfully model TEGs using finite element analysis programs [18, 19]. With the use of COMSOL Multiphysics® [20], one can model both the heat transfer and electric currents with the multiphysics coupling of the thermoelectric effect module. Simulating a TEG allows for one to test a wide variety of optimization parameters and operating conditions, without having to physically build or test a TEG. Simulations can speed up the design process, and allow for more designs to be considered.

3.3.1 Modeling with COMSOL Multiphysics®:

The thermoelectric module in COMSOL Multiphysics® includes physic interfaces related to electric currents, heat transfer in solids, thermoelectric effects, electromagnetic power dissipation, and electromagnetic material properties.

The electric currents interface allows for the determination of values such as electric field, current and potential distributions. It calculates these values for a

conducting media under no inductive effects, which is suitable for modeling TEGs. The electric currents module solves an Ohm's law based conservation of current equation using scalar electric potential as a dependent variable [21].

The heat transfer in the solids interface uses the theory of conduction, convection, and radiation to solve for the temperature profile. The temperature in solid domains is solved using a differential form of Fourier's law that allows for the addition of such things as heat sources [21].

The heat transfer and electric currents interfaces can be coupled with the thermoelectric and electromagnetic interfaces. The thermoelectric effect interface redefines the heat flux and electric current to account for the Peltier effect, Thomson effect and Seebeck effect. The thermoelectric effect interface applies a heat source based on the Peltier effect in domains and boundaries where electrical and thermal models are defined. It adds a heat flux, P**J**, to the heat equation. For solids, with the additional Peltier heating effects, the heat equation becomes:

$$\rho C_p \frac{\partial T}{\partial t} + \nabla \cdot (-\lambda \nabla T + \Pi \boldsymbol{J}) = Q \tag{3.13}$$

Recall that Π is the Peltier coefficient, λ is the thermal conductivity, ρ is the density, C_p is the heat capacity, and $\boldsymbol{J}$ is the current density [21]. The current density accounts for the Seebeck effect with the addition of the Seebeck current contribution. The current density is redefined to include the Seebeck current contribution as [21]:

$$\boldsymbol{J} = -\sigma\,(\nabla V + S\nabla \mathrm{T}) \tag{3.14}$$

The thermoelectric module primarily uses the Seebeck coefficient and, as an intermediate value, the Peltier coefficient to solve thermoelectric problems. COMSOL Multiphysics® does not use the Thomson coefficient.

The electromagnetic interface incorporates the effects of Joule heating. The electromagnetic heat source represents the source term Q_e in the corresponding heat equation:

$$\rho C_p \frac{\partial T}{\partial t} - \nabla \cdot (\lambda \nabla T + \Pi \boldsymbol{J}) = Q_e \tag{3.15}$$

where $Q_e = \boldsymbol{J} \cdot \boldsymbol{E}$ where **J** is the current density, defined by Equation 3.14 [21]. The electromagnetic heat source can also be used for boundaries to model electromagnetic surface losses as a heat source in the heat transfer part of the model. Another separate interface tool that is used is temperature coupling. The temperature coupling tool defines a source and a destination heat transfer interface and uses the temperature from the source interface to evaluate the material properties to the destination interface [21].

Through the heat transfer and electric current modules along with the coupling multiphysics modules, one can relatively easily simulate the complex system of a thermoelectric generator using finite element analysis.

3.3.2 Developing Parameters from Datasheet:

TEGs were purchased before the start of the project and were used for test purposes for the senior design team in the 2015-16 school year. The thermoelectric generators that were purchased for the project were model number: TEG1-1263-4.3; COMSOL simulations presented in this work are based off of these TEGs. These particular TEGs have 126 couples of n-type and p-type legs connected in series. The commercial TEG data sheet provides several pieces of information that are needed to correctly model the TEG using finite element analysis. The necessary values provided by the datasheet are shown in Table 3.1.

Table 3.1 - Data Sheet Values for TEG Module TEG1-1263-4.3 [22]

Hot Side Temperature (°C)	300
Cold Side Temperature (°C)	30
Open Circuit Voltage (V)	10.7
Matched Load Resistance (Ω)	5.4
Matched Load Output Voltage (V)	5.3
Matched Load Output Current (A)	1.0
Matched Load Output Power (W)	5.2

Because the datasheet does not specify a thermoelectric material or thermoelectric material properties, one must make a few assumptions with regards to the material properties. Because the Seebeck coefficient is defined as the open circuit

voltage divided by the temperature difference, one can determine an approximation of the Seebeck coefficient based on the hot and cold side temperatures and the open circuit voltage given in the datasheet. Dividing this estimation by the number of legs will give an approximation of the Seebeck coefficient of the material. The value calculated is:

$$S = \frac{10.7V}{(300°C - 30°C)} \times \frac{1}{126\ couples} \times \frac{1\ couple}{2\ legs} = \mathbf{1.57 \times 10^{-4}\ \frac{V}{°C}}$$

The value obtained for the Seebeck coefficient corresponds within the same order of magnitude as the Seebeck coefficient of bismuth telluride at a temperature of 300K given in the COMSOL Multiphysics® material library $\left(2.1 \times 10^{-4}\ {}^{V}/_{\circ C}\right)$ [20]. The n-doped material was assumed to have a Seebeck coefficient of $-S$, whereas the p-doped material was assumed to have a Seebeck coefficient of S. While the p and n-doped materials do have varying values of Seebeck coefficients beyond the sign inversion, the variations are not significant or large in magnitude and should not significantly affect the solution. The Seebeck coefficient is also assumed, in this case, to be independent of temperature. In reality, the Seebeck coefficient has a slight dependence on temperature. Because the variation with temperature is only slight, and the Seebeck coefficient was estimated from the data sheet values, the constant Seebeck coefficient assumption should not have a significant impact on the solution. The rest of the material properties for the thermoelectric material were obtained from bismuth telluride in the COMSOL Multiphysics® material library [20].

The dimensions of the thermoelectric legs and module components can have a significant impact on the solution. Because the dimensions of the particular module were not given in the datasheet, the TEG was broken open and the dimensions were measured with micrometers under a microscope. Microscope images can be seen in Figure 3.2 through Figure 3.4.

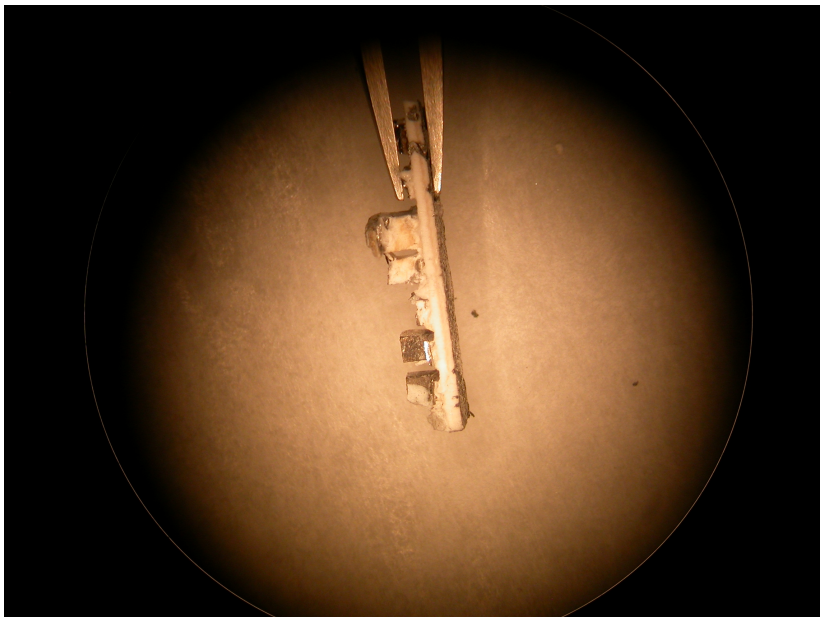

Figure 3.2 - Side view of inside of the TEG module under a microscope.

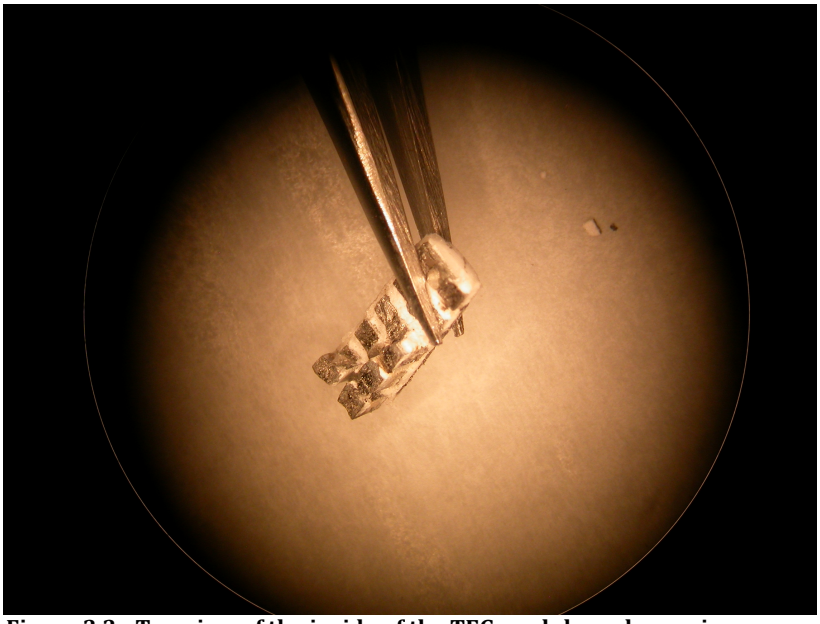

Figure 3.3 - Top view of the inside of the TEG module under a microscope.

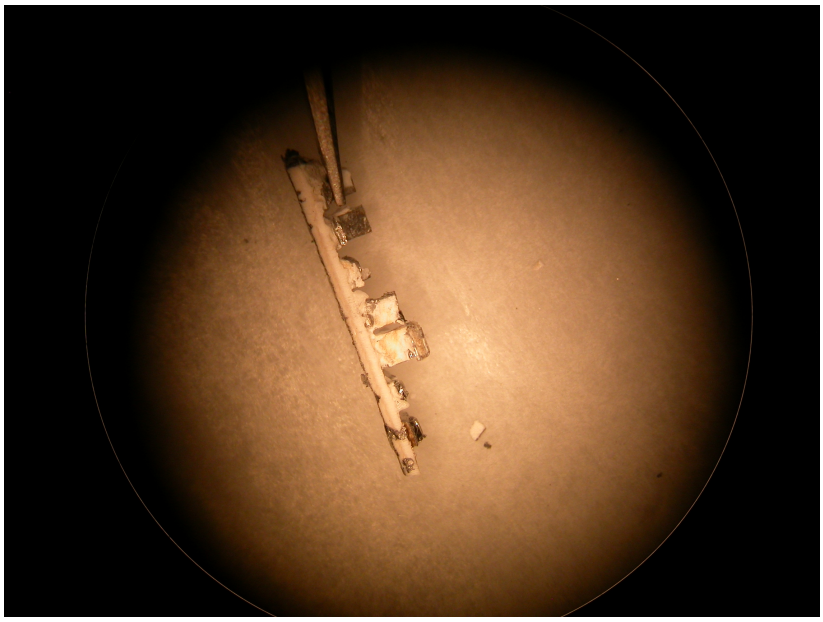

Figure 3.4 - Alternative side view of inside of the broken TEG module under a microscope.

A summary of the measured dimensions can be seen in Table 3.2. The values were averaged from the few legs that were still in tact after the TEG module was broken open. Because bismuth telluride is a not a hard or tough material, only a few of the legs could actually be measured. A common set up for a TEG device is to have the thermoelectric legs connected electrically by copper and then insulated with a ceramic layer such as alumina. Some of the layers could be seen in the broken TEG, and rough estimates of the leg, metal connection, and insulation layer are given in Table 3.2. These estimations were used to develop the geometry of the COMSOL® model.

Table 3.2 - Measured Dimensions of TEG Module

TEG Leg Height (mm)	1.26
TEG Leg Width (mm)	1.00
TEG Leg Depth (mm)	1.00
Copper Thickness (mm)	0.24
Insulated Alumina Layer (mm)	0.76

In addition to the values provided in Table 3.1, the datasheet also provides plots of the output voltage and output power as a function of output current. These plots can be reproduced using simulation in order to check the validity of the simulated model.

3.3.3 Modeling Open Circuit Voltage and Power Output:

A simple 2D TEG model is used to validate additive voltages between couples in series. Figure 3.5 and Figure 3.6 show the temperature and electric potential profiles of a one couple, two couple, and three couple TEG modeled from COMSOL® Multiphysics. The hot and cold side temperatures defined at the top and bottom most boundaries with all other boundaries thermally insulated. The temperature profiles in Figure 3.5 shows the thermally parallel legs. The ground is defined at the right most leg as observed is Figure 3.6. From Figure 3.6, it can be seen that the voltages from the one to the two to the three couple models are additive, where the one couple model has an open circuit voltage of 0.073V, the two couple model 0.146V, and the three couple model 0.219V. Modeling 126 TEG couples would be taxing and cost a significant amount of computational time. Because the voltage is additive with the number of couples, a single couple model should be able to give $1/126^{th}$ of the open circuit voltage in the entire 126 couple TEG module.

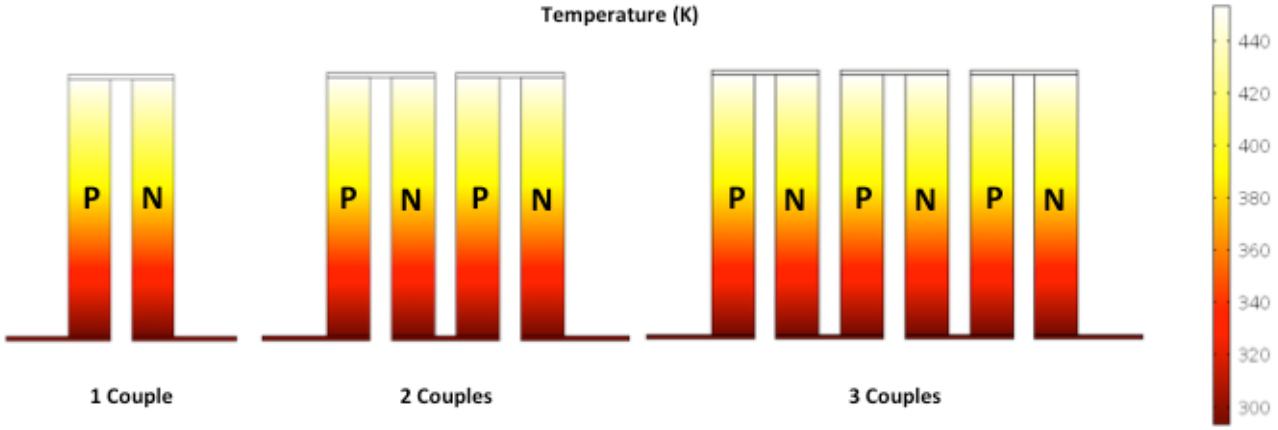

Figure 3.5 - Temperature profile of 2D TEG simulation of a 1 couple, 2 couple, and 3 couple model

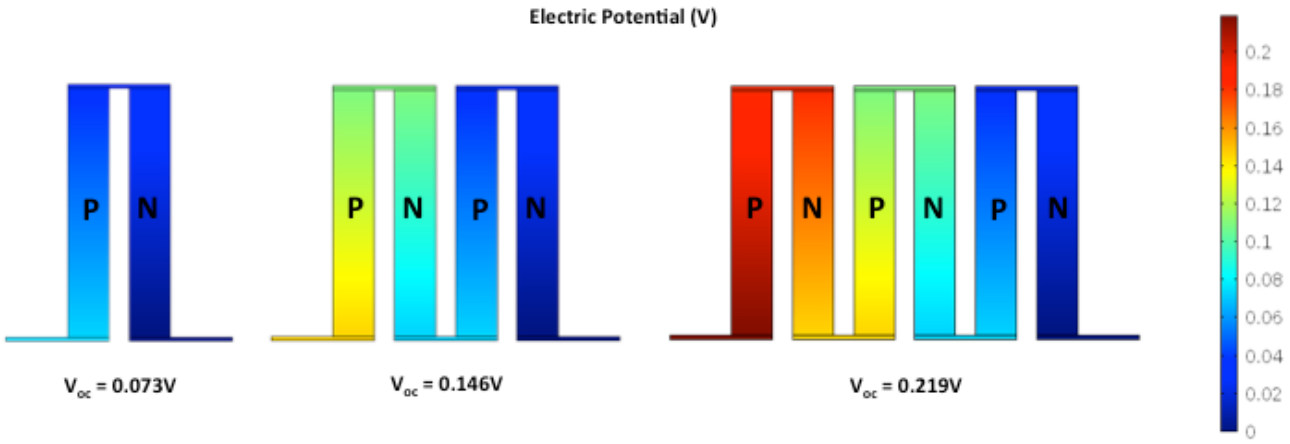

Figure 3.6 - Electric potential profile of 2D TEG simulation of a 1 couple, 2 couple, and 3 couple model

The previously described two-dimensional models are only able to show the open circuit voltage. In order to produce power, a load resistance must link the TEG terminal connections. A resistance load can be applied to the TEG by placing an extra block in the geometry between the first and the last couples' copper connection. The resistor block has no material properties except electrical conductivity, and is not included in the heat transfer analysis. The electrical conductivity can be converted to an electrical resistance based on the dimensions of the block. In order to be able to calculate the current through the block, a three-dimensional model is needed.

A single couple, four couple, twelve couple, and twenty couple models are studied to ensure that the number of couples does not have an effect on the solution. Figure 3.7 and Figure 3.8 show the one couple and four couple geometry respectively. Note that the block has a line in the center, splitting it into two domains. The current density was taken as a surface average quantity on the resistor block's center surface, or the surface that splits the block in half. In order to have the load resistance applied to the end connections, the block must be placed between the first and last couple. The single couple model simply has the resistor block placed between the n and p-type leg, which is shown in Figure 3.7. For models with more than one couple, the couples must be arranged in two lines of equal couple length, where one end is electrically connected and the other end is connected by the resistor block. This can be seen in the four couple model shown in Figure 3.8.

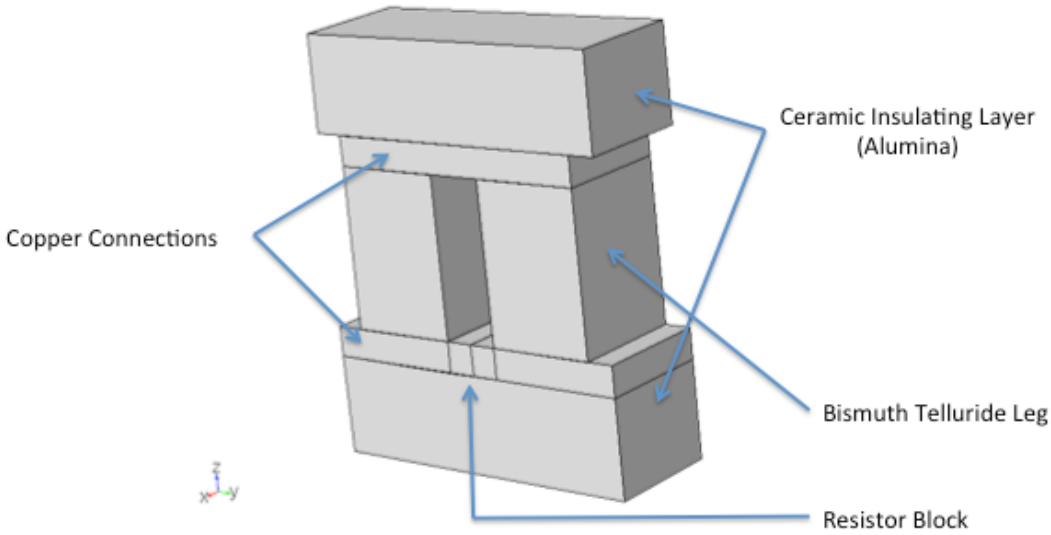

Figure 3.7 - COMSOL® geometry for the single couple TEG model.

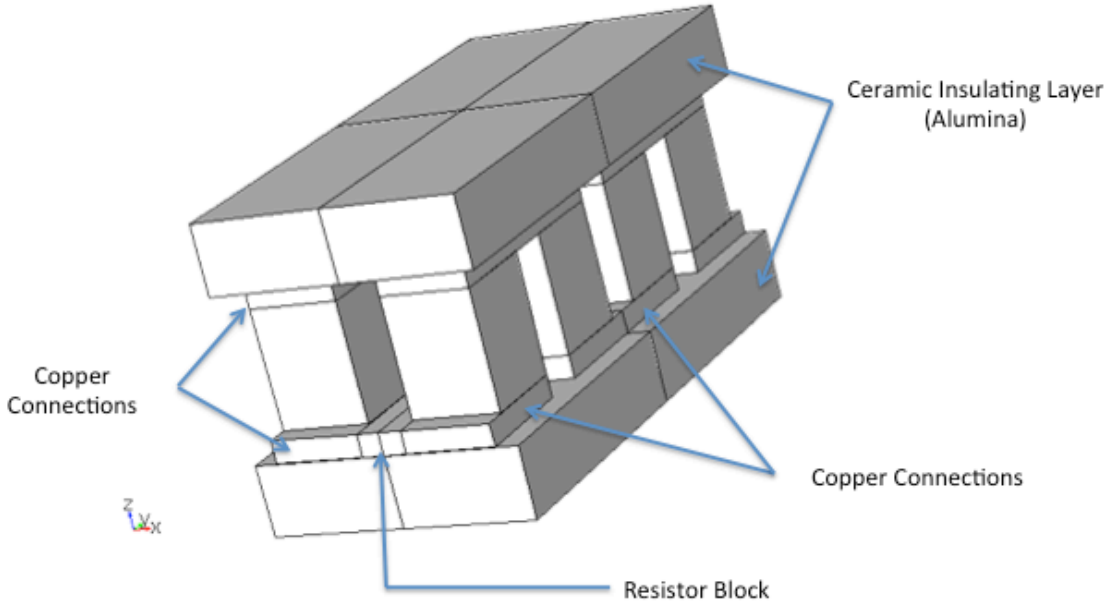

Figure 3.8 - COMSOL® geometry of the four couple TEG model.

With the electrical conductivity of the resistor block defined as a parameter in COMSOL®, a parametric sweep of the electrical conductivity can represent a varying load resistance on the TEG. The temperature and electric potential profiles of the four couple model are shown in Figure 3.9 and Figure 3.10 respectively for a load resistance of 166Ω. This load resistance corresponds to an electrical conductivity of 10S/m, which was the first point in the parametric sweep. The locations of the resistor block as well as temperature and electrical boundary conditions are presented in Figure 3.9 and Figure

3.10. All undefined boundaries are defined as thermally and electrically insulated. The geometry is based on the measured dimensions of the commercial TEG module presented in Table 3.2. The hot and the cold side temperatures are based on the datasheet values, reproduced in Table 3.1.

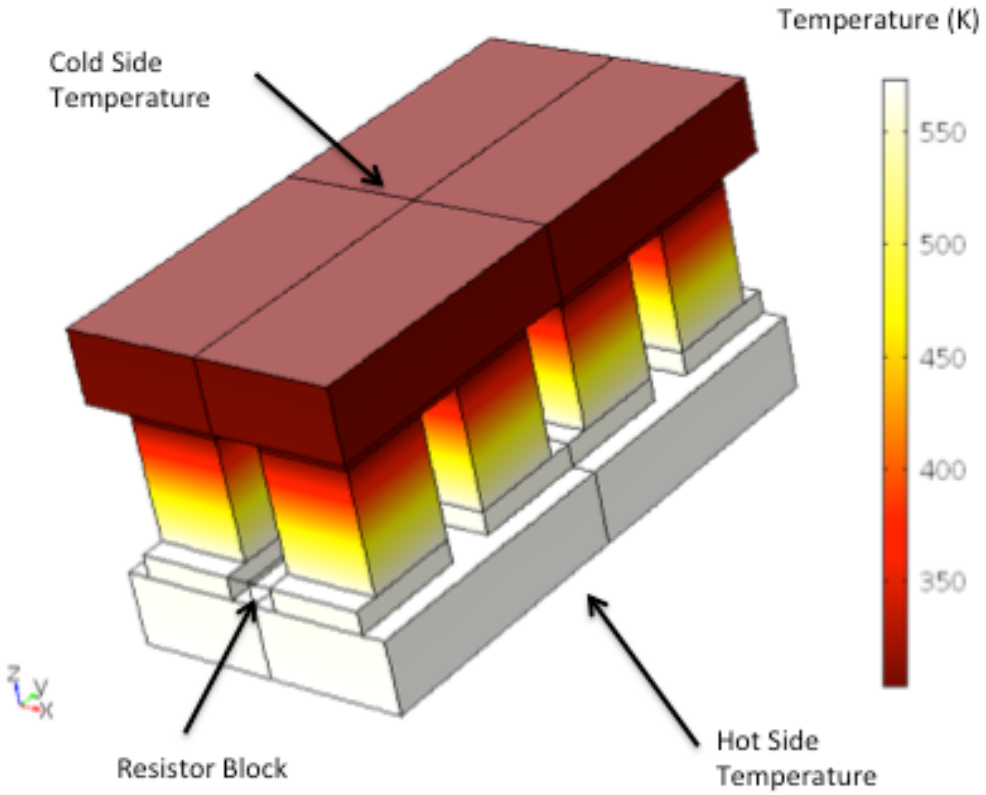

Figure 3.9 - Temperature profile of the four couple TEG modeled in COMSOL multiphysics

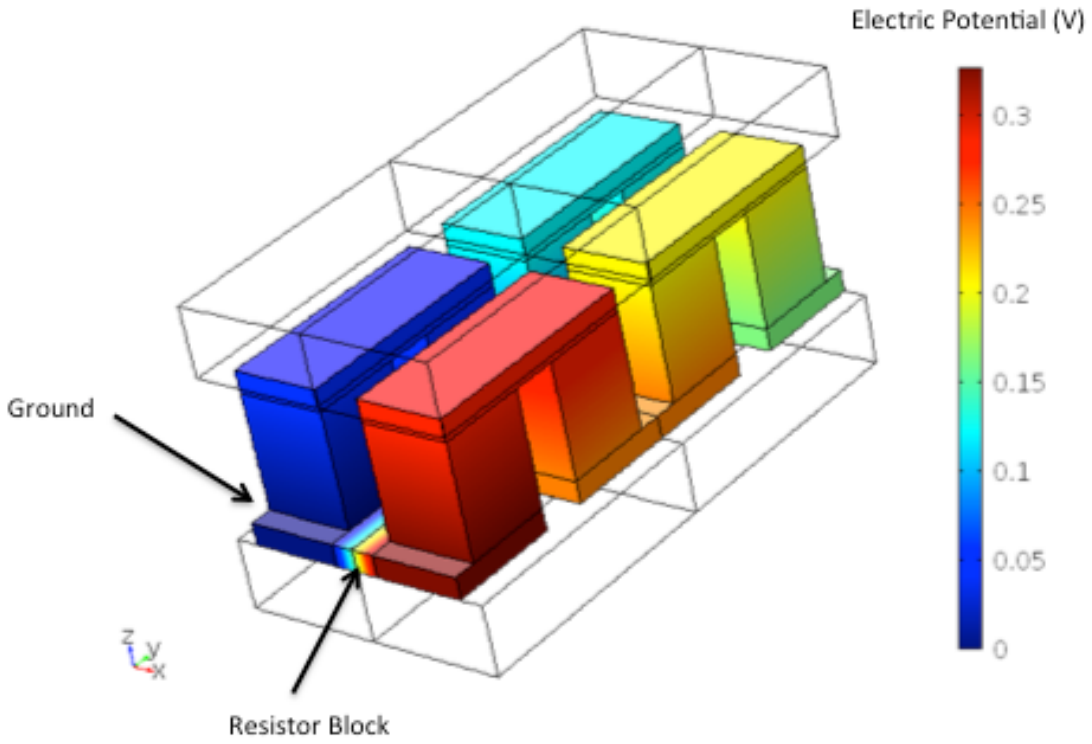

Figure 3.10 - Electric potential profile of four couple TEG modeled in COMSOL Multiphysics.

The one, four, twelve, and twenty couple model are compared with the datasheet values for the full 126 couple module by scaling the output voltage in the models to the full 126 couple TEG. The electric potential is scaled by taking the maximum electric potential calculated in COMSOL® and multiplying it by 126 and dividing by the number of couples in the COMSOL® model. The power output is determined by multiplying the scaled electric potential and the current based on the current density calculated in COMSOL®. The power output curves as a function of current obtained from the scaled COMSOL® simulations are shown in Figure 3.11 along with a reproduced plot from the TEG datasheet. One can see from Figure 3.11, that single, four, twelve and twenty couple models have a power curve that matches the power curve given in the datasheet. The 126 couple scaled open circuit voltage and matched load output power for each simulation is shown in Table 3.3.

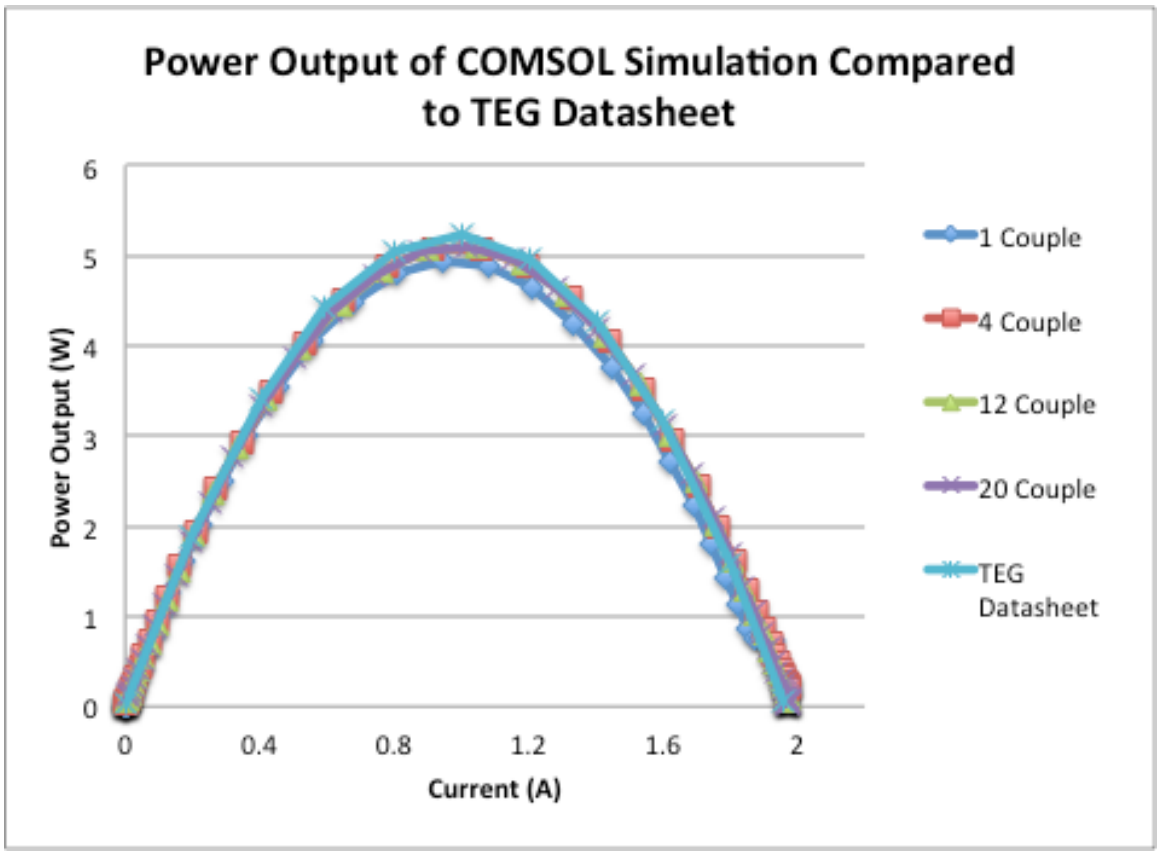

Figure 3.11 - Power output curves, from scaled COMSOL simulations as well as a reproduced graph of the TEG data sheet.

Table 3.3 – Scaled open circuit voltage and matched load output power of COMSOL simulations

Number of Couples in Simulation	Scaled Open Circuit Voltage (V)	Matched Load Output Power (W)
1	10.1	4.9
4	10.3	5.1
12	10.3	5.1
20	10.2	5.1
126 [22]	10.7	5.2

As expected, there is a linear trend in the matched load output power of the COMSOL® simulations versus the number of couples in the simulation. Figure 3.12 shows the linear trend of matched load power output as a function of the number of couples. The origin is also taken as a data point for the development of the trend line. Note that the matched load output power plotted in Figure 3.12 is not scaled to 126 couples, and therefore the individual points correspond to what one would expect for a 1 through 20 couple TEG module. Using the trend line equation to extrapolate to the full

126 couple module, a matched load output power of 5.1 W is obtained. This is slightly lower than the value provided in the TEG datasheet, restated in Table 3.1 and Table 3.3.

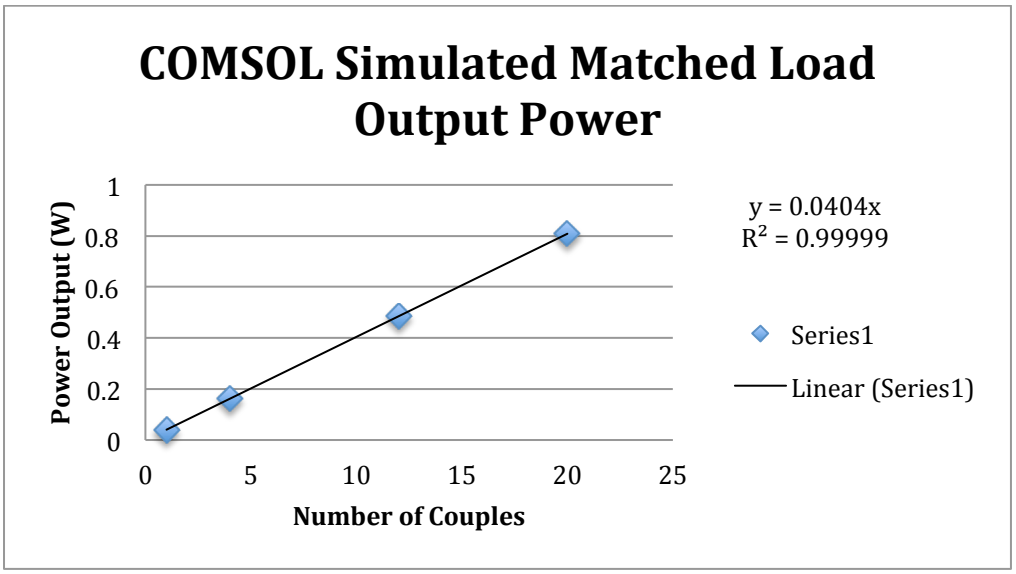

Figure 3.12 - Matched load output power as a function of the number of couples. Data produced from COMSOL simulations.

One factor that could be playing a part in causing the matched load output power to be slightly lower than the value given in the data sheet is the internal resistance of the system. The COMSOL® model does not take into account parasitic resistances, such as contact resistance. Figure 3.13 gives the matched load resistances for the COMSOL simulations of 1 through 20 couple models with a corresponding trend line. Using the trend line obtained from the simulated data shown in Figure 3.13, at 126 couples, the matched load resistance is calculated to be 4.86 Ω, which is indeed less than the listed matched load resistance of 5.4 Ω given in the TEG data sheet. Because the COMSOL® model is essentially an ideal system, it is reasonable that the matched load resistance is lower than the data sheet values. The increase in resistance in the physical TEG is likely due to contact resistances. The effects of contact resistance will be discussed further in section 3.3.5.

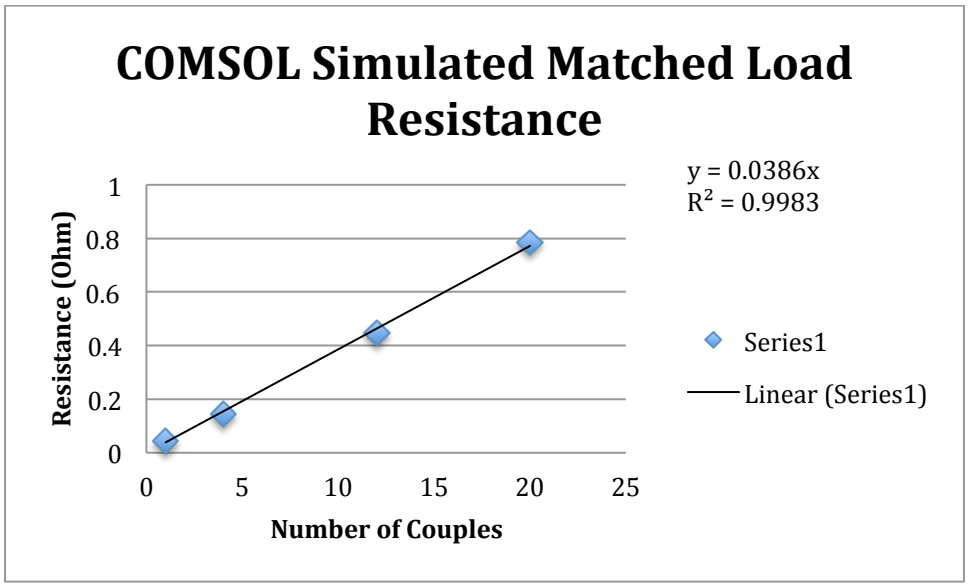

Figure 3.13 - Matched load resistance as a function of the number of couples in the model. Data is obtained from COMSOL simulation.

3.3.4 Mesh Refinement:

In order to ensure that the solution produced by the finite element method converges to a solution that approaches a true solution, a mesh refinement analysis is performed. Through the mesh refinement process it was found that the element size could be relatively coarse without having a significant effect on the solution. The four couple TEG module was solved for four different automated meshes. These meshes are preprogrammed in COMSOL® to develop mesh elements that relate to the corresponding physics in the model. The default mesh elements for the heat transfer and electric currents physics are tetrahedral. Tetrahedral elements are the easiest to use for any particular geometry and give a sufficient minimum element quality for the TEG geometry. A physics controlled normal mesh, finer mesh, extremely fine mesh, and a semiconductor controlled mesh with an extremely fine element size were compared. The finalized mesh parameters are shown Table 3.4. COMSOL® Multiphysics suggests a minimum element quality value greater than 0.1 for most applications [23]. It can be seen from Table 3.4 that the minimum element quality is achieved with a physics controlled mesh with a finer element size. Figure 3.14 shows the solution for the power curve for each of the mesh types. As one can see from Figure 3.14, the solution does not change significantly between the different mesh types.

Table 3.4 - Mesh parameters for each of the used automated COMSOL Multiphysics® [20] meshes.

	Physics Controlled Normal Mesh	Physics Controlled Finer Mesh	Physics Controlled Extremely Fine Mesh	Semiconductor Controlled Extremely Fine Mesh
Number of Elements:	5868	19120	400601	1475934
Minimum Element Quality:	0.02049	0.1778	0.1349	0.1326
Computational Time	6 min 27 s	11 min 44 s	2 h 51 min 31 s	8 h 9 min 28 s

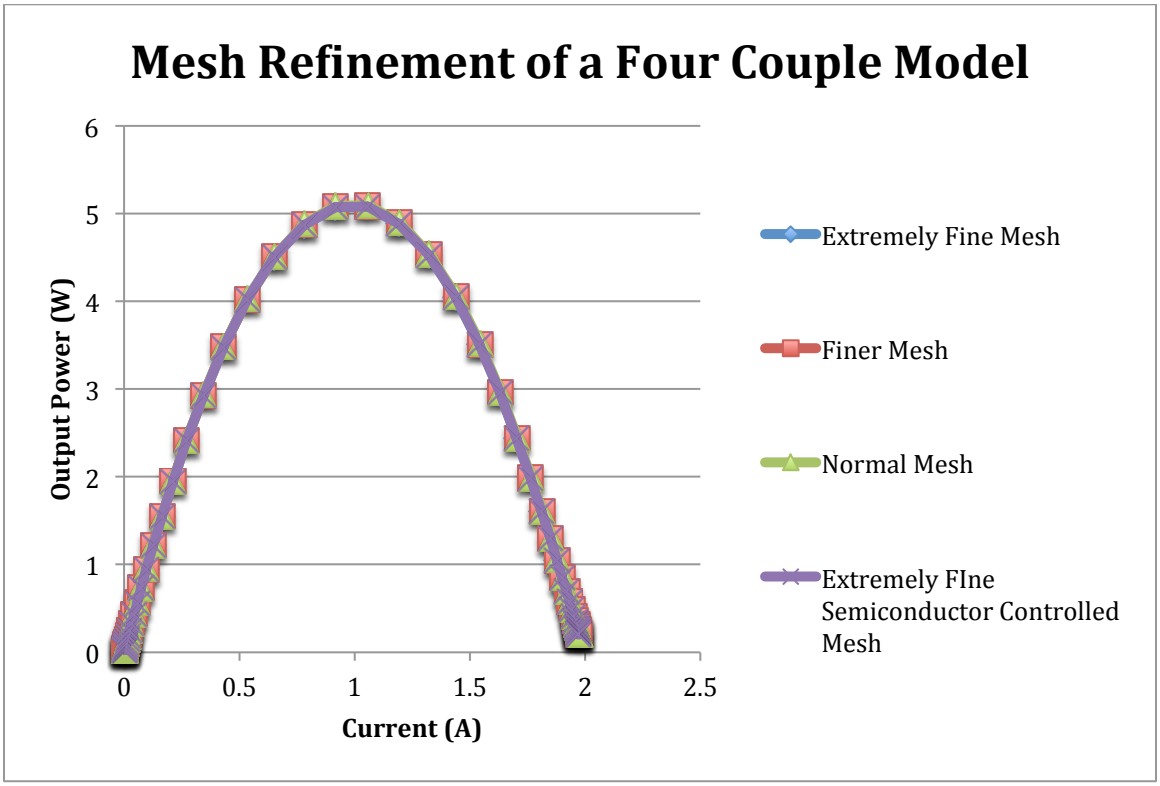

Figure 3.14 - Output power curve as a function of current for a scaled four couple TEG model. Data is from COMSOL Multiphysics® [18] simulation with varying automated meshes.

3.3.5 Factors Influencing Output Power:

There are many factors that can affect the power output of a TEG device. Optimization of these factors can enable better thermoelectric power output for the device. There are many studies that look at these factors, some of which include thermoelectric material properties [14, 24], geometry [25, 26], interfacial contact

resistance [27], and non-uniform temperature over heat spreaders [28]. The interface contact resistance between the thermoelectric material and the metal connection as well as the TEG leg height is further considered in this section.

One significant challenge with thermoelectric devices is the direct soldering of thermoelectric materials. With the use of direct soldering on thermoelectric materials, one encounters the problem of poor wettability of solder on most thermoelectric materials. This presents not only a mechanical problem, but also produces an electrical resistance problem [8]. While contact resistance between semiconductor material and metal may seem small, the significance can have a profound impact on the power output of a TEG. In a 126 couple module, there are 252 legs each with two metal contacts. This leads to a total of 504 total semiconductor-copper interfaces. With this large number of interfaces, even small contact resistances can have a significant effect on the total resistance of the device, and hence the power output. The effect of the resistance on the maximum power output can be calculated theoretically by [29]:

$$P = \frac{(2nS\Delta T)^2}{4(R)} \tag{3.16}$$

derived from $\left(P = {V^2}/{R}\right)$, where n is the number of couples, and R is the electrical resistance. The 2 in the numerator is there to account for two legs per couple. In our case $n = 126$. Assuming that resistance of the metallic electrode is small, the total resistance of the module can be described as [27]:

$$R = n\left(R_{n-TE} + R_{p-TE}\right) + 4nR_c \tag{3.17}$$

where R_{n-TE} and R_{p-TE} are the electrical resistance of the n-type and p-type couple respectively, and R_c is the electrical contact resistance. The electrical resistance of the p-type and n-type leg is calculated from the material properties in the COMSOL library for bismuth telluride. The electrical resistance of the bismuth telluride legs is calculated by:

$$R_{n-TE} \cong R_{p-TE} = \frac{l}{A_c\sigma_{TE}} \tag{3.18}$$

where l is the thermoelectric leg height, A_c is the cross-sectional area of the thermoelectric leg, and σ_{TE} is the electrical conductivity of bismuth telluride, given in the COMSOL material library as 58824 S/m at 400K (126.85°C). Based on the dimensions given in Table 3.2, $R_{n-TE} \cong R_{p-TE} = 0.02\Omega$. This thermal resistance value calculated from the material properties can be input into Equation 3.17. Setting Equation 3.17 equal to the matched load output power given in the TEG datasheet (Table 3.1), an estimate of the contact resistance can be calculated. Using this method, $R_c = 0.88\text{m}\Omega$.

Recall from the trend line extrapolation in Figure 3.13, the matched load resistance was estimated to be 4.86Ω. The COMSOL® model does not take into account contact resistance. Therefore, if one subtracts the estimated load resistance obtained with COMSOL from the load resistance given in the datasheet (Table 3.1), the difference is an estimate of the total contact resistance. This estimated resistance can then be dividing by 126 couples, and then again by 4 because there are 4 connections per couple to obtain the contact resistance per contact. Using this method the contact resistance is estimated to be 1.07mΩ.

The contact resistance estimated from the COMSOL® simulation is slightly more than that estimated from material properties. The difference is likely due to an error in the material property estimate. The electrical conductivity value greatly affects the calculated resistance of the bismuth telluride legs, which in turn greatly affects the contact resistance. The calculation of electrical resistance of the TEG legs based on material properties does not take into account the dependence of electrical conductivity on temperature. However, the values obtained from the COMSOL® simulation do take the temperature dependence into account. Therefore, the electrical resistance obtained from the matched load resistance plot extrapolation is likely the more accurate estimate of contact resistance at 1.07mΩ. Ebling et al. reports contact resistances ranging from 0.5mΩ to 30.6mΩ for different solder types [18]. The values calculated in this analysis are well within a typical contact resistance range seen in soldered thermoelectric materials.

In order to look at how the contact resistance affects the power output, a thin contact layer is added to the four couple TEG COMSOL® model at each leg-copper interface. The thin contact layer thickness is chosen as 1μm. The cross-sectional area of the thin contact layer is equivalent to the cross-sectional area of the TEG leg (1.00mm× 1.00mm). Based on these dimensions, an electrical conductivity can be calculated using Equation 3.18 to equivalently represent a given contact resistance in Ohms. Thin layer boundary properties are useful in COMSOL® Multiphysics as the thin layers are not included in the physical geometry and hence do not have to be meshed. This allows for a significant decrease in computation time and mesh simplicity. A parametric sweep of the electrical conductivity from 1 S/m to 1×10^4 S/m, corresponding to a resistance of 990mΩ to 0.099mΩ, was simulated. The results of the parametric sweep simulation are shown in Figure 3.15. Also shown in Figure 3.15 is the results calculated from theory using Equation 3.16 and Equation 3.17. The maximum power output as described in Figure 3.15 is scaled to 126 couples from a 4 couple model. As one can see from Figure 3.15, the simulation results correspond well to theory at high contact resistances.

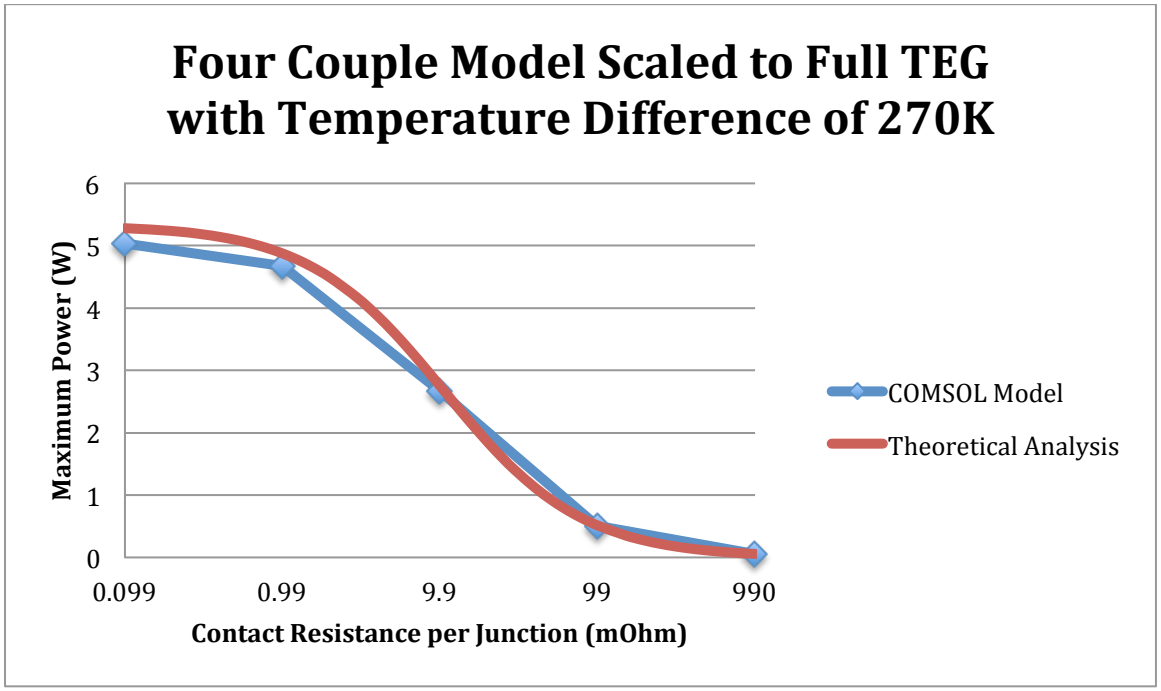

Figure 3.15 - Matched load output power as a function of the applied contact resistance per junction. Data is obtained from the four couple TEG COMSOL Multiphysics® [20] simulation and is compared to theory.

At low contact resistances, specifically at zero contact resistance, the COMSOL model and theoretical analysis differ slightly. Recall that the maximum power output of the COMSOL® simulation with a scaled four couple model is 5.1W for a 126 couple module. The zero point using the theoretical formula gives 5.33W for a 126 couple module. The discrepancy between the COMSOL® simulation and the theoretical formula at the zero point, may be due to the fact that the theoretical model does not take into account the temperature drop across the insulated ceramic layer and copper connection that is modeled in the COMSOL® simulation. The temperature difference across the legs in the COMSOL® model is less than the applied temperature difference of 270K, which is used to calculate the power output in the theoretical equation. The average temperature drop across the legs in the COMSOL® model is obtained from COMSOL® Multiphysics derived values function as 262K. Inputting this value for the temperature difference into the theoretical equation gives a zero contact resistance value of 5.03W, and a corresponding plot, Figure 3.16, of power output as a function of contact resistance. Note that Figure 3.16 shows better correspondence between theory and simulation at lower contact resistances per junction. Figure 3.16 also shows that contact resistances less than 1mΩ do not have a significant effect on the power output. The previously presented analysis of the commercial TEG, gave a contact resistance value of 1.07mΩ. Indicating that the contact resistance does not play a significant role in reducing the power output.

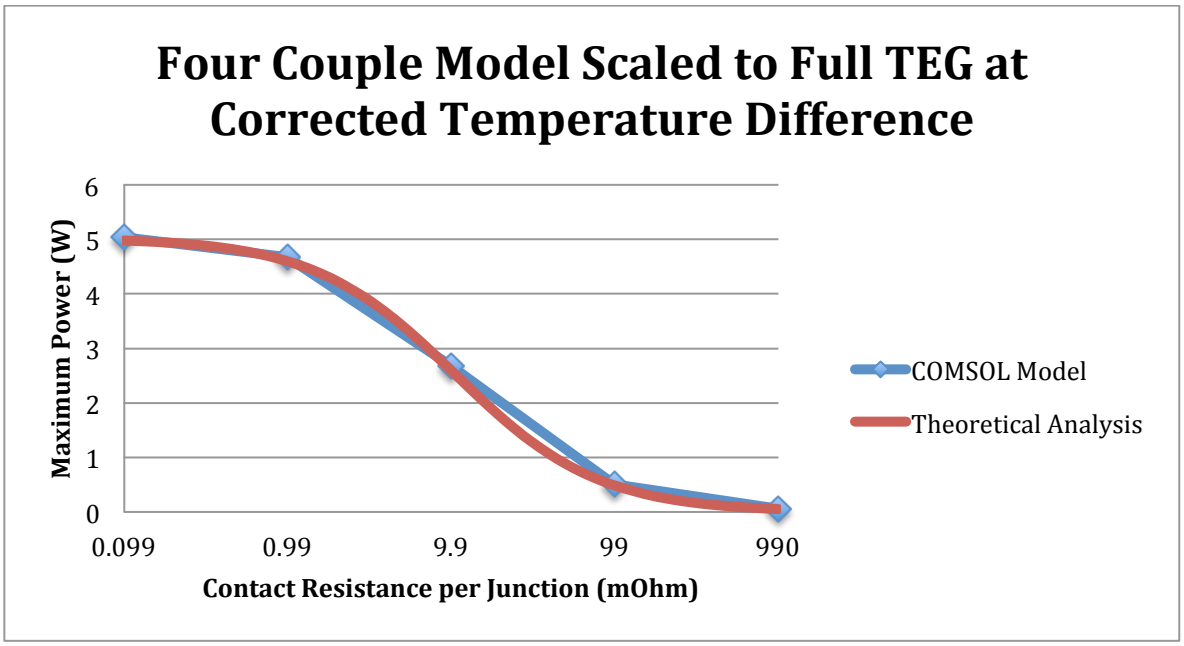

Figure 3.16 - Matched load output power as a function of applied contact resistance. Data is obtained from a four couple TEG COMSOL Multiphysics® [20] simulation and compared to theory with a temperature drop of 262.14 K.

Another property that can have a significant impact on the power output of a TEG is the thermoelectric leg height. When modeling the commercial TEG, the leg height was estimated using micrometers to get a reasonable approximation of the actual thermoelectric leg height. However, if one were to move away from using commercial TEG modules to custom built ones, the leg height would be a very important optimization parameter. Multiphysics simulation is a useful tool when comparing models with different geometry such as thermoelectric leg height. A parametric sweep simulation was performed in COMSOL® Multiphysics to see how the power output would change with thermoelectric leg height. This simulation was then compared to the theoretical power, Equation 3.16, and further compared to a more realistic power model presented by Min and Rowe [29].

In the more realistic power analysis, thermal contact resistance as well as electrical contact resistance of the contacting layers is taken into account. The contacting layers include the copper connections as well as the insulated ceramic layers. The hot and cold side temperatures are defined at the outer edge of the ceramic layers to best describe how the TEG would operate in a real system. As the thermoelectric leg height decreases, the temperature difference across the leg also

decreases. This is because more heat must be lost through the ceramic and metal connection layer when the legs are shorter in order to maintain the hot and cold side temperatures. Min and Rowe theoretically derived a comparison of the applied temperature difference across the TEG to the actual temperature across the legs [29]:

$$\Delta T = \frac{\Delta T_0}{1 + 2\left(\frac{\lambda}{\lambda_c}\right)\left(\frac{L_c}{L_0}\right)} \tag{3.19}$$

Where ΔT_0 is the applied temperature difference, λ is the thermal conductivity of thermoelectric leg, λ_c is the thermal conductivity of the contacting layer, L_c is the height of the contact layer and L_0 is the height of the thermoelectric leg. They also account for electrical resistance related to the height of the TEG. The total resistance per couple is defined as $R_{total} = R + R_{contact}$ where R is the electrical resistance described by Equation 3.17 and $R_{contact}$ is the electrical resistance due to the contacting layers, $R_{contact} = 4\frac{\rho_c}{A_0}$. With rearrangement, the electrical resistance with the inclusion of the contact layers is given by [29]:

$$R = 2\rho\left(\frac{L_0}{A_0}\right)\left(1 + \frac{n}{L_0}\right) \tag{3.20}$$

where $n = 2\,{}^{\rho_c}/_{\rho}$. Note that Equation 3.20 does not include metal to thermoelectric interface contact resistance. Plugging the temperature difference and electrical resistance calculated from Equation 3.19 and Equation 3.20 into Equation 3.16, one obtains a realistic model for output power. With rearrangement, the modified power equation becomes [29]:

$$P = \frac{P_i}{\left(1 + \frac{n}{L_0}\right)(1 + 2rw)^2} \tag{3.21}$$

where $r = \left(\frac{\lambda}{\lambda_c}\right)$ and $w = \left(\frac{L_c}{L_0}\right)$ and P_i is the power output obtained from the ideal case, Equation 3.16. Results for the COMSOL® simulation are compared to the modified ideal case with an interfacial contact resistance of 1mΩ and the realistic power equation shown above, where P_i is taken as the power obtained with an interfacial contact resistance of 1mΩ. The results are shown in Figure 3.17. The dimensions, with the

exception of leg height are the same as those given in Table 3.2. The values used for r and n are estimated from the material properties in the COMSOL Multiphysics® [20] materials library.

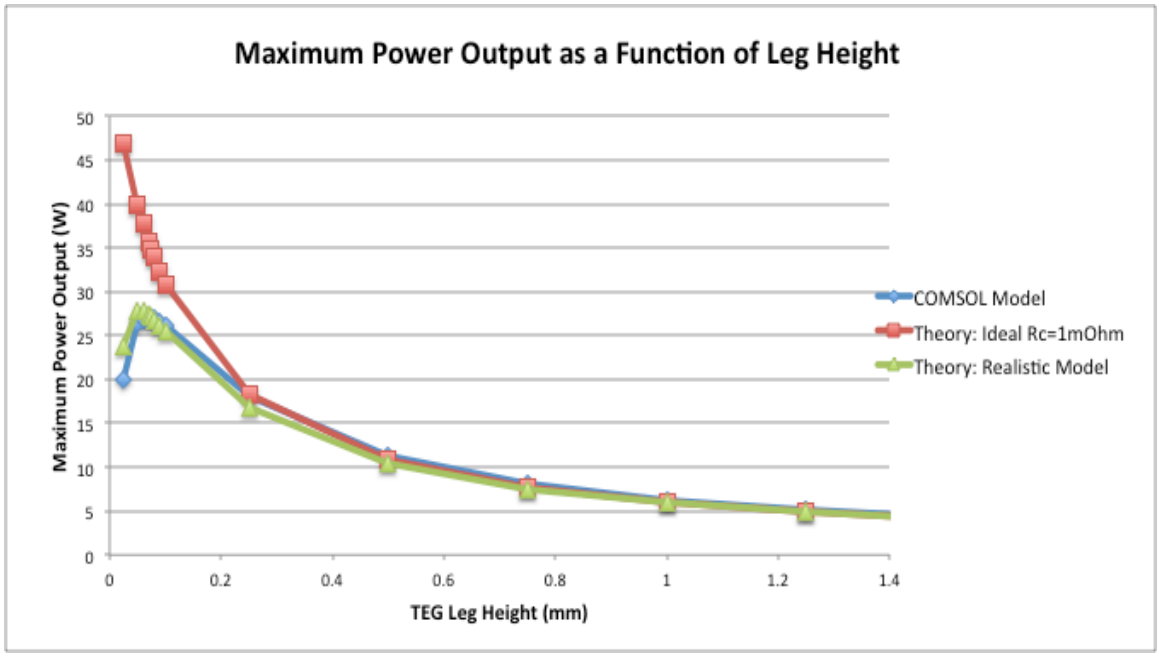

Figure 3.17 - Matched load output power as a function of thermoelectric leg height. Data obtained from COMSOL simulation are compared to two different theoretical models.

One can see from the results shown in Figure 3.17 that the ideal power equation, Equation 3.16, with an interface contact resistance of 1mΩ matches the COMSOL simulation data well at higher thermoelectric leg height values. At higher leg heights, the effect of the contacting layer becomes less significant. The realistic model captures the values at lower thermoelectric leg heights when the effect of contacting layers becomes significant. The power output reaches a peak, unlike in the modified ideal case where it increases to infinity.

When the thermoelectric leg becomes so small that the temperature difference across the leg approaches zero, the power output also approaches zero. At small leg heights, the temperature loss occurs primarily in the contacting layers and not in the thermoelectric leg itself. This change in temperature difference is accounted for in the realistic model and in the COMSOL simulation, which is why one observes a peak power output and then a significant decrease toward zero in both of these cases. For the

system presented in this analysis an optimized leg height for maximum power output occurs at a thermoelectric leg height of 0.1mm.

3.4 Integration of the TEG into the Thermal Solution:

While thermoelectric generators for energy recycling in electronic devices are an interesting prospect, the implementation requires a delicate balance between thermal resistance and gained power output. A key misconception behind waste heat recovery lies in the limitations of thermal resistance. Thermal resistance describes the thermal efficiency from one thermal interface to another. Thermal resistance is defined as the temperature difference across an interface divided by the heat flow. A one-dimensional thermal analysis of a typical electronic device can be seen in Figure 3.18A. The addition of a thermoelectric generator can be seen in the Figure 3.18B. Thermal resistance and heat flow in a thermal system are analogous to electrical resistance and current in a circuit. Also included in Figure 3.18 is the analogous schematic showing the individual thermal resistances in series.

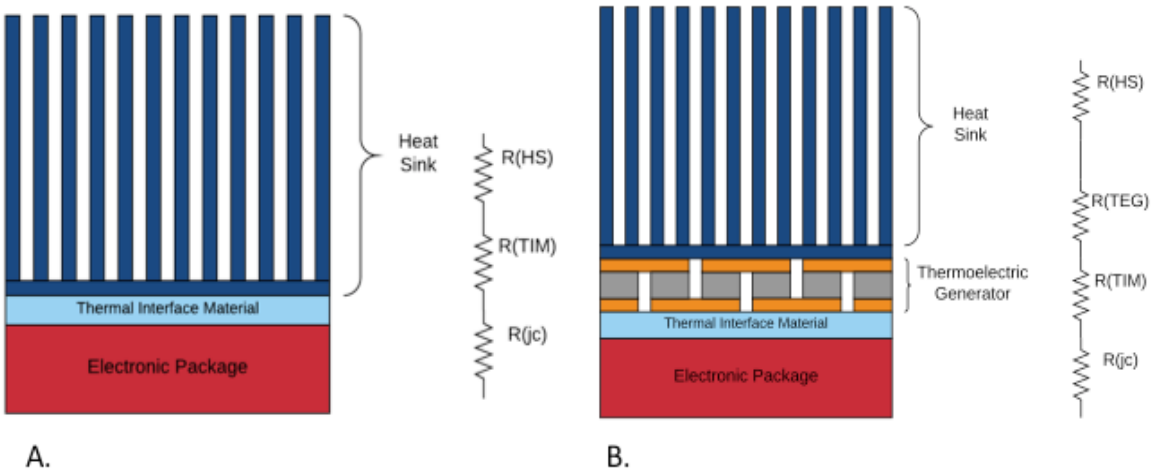

Figure 3.18 – A. Shows a typical electronic system B. Shows a typical electronic system with the addition of a TEG. The thermal resistance of each layer is in series similar to electrical resistors in series.

Thermal resistances, like electrical resistances, are additive in series. The goal of any electronic cooling system is to minimize the junction temperature. The junction temperature refers to the temperature where the electronic chip is joined to the electronic package. This will be the hottest temperature of any electronic system as this is where heat is being generated. In order to minimize the junction temperature, the

thermal resistance from the electronic junction to the ambient environment must be minimized. From the Figure 3.18, R(jc) refers to the junction to case thermal resistance or the resistance through the electronic package. R(TIM) refers to the thermal resistance of the thermal interface material, such as thermal grease or phase change materials, and R(HS) refers to the thermal resistance of the heat sink, which can be difficult to predict, but is further discussed in Chapter 2. R(TEG) refers to the thermal resistance of the TEG device.

Figure 3.18A. shows that the addition of a thermoelectric generator thermally in series with the electronic device adds an additional thermal resistance that further prevents the flow of heat from the junction to the ambient environment. This additional resistance causes the device to run at a hotter temperature for the same heat sink resistance. When a device runs at a hotter temperature, the device efficiency decreases. This is because the electrical resistance of the device is a function of the device junction temperature. Therefore, the benefit of heat recovery must be compared to the overall efficiency gain or loss that comes with an increased junction temperature.

In order to look at the increase in overall thermal resistance, a one-dimensional analysis was performed to compare the maximum junction temperature of an electronic device with the addition of a thermoelectric generator in series, similar to that shown Figure 3.18B. The electronic device that is considered is a SiC MOSFET switching device that is packaged in a TO-247 package design. The heat dissipation of the device is calculated based on the operating conditions of 20V, 20A and an estimated junction temperature of 130°C. At these operating conditions the electrical resistance is estimated to be 117mΩ. The electrical resistance is calculated based on the on-resistance versus junction temperature and drain source current plots provided by the device datasheet. More about this calculation is provided in Chapter 1. Note that the resistance value provided here is based on a 100% duty cycle. In reality, the SiC MOSFET switches will only be running at a 50% duty cycle or less. The corresponding heat flow is calculated using $P = DI^2R$, where D is the duty cycle, which gives a value of 46.8W. The junction to case thermal resistance is given as 0.6 K/W in the datasheet. The thermal resistance of the thermal interface material is chosen to be 0.4 K/W, which may be considered a slight overestimate of a typical thermal interface material. The thermal

resistance of the TEG is based off of the contact area of the TEG with the electronic device, the thermal conductivity of bismuth telluride and the height of the commercial thermoelectric legs. An average Seebeck coefficient of 0.000157 S/m and a 126 couple module was used to determine the output voltage of the TEG.

Two analyses were performed, the first was a high estimate of the thermal resistance of a typical heat sink of the same dimensions as the TEG and MOSFET device, and the second was a low estimate of the thermal resistance of a typical heat sink. The results are shown in Figure 3.19 and Figure 3.20. The last point on each plot shows the last operating point of thermal stability. Values of TEG leg heights higher than the last point on these plots do not have a steady state solution. The temperature beyond this point increases infinitely with time. This is referred to as thermal runaway.

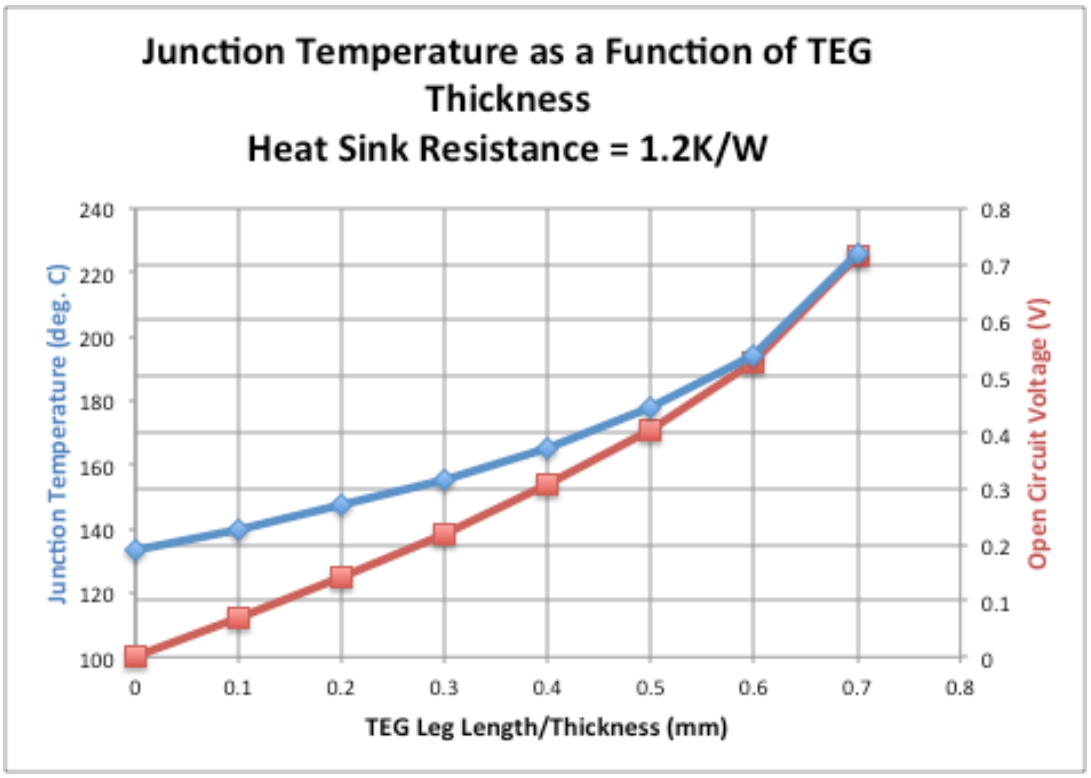

Figure 3.19 – One-dimensional thermal analysis of junction temperature with varying TEG leg heights and a heat sink resistance of 1.2 K/W. Open circuit voltage corresponds to the red line, and junction temperature corresponds to the blue line.

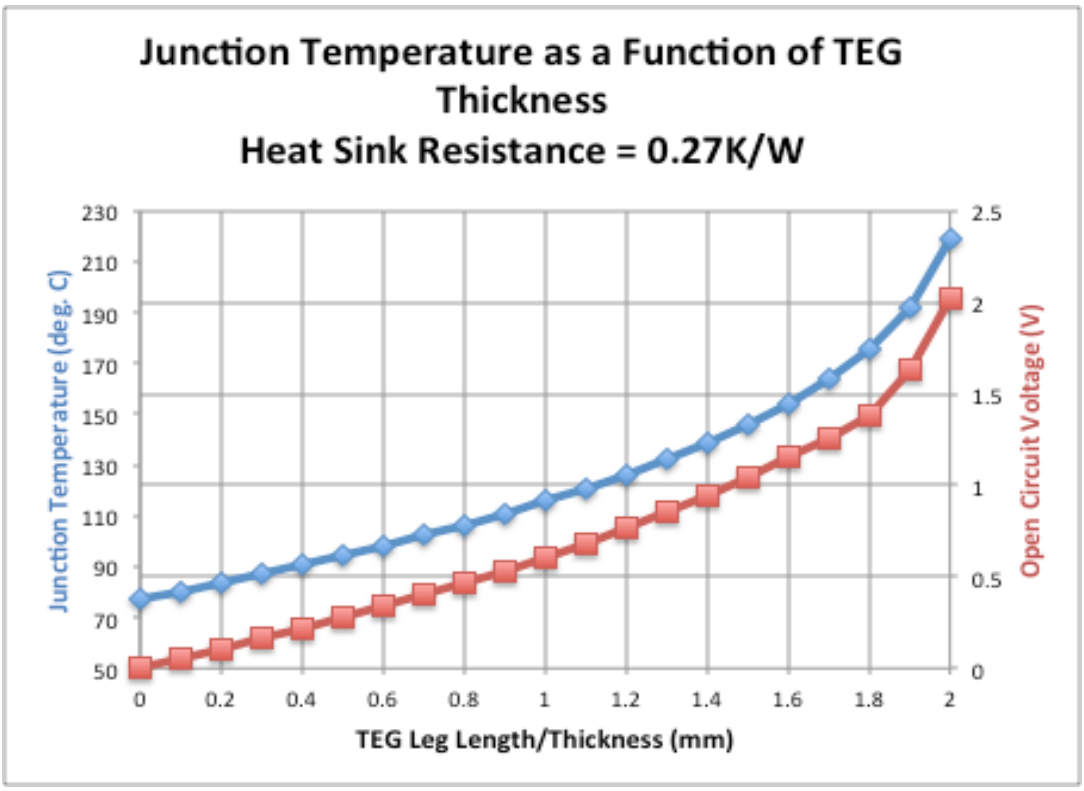

Figure 3.20- One-dimensional thermal analysis of junction temperature with varying TEG leg heights and a heat sink resistance of 0.27 K/W. Open circuit voltage corresponds to the red line, and junction temperature corresponds to the blue line.

Figure 3.21 shows the limits of stability for a given heat sink thermal resistance with respect to the TEG leg height. Below the curve in Figure 3.21 there exists a steady state temperature, and above the curve the system will be in a thermal runaway situation. The maximum operating temperature of this device is 150°C. One can see from Figure 3.19 and Figure 3.20 that this is only achieved with small TEG leg heights. The height of the commercial TEG is approximately 1.26mm tall. Figure 3.20 shows that with a heat sink thermal resistance of 0.27 K/W, a junction temperature of about 133°C is achievable for a TEG leg height of 1.26mm. At this operating point, the open circuit voltage is less than 1V. Knowing the resistance load that the TEG would undergo, one could determine the power output of the TEG. With the power output, the reduction in device efficiency, due to operating the device at a higher temperature, can be compared to the gain in output power from the TEG.

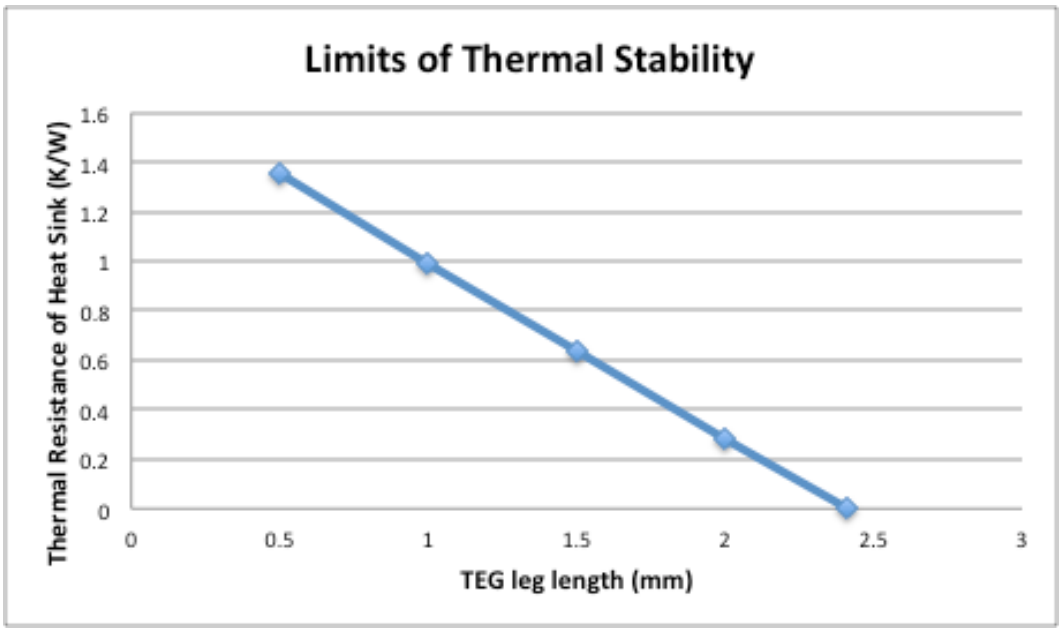

Figure 3.21 - Limit of thermal stability curve for varying TEG heights. Analysis includes a case thermal resistance of 0.6 K/W and thermal interface material resistance of 0.4 K/W.

A heat sink thermal resistance of 0.27 K/W is difficult to achieve with typical forced air-cooling. However, it is within the realm of possibility with liquid cooling. A thermal resistance of 0.033 K/W is achieved with a commercially manufactured cold plate that measures 50mm by 50mm [30]. With liquid cooling technologies, the additional thermal resistance of a TEG may not pose a significant problem in thermal management. However, liquid cooling systems usually require more energy input than air cooled systems. The extra energy input would also need to be taken into consideration when looking at the overall device efficiency.

3.4.1 TEG in Thermal Parallel to Heat Source:

One solution to the thermal resistance dilemma is to place the TEG thermally in parallel as opposed to in series with the electronic components. Solbrekken et al. provide an analysis of a "shunt attach" configuration to provide electrical power from the waste heat of a microprocessor to power a cooling fan [31]. The "shunt attach" configuration presented by Solbrekken et al. is reproduced in Figure 3.22. The configuration allows for two separate heat paths. There is a heat sink thermally in series with the TEG and the microprocessor, the "Primary heat sink", and one in parallel, the "Shunt heat sink". The shunt method offers an alternative heat path than

through the TEG. The heat can either flow through the TEG and the primary heat sink, or it can flow through the heat spreader to the secondary heat sink. A heat spreader and a secondary heat sink would lower the power output that one would be able to achieve out of the TEGs. However, it provides a potential method for using TEGs in a high heat flow systems, where the addition of a TEG might otherwise cause the electronic junction temperature to be too high or to go into thermal runaway.

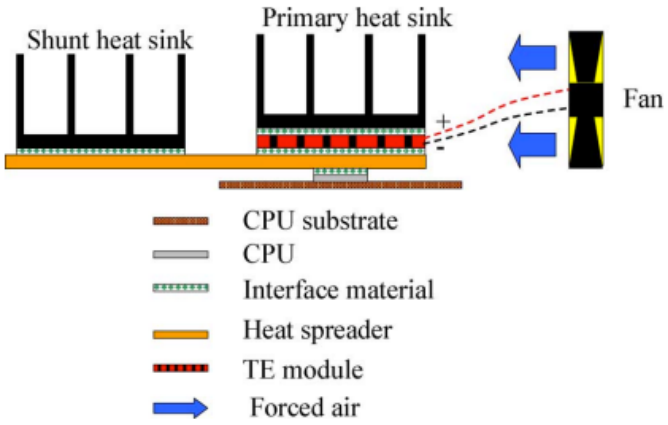

Figure 3.22 - Diagram of the Shunt heat sink design. Copied from Solbrekken et al. [31]

One way that the use of TEGs can be improved for power generation from waste heat produced by electronic devices is to move the TEG closer to the generating heat source. This requires placing the TEG on the chip within the electronic package. The use of ultrathin thermoelectric elements within an electronic package was first analyzed by Chowdhury et al. [32] for the purpose of thermoelectric cooling. Sullivan et al. [33] performed a theoretical analysis of ultrathin thermoelectric generators placed within a micro-electronic package. The TEG module has 49 couples and a total area of 3mm by 3mm. Sullivan et al. considers the effects of the proximity of the TEG to the chip, value of background heat flux, load resistance, and the addition of up to nine TEG modules within the package [33]. Sullivan et al. were able to achieve 72.9mW of useful power generation from a single module [33]. Sullivan et al. did not make any claims on how the chip temperature would be affected with the addition of an ultrathin thermoelectric layer. It is likely that the additional layer would cause an increase in the junction to case thermal resistance and ultimately increase the junction temperature. For the specific

case of the power converter design, only commercially packaged electronics were considered. However, for future research adding thermoelectric elements within the package may be advantageous.

3.4.2 Unified Thermal Core Heat Sink Design:

The analysis presented in Figure 3.19 to Figure 3.21 is for one MOSFET device. However, in the converter prototype it is desired to have sixteen of these devices. Adding sixteen devices to this system will drastically increase the heat input to the system. It is unreasonable to have a 30mm by 30mm TEG and individual heat sinks on all sixteen devices due to size constraints. Therefore, an implementation of a unified heat sink and TEG analysis will be studied further.

Because forced air cooling is likely not going to provide the thermal resistances needed to cool the sixteen MOSFETs with the addition of a TEG, cold plates will be considered for the implementation design. A thermal resistance of 0.033 K/W is achieved with a commercially manufactured cold plate that measures 50mm by 50mm [30]. The thermal resistance of this cold plate will be the basis of the achievable thermal resistance in the design. Because we are seeking a unified heat sink, and would like to maximize the amount of heat going to the TEG, a unified thermal core board design is adopted. The board design can be seen in Figure 3.23. Where the MOSFETs are placed in a square formation with four on each side in the center of the board. In the center of the square, a heat spreading aluminum block is placed thermally in series with the MOSFETs. The cold plate is then attached to the aluminum block.

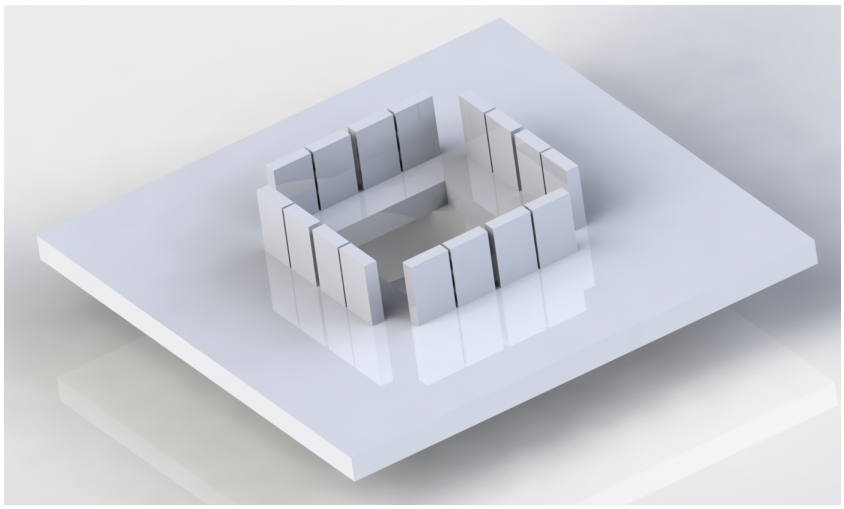

Figure 3.23 - Board configuration for a central core heat sink design

As a first analysis, only one cold plate is simulated using finite element analysis. The TEG is placed between the cold plate and the aluminum heat-spreading block. The cold plate is assigned a thermal resistance of 0.033°C/W and an outer temperature boundary is set as 30°C. The top boundary of the aluminum block is defined as thermally insulated. A volume maximum temperature of the MOSFET blocks for this simulation is calculated in COMSOL to be 561°C, which is far too high for operation, indicating the additional cold plate thermally in parallel is indeed needed for thermal stability.

For the unified thermal core design, placing a secondary heat sink in parallel is accomplished relatively easily. A secondary cold plate is placed on the top of the aluminum block, while the first cold plate and TEG remains at the bottom of the aluminum block. A side view of this design is shown in Figure 3.24.

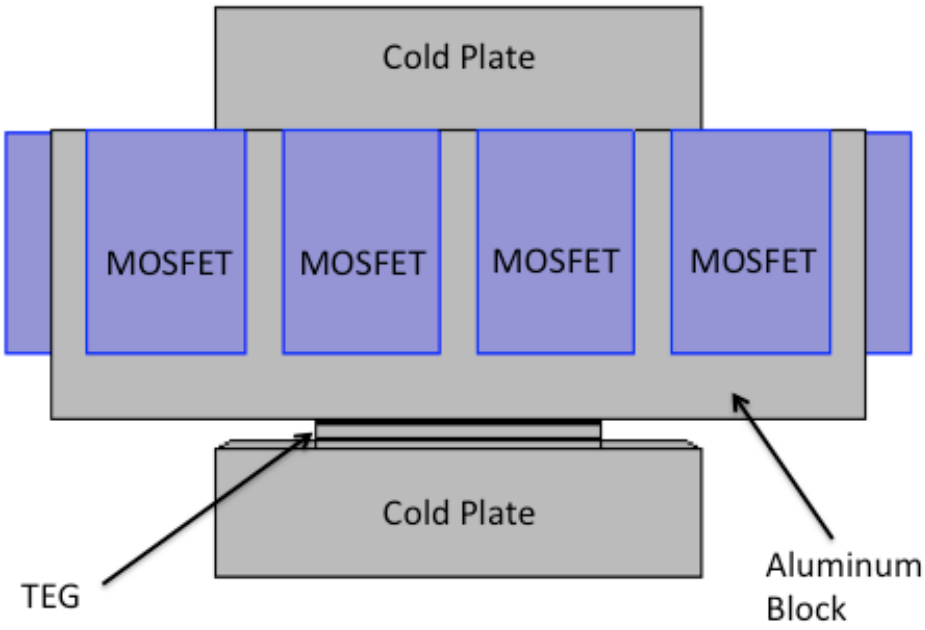

Figure 3.24 - Thermally parallel TEG design for thermal core board design. Image shows the YZ-plane.

For the simulations with two cold plates, as depicted in Figure 3.24, the bottom cold plate is kept at a thermal resistance of 0.033°C/W, while the top cold plate thermal resistance is varied. A parametric sweep of the top cold plate thermal resistance is performed for values of 0.033°C/W to 0.213°C/W. The temperature boundaries are defined as 30°C at the outer boundaries of the top and bottom cold plate. A volume temperature maximum of the MOSFET blocks is calculated for each thermal resistance value. The temperatures at the hot and cold side of the TEG are calculated as surface averages in COMSOL. The temperature difference from the hot to the cold side of the TEG is plugged into the realist theoretical TEG output power model, Equation 3.21, to determine the maximum power output that could be achieved. Results from both the commercial TEG as well as the optimized dimension TEG were obtained. As a base case, a simulation of only the top cold plate with no TEG or bottom cold plate is also performed. In this simulation, the bottom of the aluminum block is insulated and the thermal resistance of the single top cold plate is varied. The TEG power output as well as the required thermal resistance of the top cold plate for a maximum MOSFET temperature of 105°C is shown in Table 3.5. While the MOSFET temperature is maintained at 105°C for this analysis, the heat dissipation in the simulation is defined as

the maximum heat dissipation from the MOSFET devices. This would correspond to the heat dissipation at 150°C junction temperature. By choosing the maximum heat dissipation, one is able to perform a worst-case scenario analysis.

Table 3.5 - Summary of required thermal resistance of top cold plate along with power output of TEGs

Design Scheme	Power gained from TEG	Required thermal resistance of top cold plate for 105°C
One cold plate with no TEG	0.00W	0.10 °C/W
Commercial TEG	0.21W	0.12 °C/W
Optimized Leg height of TEG	0.45W	0.22 °C/W

3.4.3 Energy Balance with Pumping Costs and TEG:

It is desired to compare the required power input to the cold plates to the power output gained by the TEGs. Assuming that the power consumption of a pump times the thermal resistance achieved by the cold plate is a constant value, one can relate the required thermal resistances to the pumping power consumption. While in reality the relationship of power consumption to thermal resistance is complicated and dependent on a vast amount of system conditions, the simple assumption should give an order of magnitude analysis of the power consumption based on the required thermal resistance. The pump that was purchased for the water-cooling cold plate system has an estimated power consumption of 0.8W based on the flow rate and pressure drop required to achieve a thermal resistance of 0.033°C/W. The multiplication factor of power consumed by achieved thermal resistance is calculated to be 0.0264 W consumed *(°C/W dissipated). The required thermal resistance values given in Table 3.5 are converted to power consumed in watts based on the multiplication factor. The results of the analysis along with the power gained from the TEG based on the COMSOL simulation results are summarized in Table 3.6. The last column of Table 3.6 represents the total power consumed by the system. This is determined by taking the power consumed by the top and bottom cold plates and subtracting it from the power gained by the TEG.

Table 3.6 - Summary of TEG total power consumed for two different TEG types

Design Scheme	Power Consumed by Top Cold Plate	Power Consumed by Bottom Cold Plate	Power gained from TEG	Total Power Consumption of System
One cold plate with no TEG	0.26W	0.00W	0.00W	**0.26W**
Commercial TEG	0.22W	0.80W	0.21W	**0.81W**
Optimized Leg height of TEG	0.12W	0.80W	0.45W	**0.47W**

It is clear from Table 3.6 that even the optimized TEG leg height design still consumes more power than a design that excludes the TEG all together. The integration of the TEG in the current design would not provide any additional power that could be used to improve the overall efficiency of the device. In fact, it would cause an increase in the power needed to run the system, and therefore would decrease the overall efficiency of the device.

The biggest limitation of power output is the limitation in maximum case temperature. With the current MOSFETs, to maintain currents large enough to meet the requested power input goals of the energy conversion unit, the case temperature must remain near 105°C. If the device could operate at higher temperatures without sacrificing electrical function, a higher power output could be achieved and the last column in Table 3.6 would approach zero or negative values. A value of zero would be comparable to a natural convection system that does not require power input into the thermal management system. A negative value would indicate power output in the overall system that could be used to power an electrical component in the board and improve the overall efficiency of the device.

A larger parametric sweep of the thermal resistance of the top heat sink from the COMSOL model shown in Figure 3.24 is performed. Figure 3.25 shows the results of the larger parametric sweep with the total power consumed by the thermal system as a function of the maximum temperature on the MOSFET case obtained from COMSOL. The total power consumed reaches zero at a MOSFET temperature of 170°C. Beyond 170°C the total power consumed is negative, indicating power generation. If the case temperature of the electronic device could maintain good electrical function at

temperatures near or greater than 170°C, the use of a commercial TEG module would be beneficial and could improve the overall efficiency of the device.

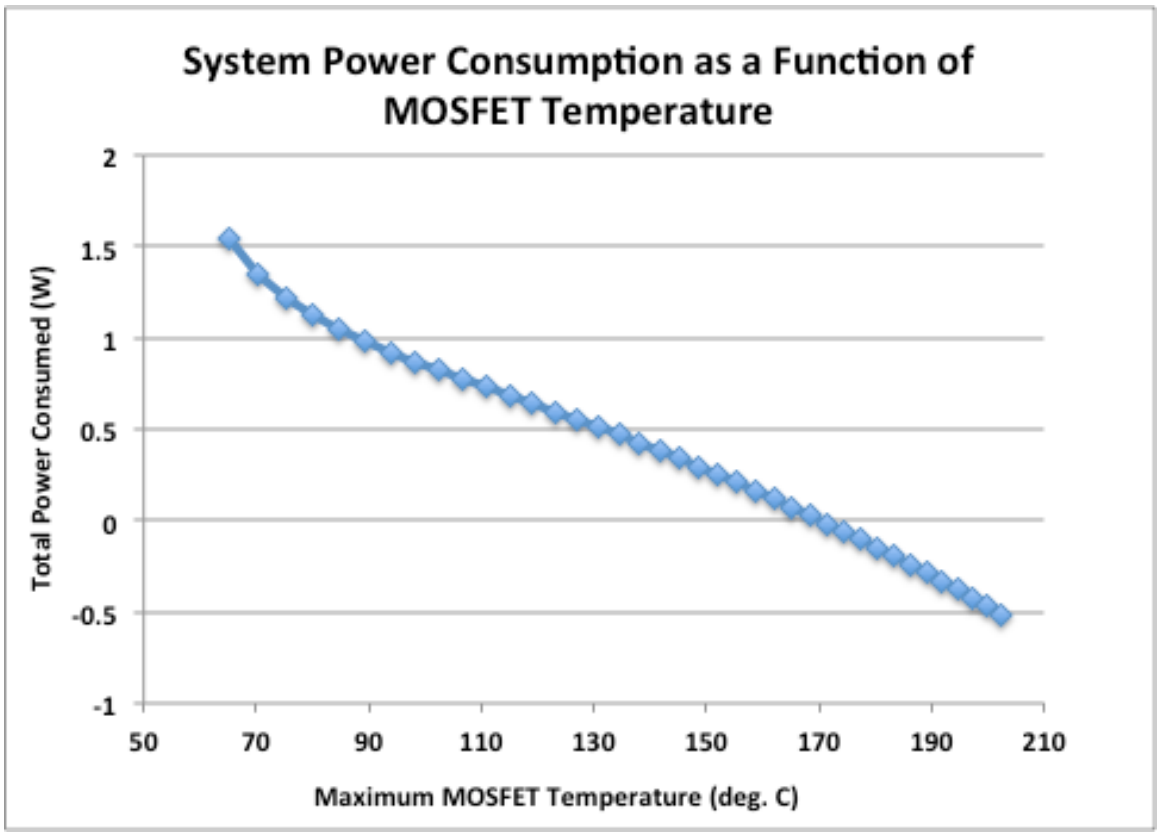

Figure 3.25 - Power Consumed in thermal system at higher MOSFET temperatures.

3.5 Summary and Conclusions:

Waste heat recovery is one idea in the quest to making high efficiency electronic devices. The use of thermoelectric generation is well on its way to becoming a leader in heat recovery technologies. While the thermoelectric effects are not a new revelation, the use of them in waste heat recovery of electronics is relatively naïve. The challenges that face TEGs in the thermal management matrix are significant. One of these challenges is the limitation of TEG efficiency based on the nature of material properties, specifically, the intimate relation between thermal conductivity and electrical resistivity. The additional thermal resistance of a TEG in thermal series with an electronic device is also cause for concern. The additional thermal resistance can cause the electronic device to run at hotter temperatures or as a worst-case scenario, it goes into a thermal runaway situation. When an electronic device remains at hotter

temperatures it often runs less efficiently, which would defeat the purpose of recovering waste heat.

Fortunately, there are several ways around these challenges. Material scientists are on their way to developing materials with satisfactory electrical properties and thermal conductivities close to the theoretical minimum, ultimately increasing the figure-of-merit for the thermoelectric materials. Adding alternative heat flow paths, and having low thermal resistance heat sinks can reduce the negative effects of the additional thermal resistance caused by the TEG. TEGs themselves can be improved by reducing the internal thermal resistance.

It was shown that thermal contact resistances below about 1mΩ do not have a significant effect on the power output. Also careful optimization of the TEG geometry, looking at TEG leg height and thickness of contacting layers, can improve the power output of a particular module. If electronic device efficiency and reliability at higher temperatures improves, the use of current commercial TEGs may be justified. It was shown, for the system considered in this research, that a MOSFET temperature of 170°C is the point where power consumption would equal power generation, reaching a power neutral cooling system, while temperatures above 170°C would generate useful power that could be used elsewhere in the electronic device. While the challenges in heat recovery of electronic devices using TEGs are significant, the solutions provide a direction for future development.

References:

[1] P. Garforth, “Waste Heat Recovery,” in *Encyclopedia of Energy*, Salem Press, 2012.

[2] R.E. Sonntag and C. Borgnakke, “Ideal versus Real Machines,” in *Introduction to Engineering Thermodynamics*, Danvers, MA: John Wiley & Sons, Inc., 2007, ch. 7, sec. 7.9, pp. 201-204.

[3] F.L. Curzon and B. Ahlborn, “Efficiency of a Carnot engine at maximum power output,” *Am. J. Phys.*, vol. 43, pp.22-24, Jan. 1975.

[4] E. N. Miranda, “On the maximum efficiency of realistic heat engines,” *Int. J. Mech. Eng. Educ.*, vol. 35, no. 76, pp. 76-78, 2007.

[5] E. Rebhan, "Efficiency of nonideal Carnot engines with friction and heat losses," *Am. J. Phys.,* vol. 70, pp. 1143-1149, Nov. 2002.

[6] C. B. Vining, "An inconvenient truth about thermoelectrics," *Nat. Mater.*, vol 8, pp. 83-85, Feb. 2009.

[7] D. D. Pollock, "Thermoelectric Phenomena," in *CRC handbook of thermoelectric*, D.M. Rowe, Boca Raton, FL: Taylor & Francis, 1995, ch. 2, pp. 7-17.

[8] W. Liu, Q. Jie, H.S. Kim, and Z. Ren, "Current progress and future challenges in thermoelectric power generation: From materials to devices," *Acta Materialia*, vol. 87, pp. 357-376, Apr. 2015.

[9] D. M. Rowe, "Introduction," in *CRC handbook of thermoelectric*, Boca Raton, FL: Taylor & Francis, 1995, ch. 1, pp. 1-5.

[10] V. Zlatic and R. Monnier, "Physical interpretation," in *Modern Theory of Thermoelectricity*, 1st ed. Oxford, United Kingdom: Oxford University Press, 2014, ch. 4, pp. 17-21.

[11] S. W. Angrist, "Thermoelectric Generators," in *Direct Energy Conversion*, 4th ed. Boston: Allyn and Bacon Inc., 1982, ch. 4, pp. 121-171.

[12] C. J. M. Lasance. (2016, May 1). *How Thermal Conductivity Relates to Electrical Conductivity*. [Online]. Available: https://www.electronics-cooling.com/2000/05/how-thermal-conductivity-relates-to-electrical-conductivity/

[13] H.S. Kim, Z. M. Gibbs, Y. Tang, H. Wang, and G. J. Snyder, "Characterization of Lorenz number with Seebeck coefficient measurement," *APL Materials*, vol. 3, no. 4, Feb. 2015.

[14] M. Beekman, D. T. Morelli, and G.S. Nolas, "Better thermoelectrics through glass-like crystals," *Nat. Mater.*, vol. 14, no. 12, pp. 1182-1185, Nov. 2015.

[15] L. D. Zhao *et al*., "Ultralow thermal conductivity and high thermoelectric figure of merit in SnSe crystals," *Nature*, vol. 508, no. 7496, pp. 373-377, Apr. 2014.

[16] V. Zlatic and R. Monnier, "Introduction," in *Modern Theory of Thermoelectricity*, 1st ed. Oxford, United Kingdom: Oxford University Press, 2014, ch. 1, pp. 1-4.

[17] J. S. Tse and D. D. Klug, "Recent Trends for the Design and Optimization of Thermoelectric Materials – A Theoretical Perspective," in *Thermoelectrics Handbook: Macro to Nano*, Boca Raton, FL: Taylor & Francis Group, 2006, ch. 8.

[18] D. Ebling, K. Bartholome, M. Bartel and M. Jagle, "Module Geometry and Contact Resistance of Thermoelectric Generators Analyzed by Multiphysics Simulation," *J. Electron. Mater.*, vol. 39, no. 9, pp. 1376-1380, Aug. 2010.

[19] X. Hu, H. Takazawa, K. Nagase, M. Ohta and A. Yamamoto, "Three-Dimensional Finite-Element Simulation for a Thermoelectric Generator Module," *J. Electron. Mater.*, vol. 44, no. 10, pp. 3637-3645, Jul. 2015.

[20] COMSOL Multiphysics® v. 5.1. www.comsol.com. COMSOL AB, Stockholm, Sweden.

[21] Thermoelectric Effect User's Guide. COMSOL Multiphysics® v. 5.1. COMSOL AB, Stockholm, Sweden. 2015.

[22] Cree, "Silicon Carbide Power MOSFET C2M™ MOSFET Technology," C2M0045170D datasheet, [Revised Jun. 2016].

[23] A. Griesmer. (2014). *Size parameters for free Tetrahedral Meshing* [Online]. Available: https://www.comsol.com/blogs/size-parameters-free-tetrahedral-meshing-comsol-multiphysics/

[24] L. L. Baranowski, G. J. Snyder and E. S. Toberer, "Effective thermal conductivity in thermoelectric materials," *J. Appl. Physics*, vol. 113, no. 20, 2013.

[25] G. Min and D. M. Rowe, "Optimisation of thermoelectric module geometry for 'waste heat' electric power generation," *J. Power Sources*, vol. 38, pp. 253-259, 1992.

[26] D. M. Rowe and G. Min, "Design theory of thermoelectric modules for electrical power generation," *IEEE Proc.-Sci. Meas. Technol.,* vol. 143, no. 6, pp. 351-356, Nov. 1996.

[27] Y. Kim, G. Yoon and S. H. Park, "Direct Contact Resistance Evaluation of Thermoelectric Legs," *Exp. Mech.*, vol. 56, pp. 861-869, Feb. 2016.

[28] B. T. Admasu, X. Luo and J. Yao, "Effects of temperature non-uniformity over the heat spreader on the outputs of thermoelectric power generation system," *Energy Convers.*, vol. 76, pp. 533-540, Aug. 2013.

[29] G. Min and D. M. Rowe, "Peltier Devices as Generators," in *CRC handbook of thermoelectric*, Boca Raton, FL: Taylor & Francis, 1995, ch. 38, pp. 479-488.

[30] (2016). *PLT-UN50F cold plate, 50mm x 50mm (1.97in x 1.97in): Specification*. [Online]. Available: http://koolance.com/cold-plate-50mm-plt-un50f

[31] G. L. Solbrekken, K. Yazawa and A. Bar-Cohen, "Heat Driven Cooling of Portable Electronics Using Thermoelectric Technology," *IEEE Trans. Adv. Packag.*, vol. 31, no. 2, pp. 429-437, May 2008.

[32] I. Chowdhury, R. Prasher, K. Lofgrenn, G. Chrysler, S. Narasimhan, R. Mahajan, D. Koester, R. Alley and R. Venkatasubramanian, "On-Chip Cooling by Superlattice-Based Thin-Film Thermoelectrics," *Nat. Nanotechnol.*, vol. 4, no. 4, pp. 235-238, 2009.

[33] O. Sullivan, M. P. Gupta, S. Mukhopadhyay, S. Kumar, "On-Chip Power Generation Using Ultrathin Thermoelectric Generators," *J. Electron. Packag.*, vol. 137, Mar. 2015.

Chapter 4: Power Converter Design and Future Progress

Power electronics are used anytime there is a nominal voltage change or an electrical energy conversion from AC to DC or vise versa. They are used extensively in our modern world. With a continual push toward smaller electronic devices, comes the need for more effective thermal management. Unlike the progress in electrical components, which doubles in complexity every year according to Moore's law [1], technology in heat dissipation has stayed relatively constant since the 1990s. For system level cooling, or cooling outside of the electronic package, air-cooled heat sinks are still the most common choice [2].

The research presented has been funded through an SBIR grant with the purpose of developing a multi-stage, multi-phase, high efficiency electrical energy conversion unit. The previous chapters have outlined the thermal need and basic heat transfer principles (Chapter 1), considered specifically parallel plate heat sinks and the prediction of thermal resistance using correlations and finite element analysis simulation (Chapter 2), analyzed the feasibility of heat recovery with thermoelectric generators using current heat sinking designs (Chapter 3). This chapter will look specifically at the power converter heat sink design and thermal performance predictions based on correlation estimates and finite element analysis. Consideration of future work and progress with the current heat sinking design will also be discussed.

4.1 Power Converter Design:

In electronic cooling, a common trend is to establish a board configuration that places the highest heat dissipating components as far apart as possible with individual heat sinks on the these devices. However, another approach is to use a unified heat sink that is thermally connected to the highest heat dissipating devices. While this increases the heat load that must be dissipated by the one heat sink, the total required heatsink volume can be smaller. It often creates a more compact thermal solution. Central core heat dissipation is not a new concept. The 2013 Mac Pro® has an extremely compact design with a single heat sink in the center of the tower, a volume of 5E-3m^3 and a weight of 11lbs [3]. This is nearly an order of magnitude smaller than the 2012 Mac

Pro® tower with a volume of 5E-2m^3 and a weight of approximately 40lbs [4]. Often times in electronics cooling, the board design does not take into account thermal considerations. However, as seen with the 2013 Mac Pro®, by taking into account thermal management at the board level, the complete product can be more compact. An image of the 2013 Mac Pro® can be seen in Figure 4.1.

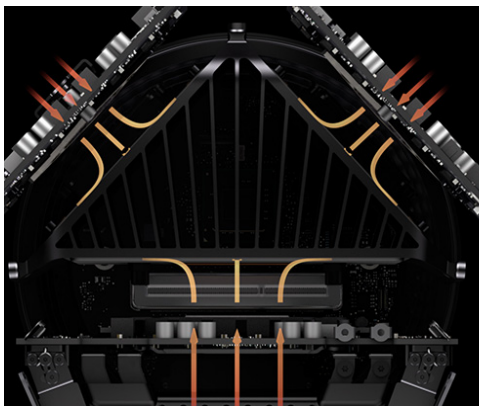

Figure 4.1 - 2013 Mac Pro® thermal core heat sink image [3].

As an initial evaluation, the 2013 Mac Pro® is evaluated using finite element analysis simulation in COMSOL Multiphysics. The geometry specifications are estimated from the dimensions given by the Mac Pro® web page [3]. For simplicity the model geometry will have vertical fins, as opposed to the slightly angled fins of the Mac Pro® heat sink. The full heat sink model is simulated. The diameter of the computer itself is approximately 168 mm. The tallest fin in the heat sink is only about half the length of the diameter. Whereas the width of the heat sink (or the base of the heat sink) is about the length of the diameter. Therefore the dimensions of the modeled heat sink will have a base of length 168 mm and a maximum fin height of 84 mm. There are 17 fins that are approximately 1mm thick. That leaves a fin spacing of approximately 8.38 mm. The maximum heat load is given as 450W, and the ambient operating range is given as 10°C to 30°C [3]. For the simulation, an ambient temperature of 293.15K (20°C) is used. The ambient temperature is defined at the inlet flow condition. A volumetric flow rate of 25 CFM is chosen as a reasonable flow rate that could be provided by a fan. The volumetric flow rate can be modeled as a laminar inflow profile with an average velocity of approximately 1.68 m/s. The outlet fluid flow condition is defined as zero pressure. The geometry and applied boundary conditions can be seen in Figure 4.2 and Figure 4.3.

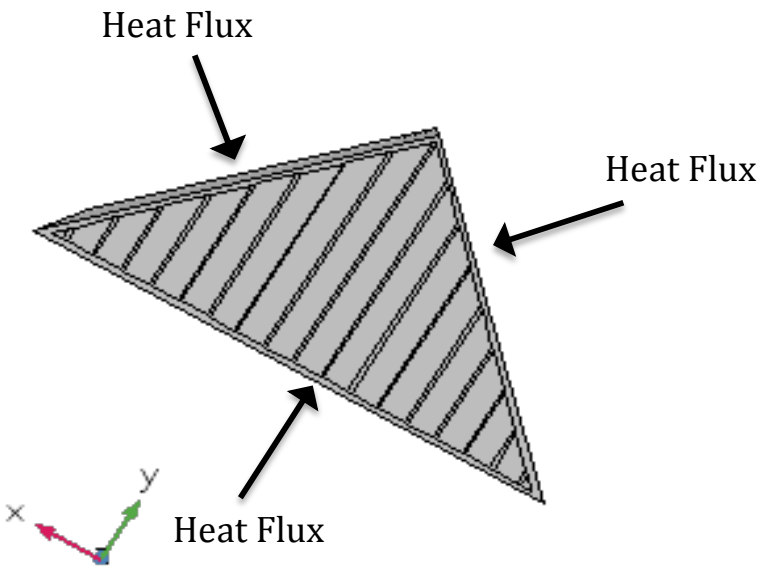

Figure 4.2 - X-Y Geometry and total heat flux boundary conditions.

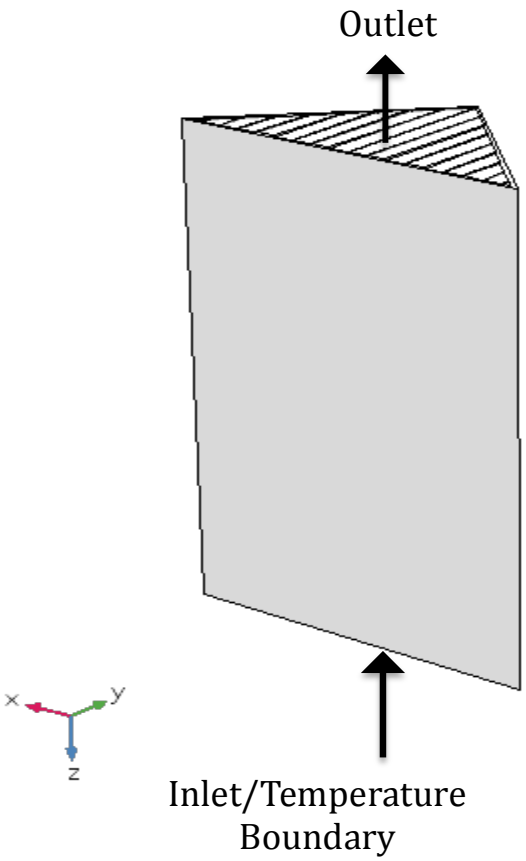

Figure 4.3 - Full Geometry with inlet and outlet boundary conditions shown as well as the ambient temperature boundary shown.

Figure 4.4 shows the temperature profile of the heat sink and fluid domains. As consistent with Figure 4.3, the bottom side of the heat sink is the inlet, while the top is the outlet. From the temperature profile, one can see that the top corners of the heat sink are the hottest. This is what one would expect for a triangular geometry with vertical fins in one direction. The maximum temperature of the heat sink is evaluated by using the derived values volume maximum tool for the aluminum heat sink domain. The maximum temperature was calculated to be 83.5°C, which is a high, but a reasonable temperature for a CPU, as a typical CPU fails at about 85°C to 95°C. When considering that the maximum temperature is calculated for the maximum heat load, which the computer would likely not be experiencing for long periods of time, this is an acceptable maximum temperature value.

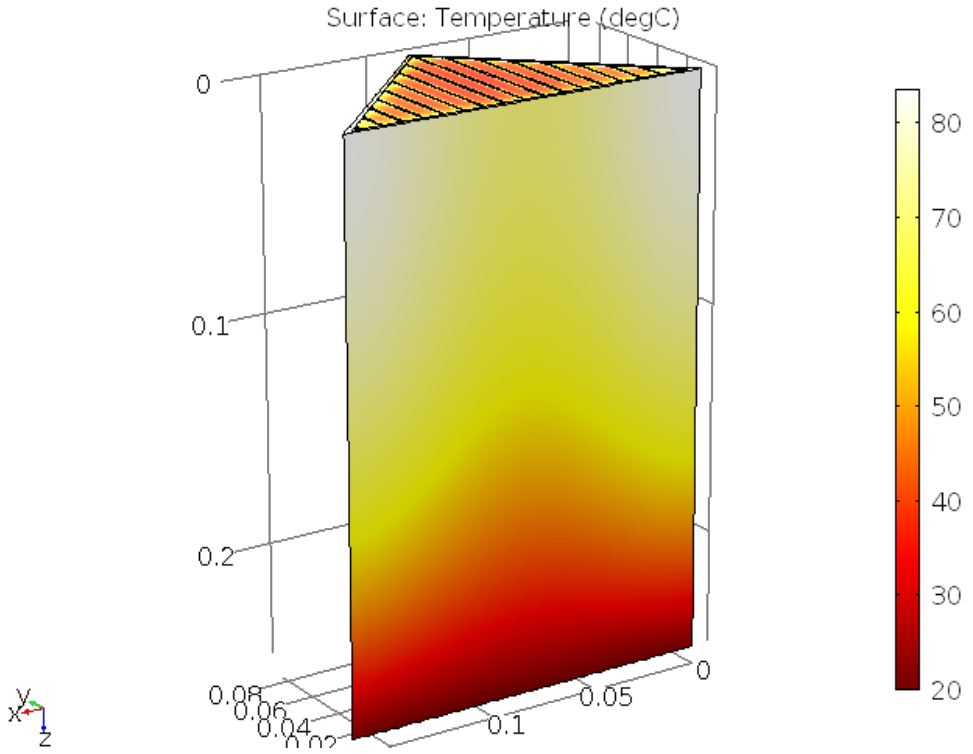

Figure 4.4 - Temperature profile of the aluminum heat sink and air domains. Figure shows the outlet side of the heat sink at the bottom.

From the derived values volume maximum tool, the thermal resistance for the heat sink can also be determined. By inputting the expression for thermal resistance and calculating for the heat sink domain, one obtains a thermal resistance value of 0.141°C/W. Assuming that there is no thermal resistance loss due to conduction, a fair

assumption for materials with high thermal conductivities such as aluminum, the convective heat transfer coefficient can be calculated from the thermal resistance and the surface area available for heat transfer. The calculated convective heat transfer for a thermal resistance of 0.141°C/W with this heat sink surface area is 16.75 W/m^{2}K. This value is within the range of forced air convective heat transfer coefficients [5].

As a way to further check the validity of the solution, the rise in fluid temperature is compared to the simple energy balance given by $q = C_p \dot{m} \Delta T$. For the heat flux and air flow rate used in the simulation, the predicted ΔT or rise in fluid temperature from inlet to outlet is 32.0°C. Using the derived values surface average tool in COMSOL, the average temperature at the outlet air boundary is 49.4°C. This gives a temperature difference between entrance, defined as 20°C, and exit air of 29.4°C. This values is in agreement with the theoretical value and indicates that the model is running as expected.

Taking the same approach to thermal management as adopted in the 2013 Mac Pro®, the highest heat dissipating devices are moved to the center of the board. For the energy conversion unit, the highest heat dissipating components will be the switching devices. The switching devices for the current design are SiC MOSFETs. The power MOSFETs are moved to the center of the board, with the idea of passing fluid through the center of the board. In order for fluid to pass through the center of the board, a hole is cut out of the board's center. The transformer used for the energy conversion unit is a torroid transformer. This type of transformer is shaped like a donut, a short cylinder with a cylindrical hole in the center. The torroid transformer, which will also produce a significant amount of heat, is placed in the center of the board on the backside, underneath the MOSFETs. This allows flow through the center of the torroid transformer and then through the center of the board past the MOSFETs. A top view of the board design can be seen in Figure 4.5, provided by the senior design team working on the design, machining and testing of the power converter heat sink. The sixteen vertical boxes are the power MOSFETs. The transformer is on the bottom side of the board and is not in view of Figure 4.5.

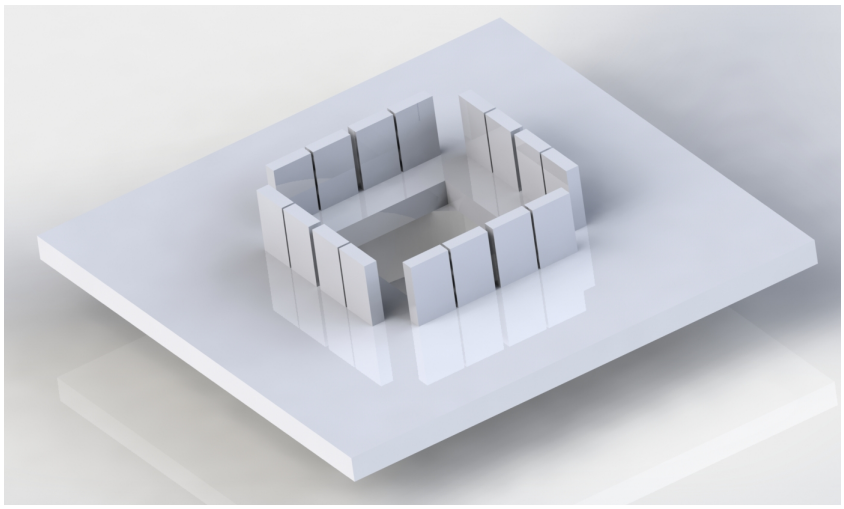

Figure 4.5 - Board configuration for a central core heat sink design

The heat sink will be centered on the topside of the board, thermally connected to each of the sixteen MOSFETs. In order to get effective heat transfer, the heat sink is made of a conductive metal, aluminum, to allow effective heat transport from the MOSFET devices on the perimeter to the center of the heat sink. The heat sink also needs to have fins, or holes that allow sufficient fluid flow, for maximum convective heat transfer, while still maintaining a high surface area available for convective heat transfer.

Using the on-resistance of the MOSFETs, as described in Chapter 1, the heat dissipation per MOSFET can be determined. The required heat sink thermal resistance to maintain a specified junction temperature is calculated based on the heat dissipation, the expected ambient temperature, and the thermal resistance through the package and interface. This required thermal resistance is calculated in Chapter 1 for both individual device heat sinks, and a heat sink based on sixteen MOSFET devices. For the unified thermal core design, the required heat sink thermal resistance will need to be able to dissipate the heat from sixteen MOSFET devices. The required thermal resistances for sixteen MOSFETs at three different component junction temperatures are reproduced from Chapter 1 in Table 4.1.

Table 4.1 – Required heat sink thermal resistance

Junction Temperature of Each MOSFET	Heat Output per MOSFET calculated from on-resistance with duty cycle of 50%	Required Heat Sink Thermal Resistance for sixteen MOSFETs at ambient Temperature of 20°C
150°C	16.6W	0.47°C/W
125°C	14.5W	0.43°C/W
100°C	12.3W	0.39°C/W

In order for the heat sink to keep the junction temperature at or below the specified temperatures in Table 4.1, the heat sink needs to be operating with a thermal resistance at or below the corresponding thermal resistance presented in Table 4.1. A custom air-cooled heat sink was designed and developed as part of a mechanical engineering senior design project to meet the thermal needs of the power converter.

The engineering senior undergraduate students working on the design, and manufacturing of the heat sink developed two different air-cooled designs, both of which they manufactured and tested. The first design is shown in Figure 4.6. The heat sink consists of vertical fins extending from the perimeter of the heat sink. The fins have different heights, increasing toward the center and decreasing toward the corners to make triangles. The second design is shown in Figure 4.7. This design incorporates a crossed parallel plate design. It consists of four plates that have fourteen rectangular slots with curved corners oriented in one direction. These four identical plates are stacked, turning the plate being stacked 90° from the plate underneath to get crossed parallel fins.

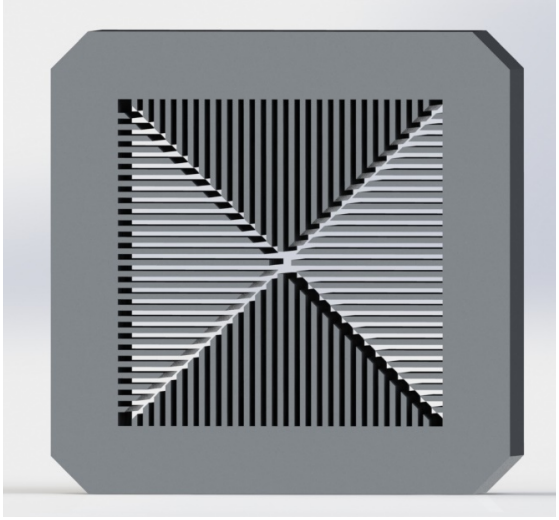

Figure 4.6 - Triangular heat sink configuration.

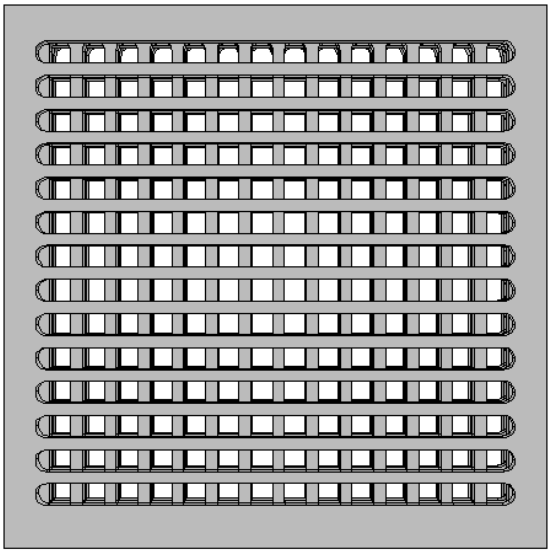

Figure 4.7 - Cross parallel plate heat sink configuration.

Alongside the fabrication of the custom air-cooled heat sink, a water-cooled system was also considered. Off the shelf commercial cold plates have sufficiently low thermal resistances for the needs of the power converter. A water-cooled cold plate was purchased from Koolance, along with a radiator and pump. The cold plate is 50mm by 50mm and is easily mounted to a block that the senior design team machined to fit into the square hole of the board design (Figure 4.4). The cold plate has an expected thermal resistance of 0.033°C/W at a 5L/min flow rate. The specified pressure drop at 5L/min is 0.9psi or 6.2kPa. The thermal resistance is well below the required thermal resistance

given in Table 4.1, and should easily be able to handle the heat load of the power converter. However, the cold plate may require more energy input, as the pressure drop in water-cooled systems are typically greater than air-cooled systems, and higher pressure drop corresponds to higher required pumping power. It also weighs more than the air-cooled systems. These factors are considered when choosing the overall best heat sink design.

4.1.1 Predicted Performance of Triangular Heat Sink:

An analysis based on the convective heat transfer correlation developed by Teertstra et al. [6] for parallel plates and the pressure drop analysis presented by Culhman and Muzychka [7] is conducted to predict the thermal performance of the two air cooled heat sink designs. The correlations are discussed in further detail in Chapter 2. From the correlations an estimated pressure drop and thermal resistance as a function of the fluid flow rate can be determined. The pressure drop can then be compared to a fan curve to obtain a predicted operating flow rate and expected thermal resistance at this predicted operating flow rate.

The first heat sink, with four triangular sections, is modeled as parallel plates that are a height exactly halfway between the tallest and the shortest fin. Treating all of the fins at this height makes the solution much simpler and should provide a reasonable estimate. Also for simplicity, only one side, $1/4^{th}$, of the total heat sink is modeled. The thermal resistance is calculated based on the surface area of the full heat sink and the heat transfer coefficient predicted by the correlation prediction. The volumetric flow rate is scaled to $1/4^{th}$ of the entrance area and the channel velocity is determined based on a set of 27 channels. The pressure drop curve produced by the analytical correlations is compared to the fan curve of a high performance, 24V DC fan XC Series produced by Orion Fans. The pressure drop and fan curve cross at a flow rate of approximately 55CFM. At 55CFM, the predicted thermal resistance for the full heat sink is 0.09 K/W. The operating curve, with the pressure drop, thermal resistance, and fan curve is plotted in Figure 4.8.

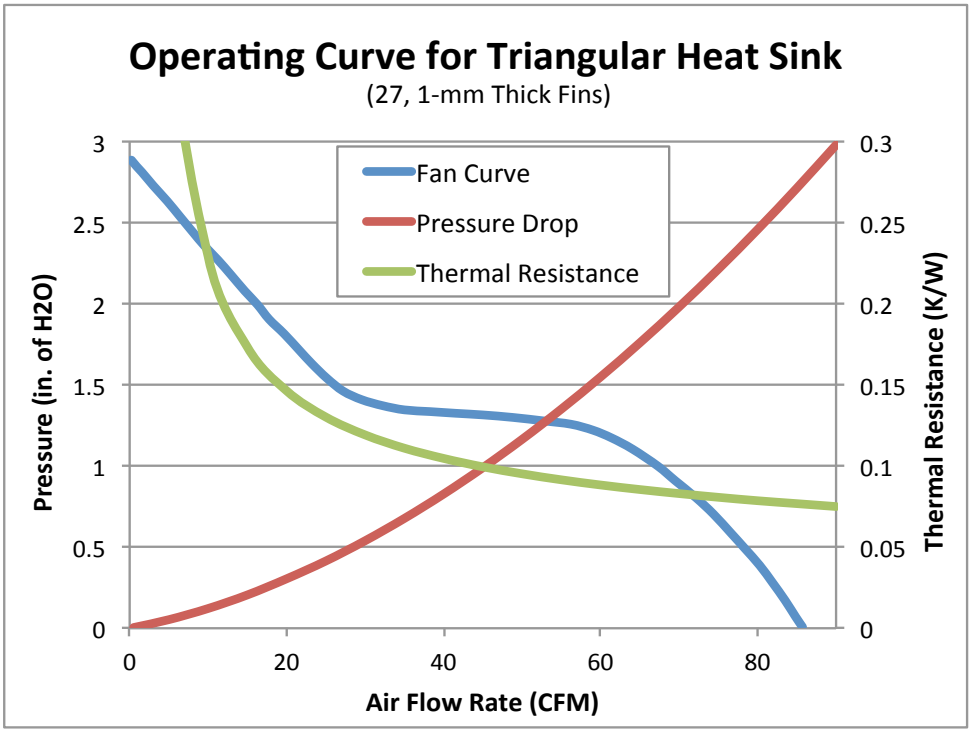

Figure 4.8 - Operating curve predicted by analytical correlation for triangular heat sink.

The triangular heat sink is also simulated using finite element analysis simulation with the program COMSOL Multiphysics. This program enables the coupling of physical phenomena, such as fluid flow and heat transfer, to obtain a composite solution.

The heat sink with triangular fins has internal symmetry, and only one fourth of the model is simulated. An overall heat transfer rate of 112W is applied on the bottom of the heat sink, this is one forth of the total heat load produced by the sixteen MOSFETs at a 100% duty cycle. As recommended by Bons [8], an entrance region of 1X the length of the heat sink and an exit region of 3X the length of the heat sink are constructed into the model. A thermal outflow boundary condition is applied at the exit of the model. An outflow boundary condition is applied to boundaries that have heat leaving the system primarily by convection. It assigns a zero temperature gradient in the normal direction with no radiation. A temperature boundary of 293.15K and a normal inflow velocity of 3m/s are applied to the inlet. This velocity corresponding to approximately 10CFM for flow through the full heat sink geometry. Unfortunately, convergence problems arose when simulating higher flow rates. The outlet is given a zero pressure boundary condition. A symmetry boundary condition is applied at the channel opening at the top

of the quarter heat sink model along with the entrance and exit side boundaries. The symmetry boundary prescribes a vanishing shear stress, unlike the default wall boundary condition. The simulated geometry with boundary condition locations can be seen in Figure 4.9.

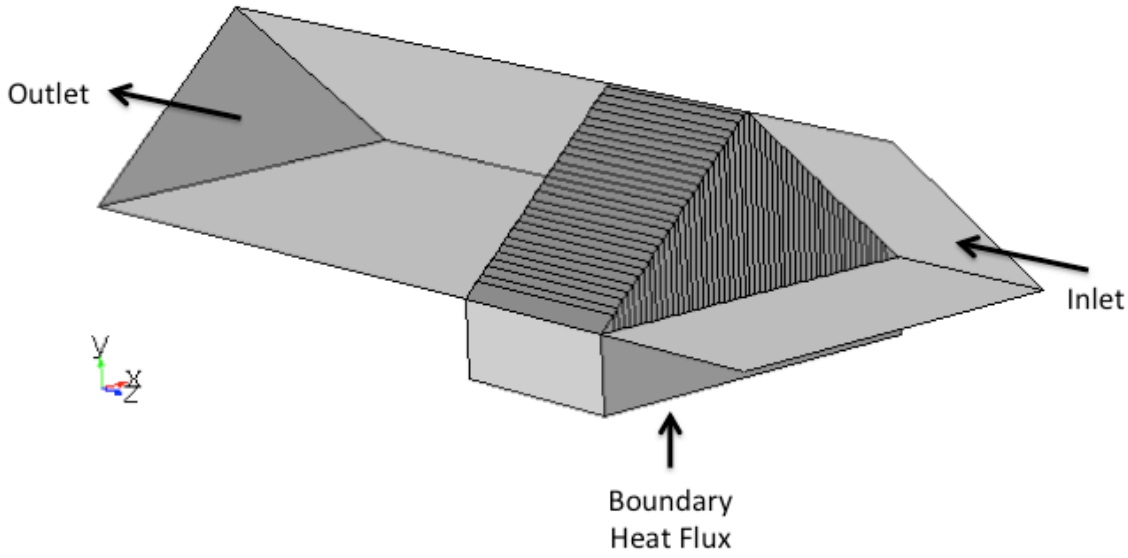

Figure 4.9 - Simulated geometry with some boundary condition locations identified.

The mesh is a user-controlled mesh with free tetrahedral elements of 'fine' size through the channels, and 'extra fine' elements on the fins. A boundary layer mesh is applied on the channels to account for boundary layers on the channel walls. The boundary layer mesh has a dense element distribution in the normal direction along the boundaries, which is good for fluid flow [9]. There are 468277 elements in the mesh, with a minimum element quality of 0.002 and an average element quality of 0.4156. While the element quality is a relatively low, meshes of a finer size had significantly longer computational time and experienced a significant number of convergence errors.

For a flow rate of 10CFM, the average rise in fluid temperature is simulated as 97.0°C. This corresponds relatively well to the simple heat balance equation $q = C_p \dot{m} \Delta T$, which with the flow rate, $0.0012 m^3/s$ (10CFM scaled to $1/4^{th}$ of the geometry) and heat input, 112W, into the model and the heat capacity of air gives a temperature difference of 88.9°C. The 9.1% discrepancy between the theoretical value and the simulated value could be due to the fluid flow variations within the simulated channel

velocity, or due to the temperature dependence of the fluid properties, which are not accounted for in the analytical model.

The average pressure drop at the exit of the channels in the finite element analysis simulation is calculated using the derived function as 32.6 Pa for 10CFM. The analytical model for pressure drop at 10CFM gives a pressure drop of 30.4 Pa, which is slightly lower than that predicted by the COMSOL simulation. The average velocity entering the channel calculated from the derived values in COMSOL is 1.74m/s. The maximum velocity entering the channel is 3.5m/s. The velocity calculated by the volumetric flow rate and the number of channels in the heat sink in the analytical model is 2.91m/s. It is likely that the slight discrepancy is due to different channel velocities between the COMSOL simulation and the analytical model. The velocity profile of the finite element simulation can be seen in Figure 4.10. One can see that the velocity entering the channels is higher for the end channels. These end channels are likely causing the average pressure drop at the exit to be slightly higher than predicted by the analytical model, which assumes channels of equal height half way between the tallest and shortest channel. When the analytical model is run for a velocity of 3.5m/s, the maximum velocity at the inlet of any channel, the corresponding pressured drop is 34.9Pa, which is higher than the average pressure drop given by the simulation. Therefore, the average pressure drop calculated in the COMSOL simulation is within the correct range based on the maximum and minimum velocity through the channels.

The average thermal resistance calculated from the COMSOL simulation at 10CFM is 0.93°C/W. This value is compared to the analytical prediction of 0.92°C/W at a flow rate of 10CFM. The analytical correlation and COMSOL simulation agree quite well at 10 CFM. The temperature profile of the finite element simulation is shown in Figure 4.11.

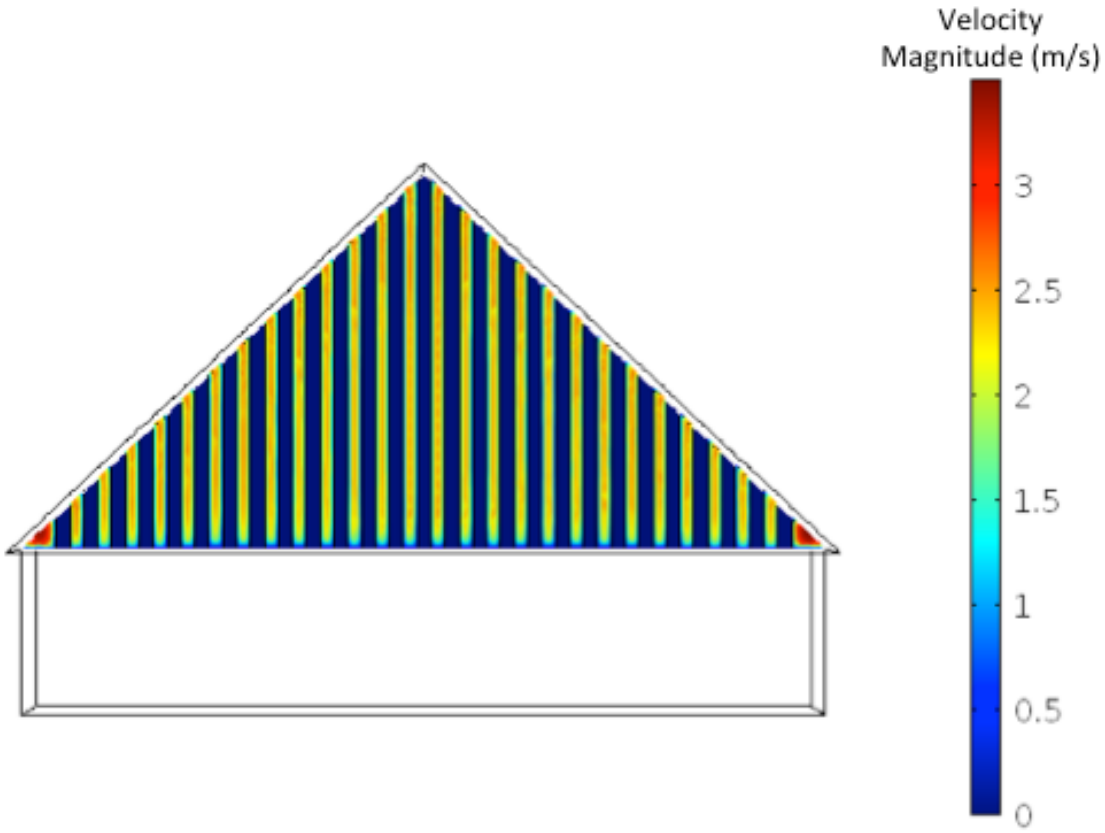

Figure 4.10 - Velocity profile at the inlet of the channels, simulated in COMSOL Multiphysics.

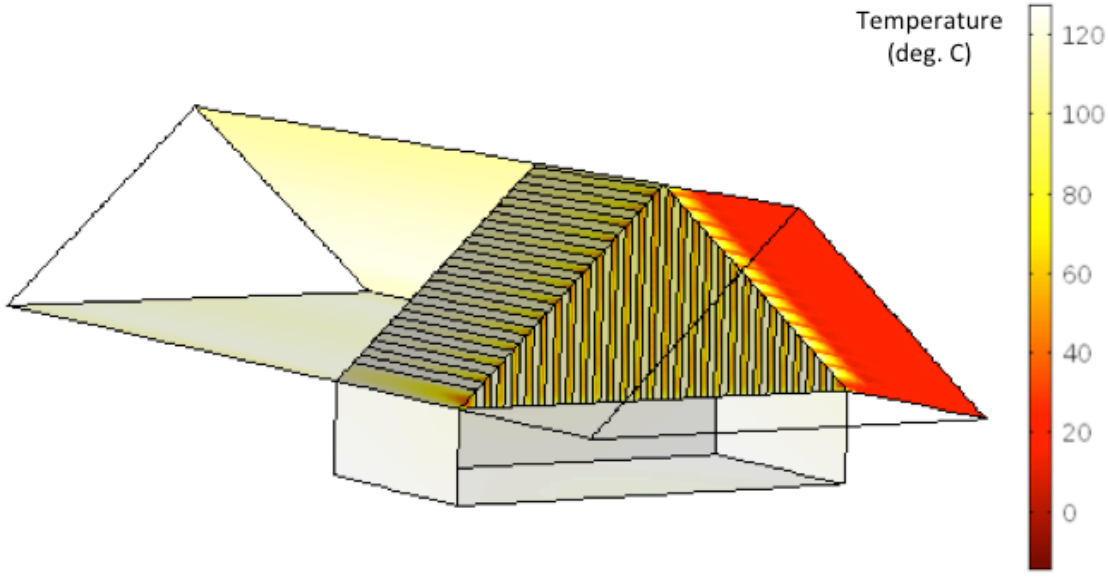

Figure 4.11 - Temperature profile of triangular heat sink produced using COMSOL Multiphysics.

4.1.2 Predicted Performance of Cross Finned Heat Sink:

The second heat sink, with the cross fins, is also analyzed using the convective heat transfer correlation developed by Teertstra et al. [6] for parallel plates and the pressure drop analysis presented by Culhman and Muzychka [7]. The pressure drop is analyzed based on the hydraulic diameter of the rectangular openings of the fins and the thickness of the entire heat sink in the direction of fluid flow. The channel velocity is determined by first scaling the total flow rate to the flow rate through the 14 initial parallel rectangular channels. This flow rate is used to calculate an approach velocity for the 14 square openings available for fluid flow in the cross-finned section. From the approach velocity, a channel velocity through the 14 square openings is calculated. This channel velocity is used to evaluate the pressure drop. The channel velocity through the square openings is likely a maximum value, as the highest velocity flow will be experienced at the cross-finned section. Using this velocity, should give a slight overestimate of the pressure drop. The surface area available for heat transfer is taken as 4 times the inside area of the rectangular slots on one plate. Once again the pressure drop of the high performance 24V DC fan XC Series produced by Orion Fans is plotted with the estimated pressure drop of the cross-finned heat sink. The pressure drop and fan curve cross at a flow rate of approximately 68CFM. At 68CFM, the predicted thermal resistance is 0.13 K/W. The operating curve, with the pressure drop, thermal resistance, and fan curve is plotted in Figure 4.12. The analytical correlation does not take into account any recirculation that is likely to occur between the fin openings after the crossed section.

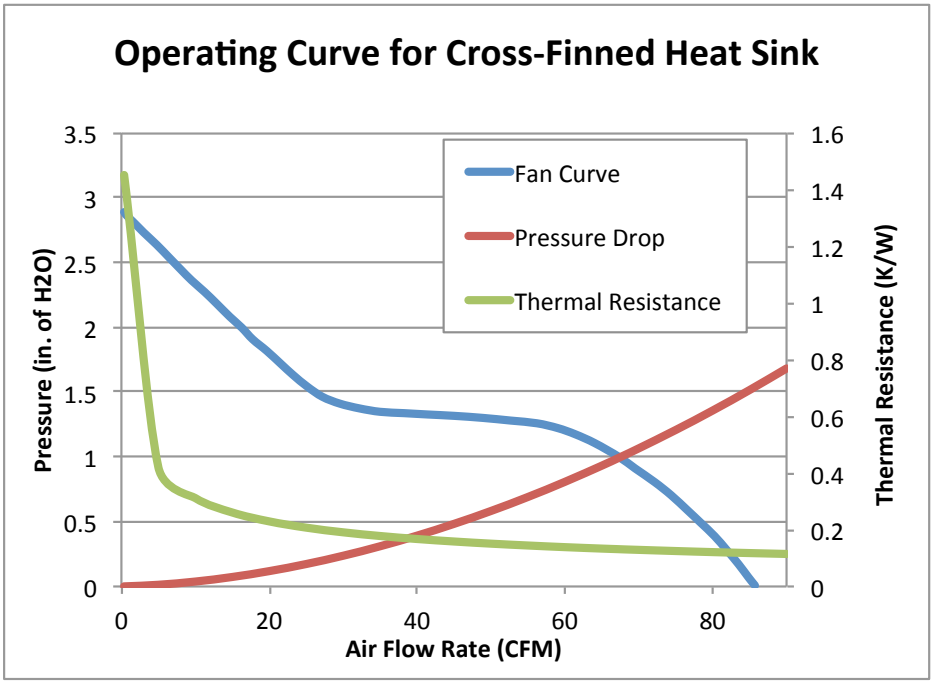

Figure 4.12 - Operating curve predicted by analytical correlations for the cross-finned heat sink.

Unfortunately, significant convergence errors arose when trying to model the cross-finned heat sink with finite element analysis in COMSOL Multiphysics. Therefore, simulation results are not included for the cross-finned heat sink in this work.

4.1.3 Experimental Results:

The mechanical engineering senior design team, consisting of James Sutton, Connor Trulock, and Caleb Jo, conducted thermal tests on the two air-cooled heat sinks and the liquid cooled cold plate. Their tests used resistors as the heat source with defined power inputs. They performed tests with one fan and two fans. For the one fan test, there was a single fan on the side of the case pulling air out of the case. In the two fan system there was an additional fan placed directly above the heat sink pulling air through the fan. Using an IR camera, they recorded temperatures over the course of 30 minutes, at which point the system appears to be at steady state. Their experimental results are summarized in Table 4.2 along with the predicted thermal resistance presented in the previous two sections. The analytical and COMSOL simulations most closely represent the test conditions with two fans.

Table 4.2 - Experimental results from senior design team compared to theoretically predicted thermal resistances for the air-cooled heat sinks.

Testing Variable	Water-cooled Cold Plate	Triangular Heat Sink with 1 Fan	Triangular Heat Sink with 2 Fans	Cross Finned Heat Sink with 1 Fan	Cross Finned Heat Sink with 2 Fans
Predicted Thermal Resistance (K/W)	-	-	0.09	-	0.13
Experimental Thermal Resistance (K/W)	0.09	0.19	0.17	0.19	0.17

From Table 4.2 it can be seen that the analytical correlation predicts a thermal resistance much lower than what was observed experimentally. The machining of the triangular heat sink proved to be difficult, and some of the fins in the physical heat sink were not evenly spaced or at the same thickness. These changes in the fin spacing and fin thickness would cause the fluid flow through the heat sink to be different than predicted by the correlations, which in turn would cause discrepancy between the analytical predictions and the experimental results.

The cross finned heat sink experimental results are only slightly higher than the predicted analytical correlation. When conducting the experiments, the temperature was taken from the resistor packages. Therefore, the experimental thermal resistance results also include the thermal resistance at the interface, from the resistor case to the heat sink. Both of the analytical correlations only account for the thermal resistance of the heat sink.

4.2 Future Progress and Project Direction:

The two air-cooled heat sinks appear to perform within the thermal needs of the sixteen power MOSFETs for the first prototype. With the extension of the SBIR project, a full-scale 15kW power converter will need to be developed. This will likely be done based on stacking multiple prototype power converter designs. The current air-cooled

heat sink design may be able to provide sufficient cooling with a stacked design. However, with stacked heat sinks, careful consideration of the inlet air of the higher heat sinks will need to be considered. If the heat sinks do not provide sufficient cooling, alternative cooling designs will need to be considered. If heat recovery is implemented, alternative designs will also need to be considered.

While not considered for this phase of the project, custom package design may enable a more compact cooling solutions. The SiC bare die is much smaller than the packaged MOSFET and could reduce the overall size of the converter. There are some interesting conducting dielectric materials that may be able to be used in a custom package design in future work. One of these conducting materials that may be useful is beryllia. Solid beryllia has a thermal conductivity of 325W/m*K and a volume resistivity greater than $10^5\Omega$*cm [10]. Unfortunately, this material can be toxic if inhaled as dust.

4.2.1 System Level Heat Sink Enhancement:

Current trends in the electronic cooling industry take a package based approach, attempting to start the cooling design from within the package. However, there are some ways that system level cooling can be improved that may enable better heat transfer solutions for future work in power converters.

4.2.1.1 Optimization:

Optimization of parallel plate heat sinks may be one method of heat transfer improvement. There is a considerable amount of research on parallel plate heat sink optimum plate spacing for both natural convection and forced convection. Table 4.3 gives a summary of some important optimization studies for both natural and forced convection.

Table 4.3 – Optimization studies performed for natural and forced convection.

Researchers	Fluid Flow Type	Method of Optimization	Optimization Parameters
Elenbaas [11]	Natural Convection of Air	Analytical maximization of heat dissipated for a given temperature	Parallel plate spacing
Levy [12]	Natural Convection of Air	Analytical minimization of temperature for a given heat flux	Parallel plate spacing
Culham & Muzychka [7]	Forced Convection of Air	Analytical minimization of entropy generation	Number of fins, Fin thickness, Fin height, Velocity
Lee [13]	Forced Convection of Air	Parametric analytical simulations to minimize thermal resistance	Number of fins
Bornoff et al. [14-16]	Forced Convection of Air	Computational fluid dynamics to reduce thermal bottleneck	Parallel plate fin thickness [14], Heat sink topology by mass addition [15], and mass reduction [16]

From Table 4.3 it should be noted that the studies performed by Bornoff et al. [14-16] are based on thermal bottleneck, a term used to describe heat paths with large thermal resistance. It should also be noted that studies [15] and [16] are not optimization of parallel plate heat sinks. Study [15] involves the successive addition of heat sink material to points of highest temperature, followed by re-simulation to determine if the addition reduced the thermal resistance. The optimized heat sink geometry takes a branched tree-like topology. Study [16] takes the opposite approach, involving successive removal of heat sink material from an initially optimized parallel plate heat sink. The mass removal is systematically based on locations of greatest thermal bottleneck. Bornoff et al. [16], for both forced and natural convection, gave plots for the percent increase in thermal resistance as a function of percent reduction in mass. It was ultimately found that in forced convection there exists a small opportunity of mass reduction with little increase in thermal resistance [16]. However, for forced convection, the surface area available for heat transfer is a dominating factor. For

natural convection it was found that there exists a much greater window for mass reduction with minimal increase in thermal resistance [16].

4.2.1.2 Geometric Considerations:

While parallel plates and pin fins are the most common heat sink topologies, there are many studies that have evaluated the thermal performance of other heat sink designs in addition to the uniquely optimized topology of Bornoff et al. [15, 16]. A significant number of these alternative geometries are evaluated for liquid cooled mircrochannels as a method to reduce pressure drop.

Xie et al. [17] compared traditional rectangular cross section microchannels to longitudinal-wavy microchannels (LWC) and transversal-wavy microchannels (TWC) using numerical simulation for a water-cooled system. It was found that LWC had an improved Nusselt number, however, with this improvement came a greater negative effect of high increase in pressure drop over the traditional straight rectangular microchannel. The LWC proved to have an overall thermal performance inferior to that of the straight rectangular channels. The TWC had a slight decrease in heat transfer coefficient from the straight rectangular channels. However, it did have a significant decrease in pressure drop. With such an improvement in pressure drop, the slight decrease in the heat transfer coefficient did not prevent the TWC from having an overall thermal performance superior to that of the straight rectangular channels. For a thermal resistance of about 0.04 °C/W, the pressure drop in the TWC was only about 20kPa [15]. The pressure drop is an order of magnitude smaller than the previously reported pressure drop by Tuckerman and Pease for straight rectangular channels [18].

Gunnasegaran et al. [19] studied the effect of geometry, the Reynolds number, and heat flux on the pressure drop and convective heat transfer coefficient for straight rectangular, trapezoidal, and triangular microchannels. Using finite volume analysis, it was determined that in general smaller hydraulic diameters provide higher heat transfer coefficients and higher pressure drops as expected, and that pressure drop rises linearly with Reynolds number. Gunnasegaran et al. [16] concluded that the heat transfer coefficient and the Poiseuille number, related to the friction factor, are the

highest for the rectangular microchannels. The rectangular microchannels were seen as the most effective heat sinks, followed by the trapezoidal microchannels.

Luo et al. [20] studied honeycomb microchannel geometry. The honeycombs were set on top of each other to make a porous like media for the fluid to flow through. Luo et al. [20] experimented with brass honeycomb stacked on top of each other. They [20] looked at the heat transfer capabilities with different pipe diameters, different working fluid, and various pumping power using a micro pump. Luo et al. [20] concluded that for water, the system can remove a heat flux of 18.2W/cm^2 at a pumping cost of 2.4W. The experiment was not compared to the traditional straight microchannel set up, however, the dissipated heat flux is considerably less than that reported by Tuckerman and Pease [18] for straight rectangular microchannels. Further investigation into the pumping power to determine the core pressure drop in the heat sink system is needed to make a direct comparison of the honeycomb microchannel geometry to the traditional straight rectangular channels.

Ruiz and Carey [21] experimentally studied the heat transfer and pressure drop of a microchannel with spiraling radial inflow. The heat transfer coefficient of the radial inflow microchannel heat sink are reported as four times higher than for unidirectional laminar fully developed flow through parallel plates.

In addition to the constructal, or branched, heat sink geometry presented by Bornoff et al. [15], there are also studies that look at branched mirchochannel geometries to enable better fluid flow. The constructal principle refers to the idea that the performance of a channeling system is maximized by arranging and balancing flow resistances in a flow system that is allowed to morph [22]. This idea is most commonly focused on a flow system that connects a single point to an infinitely many number of points, similar to tree branches [22].

Bornoff et al. [15] allowed branching based on the flow of heat. However, the same principle can be applied to fluid flow with the expectation of increasing convective heat transfer with minimal pressure drop. Escher et al. [23] analyzed the hydrodynamic and thermal performance of a bifurcating network and compared it to a parallel microchannel cold plate using a one-dimensional model. Unlike previous studies, Escher et al. [23] optimized the geometry based on the available space. It was

found that due to the massive branching of an optimized bifurcating system, the parallel channels provided coolant more effectively to the heat transfer surface area, which in turned enabled better convective heat transfer. Mazloomi et al. conducted a study that showed optimal configuration for transferring heat to a heat sink is achieved with side branches, parallel to main channel, with a large main channel thickness [24].

4.2.1.3 Cutting Edge Heat Sink Designs:

While heat sink geometry and geometry optimization can improve thermal performance, there are some other unique ways in which thermal performance has been improved. Rips et al. [25] presented an idea to induce turbulent flow in commonly narrow, laminar parallel plate channels used in forced convection with the addition of a reed. The reed was placed in a tradition parallel plate heat sink to create flow-induced vibrations. Through simulation it was observed that the reed induced vortex structures, much like an obstruction does. However, the reed had a pressure drop much less than a typical channel obstruction. Turbulent flow increases the convective heat transfer coefficient, which in turn is able to decrease the thermal resistance of the heat sink.

Another technology that has hit the market with some excitement is the Sandia Cooler developed at the Sandia National Laboratory (SNL) [2]. Currently commercially available from a recent start up company, CoolChip™ Technologies, the Sandia cooler combines the fan and the heat sink of an air-cooled system into one component. The Sandia cooler consists of a finned disc-shaped impeller that rotates by a high efficiency brushless motor (Figure 4.13). The impeller pulls air into the center, where there are no fins, and then forces air to be expelled outward through the fins. The rotation of the fins reduces the average boundary layer thickness, and also reduces the effects of fouling due to dust and moisture accumulation. In order to spin with minimal friction, the impeller is suspended above a baseplate by a thin air gap of approximately 10μm [2].

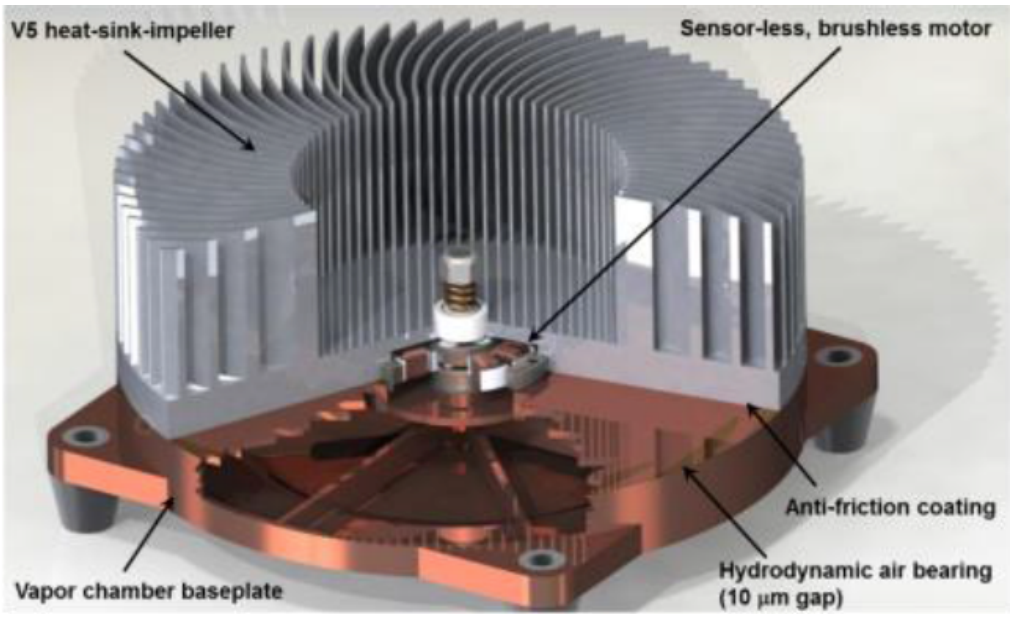

Figure 4.13 - Image from Sandia National Laboratory [2] of the Sandia Cooler.

Unfortunately, the small air gap adds thermal resistance to the overall system. Thermal resistance data from SNL shows thermal resistance values of 0.25 °C/W at 1000 RPM to 0.07 °C/W at 4500 RPM. From the experimental data and simulations published by SNL, the thermal resistance of the Sandia cooler appears to approach 0.05°C/W. For an air gap distance of 10μm, the thermal resistance across this gap is 0.05°C/W [2]. Therefore, the total resistance of the Sandia cooler approaches the resistance of the air gap that is used to suspend the baseplate, ultimately proving to be the limiting thermal resistance of the overall Sandia cooler.

The results presented by SNL are for a 4in diameter cooler [2]. This gives an air gap surface area thermal resistance of 0.628 in^2 °C/W (4.05E-4 m^2 °C/W). The tested thermal resistance values are 0.002 m^2 °C/W at 1000 RPM and 5.68 m^2 °C/W at 4500RPM. An individual MOSFET has an area of 3.36E-4m^2. For a heat sink of this area, an air gap would give a thermal resistance of 1.21 °C/W. For an area of sixteen MOSFETs the air gap would have a thermal resistance of 0.08 °C/W, which is comparable to the full scale Sandia Cooler. Because the Sandia cooler is relatively large, in comparison to individual power MOSFETs, the small air gap does not pose a significant thermal resistance. However, as the area of the heat sink becomes smaller, the thermal resistance of the 10μm gap becomes large. The Sandia Cooler will be

effective for medium to large-scale heat sinking. However, it is likely inappropriate for smaller scale heat sinking.

Another idea that may have progress for certain electronics is the idea of adding phase change material to the inside of pin or plate fins. Yoo and Joshi [26] analyzed thermal performance of a hollowed plate and pin-finned heat sinks filled with Wood's metal (50Bi/27Pb/13Sn/10Cd). In their experiments they simulated transient thermal loads by using periodic power inputs. For fan-cooled heat sinks, phase change material reduced energy consumption by 5.4-12.4% based on the decrease in necessary fan operating time. A decrease in fan use also decreases the audible noise of the device. Because heat sinks are typically designed for worst-case scenarios, in the case of electronics that produce transient thermal loads, such as computer CPUs, use of phase change material could significantly reduce the size of the heat sink. The melting of the phase change core would be able to cover the worst-case scenario thermal load peaks. For power electronics such as MOSFETs, the use of a phase change core heat sink would not provide much benefit, as it does not exhibit transient thermal loads.

4.3 Conclusions:

The research presented here is focused on the development and analysis of thermal solutions for a high-efficiency power conversion unit. The first chapter of this work defines thermal resistance and outlines the basic method of heat sink sizing. The required thermal resistance for the particular power switching devices is calculated based on the parameters given by the electronic device manufacturer.

The second chapter considers how to predict thermal resistance values in parallel plate heat sinks. Analytical correlations developed for convective heat transfer in parallel plates and finite element analysis simulations are compared to experimental results for a finned heat sink. Forced air convection experimental thermal resistance results are found to be within 15% of the simulated and analytical results. The deviation between experimental and simulated results is attributed to incorrect assumption in fluid flow rate, as stagnation zones were observed with the fan during experimental testing.

The analytical correlations for forced convection through parallel plates were extended to systems using helium and water as the working fluid. The thermal resistance results were compared to finite element simulations. Finite element analysis predicted a pressure drop value close to the analytical values for the water-cooled system. The thermal resistance predicted by finite element analysis was considerably higher than that predicted by the analytical correlations. This is not unexpected as the analytical correlations were derived for fluids with Prandlt number approximately equal to unity. While expected to improve the thermal performance of the heat sink with a higher thermal conductivity than air, the helium system was observed using finite element analysis to worsen the thermal performance of the heat sink. The velocity profiles indicated significant flow bypass with the helium system, which decreased the amount of fluid participating in convective heat transfer. The analytical model did not take into account flow bypass and predicted thermal resistance values lower than the air-cooled system.

Finite element analysis simulations were also used to compare results to a well-known microchannel experiment conducted by Tuckerman et al. [18]. The simulations predict thermal resistance values that are lower than the results obtained by Tuckerman et al. It was also observed using finite element analysis that the thermal resistance is not independent of the heat flux contrary to the conclusions drawn by Tuckerman et al. The temperature dependencies of the material properties used in the simulation are found to play a significant role in causing the thermal resistance to be dependent on heat flux. Using finite element simulation, it was also observed that thermal resistance is improved with increased water temperature.

Chapter 3 evaluated the practicability of using thermoelectric generation to recover heat dissipated from electronic components. It was determined that with the current design, heat recovery with thermoelectric generators actually increases the power required. The added thermal resistance caused by integrating a TEG increases the heat transfer needs of the solution. For the case of electronic components, where hot side temperature is limited and must be tightly controlled, heat recovery becomes limited. For the current design with commercial TEGs, an estimated component temperature that would cause energy input into the system to be net zero is determined

to be 170°C, which is 20°C above the maximum junction temperature of the current electronic device. High temperature electronic components may be able to have a heat recovery system. However, further work would need to be conducted to evaluate if the increase in TEG power output is greater than the decrease in device efficiency at high temperatures. For the current power conversion unit, TEG heat recovery would not improve the overall efficiency of the device, and therefore was not pursued further.

The final chapter describes the predicted performance of the heat sink to be used in the prototype energy conversion unit. By incorporating heat dissipating device location with the thermal management solution, a more compact solution is designed. For the final power converter heat sink design, a thermal core approach is taken, cooling the highest heat dissipating devices from the center of the board. This approach was adopted from the 2013 Mac Pro® uniquely compact thermal design. Two different air-cooled heat sinks were developed, built and tested for the power conversion unit prototype, as well as one commercial cold plate design. Simulation and analytical correlation results indicate that all three designs meet the required thermal resistance values calculated in Chapter 1.

References:

[1] G.E. Moore, "Cramming more components onto integrated circuits," *Electronics*, Apr. 1965, vol. 38, no. 8.

[2] T. A. Johnson, J. P. Koplow, W. L. Staats, D. B. Curgus, M. T. Leick, D. Matthew, M. D. Zinnerman, M. Arienti, P. E. Gharagozloo, E. Hecht, N. Spencer, J. W. Vanness, and R. Gorman, "Development of the Sandia Cooler," SNL. Albuquerque, NM. Rep. SAND2013-10712, 2013.

[3] (2017, Apr. 19). *Mac Pro (Late 2013) – Technical Specifications* [Online]. Available: https://support.apple.com/kb/SP697?viewlocale=en_AF&locale=en_AF

[4] (2013, Jan. 15). *Mac Pro (Mid 2012)-Technical Specifications* [Online]. Available: https://support.apple.com/kb/SP652?locale=en_US

[5] The Engineering ToolBox, "Convective Heat Transfer," [Online]. Available: http://www.engineeringtoolbox.com/convective-heat-transfer-d_430.html. [Accessed: Jan. 2017].

[6] P. Teertstra, M. M. Yovanovich, J. R. Culham, T. Lemczy, "Analytical Forced Convection Modeling of Plate Fin Heat Sinks." *5th IEEE SEMI-THERM Symp.,* 1999, pp. 34-41.

[7] J.R. Culham, Y.S. Muzychka, "Optimization of Plate Fin Heat Sinks Using Entropy Generation Minimization". *IEEE Trans. Compon. Packag. Technol.,* vol. 24, no. 2, pp. 159-165, Jun. 2001.

[8] R. Bons. Siemens Webinar, Topic: "Best practices for forced & natural convection cooling simulation," Dec. 15, 2016.

[9] Meshing Reference Manual, "Boundary Layers," COMSOL Multiphysics® v. 5.1. COMSOL AB, Stockholm, Sweden. 2015.

[10] Materion, "Ceramics Material Properties Chart," BW3250, [Revised Oct. 2014].

[11] W. Elenbaas, "Heat Dissipation of Parallel Plates". *Physica IX*, no. 1, pp. 1-28, Jan. 1942.

[12] E.K. Levy, "Optimum Plate Spacing for Laminar Natural Convection Heat Transfer From Parallel Vertical Isothermal Flat". *J. Heat Trans-T ASME,* pp. 463-465, Nov. 1971.

[13] S. Lee. "Optimum Design and Selection of Heat Sinks," *IEEE Trans. Compon. Packag. Manuf. Technol.*, vol. 18, no. 4, pp. 812-817, Dec. 1995.

[14] R. Bornoff, B. Blackmore, J. Parry, "Heat Sink Design Optimization Using the Thermal Bottleneck Concept." *27th IEEE SEMI-THERM Symp.*, 2011, pp. 76-79.

[15] R. Bornoff, J. Parry, "An Additive Design Heatsink Geometry Topology Identification and Optimization Algorithm." *31st IEEE SEMI-THERM Symp.,* 2015, pp. 303-308.

[16] R. Bornoff, J. Wilson, J. Parry, "Subtractive Design: A Novel Approach to Heatsink Improvement." *32nd IEEE SEMI-THERM Symp.,* 2016, pp. 198-205.

[17] G. Xie, J. Liu, Y. Liu, B. Sunden, W. Zhang, "Comparative Study of Thermal Performance of Longitudinal and Transversal-wavy Microchannel Heat Sinks for Electronic Cooling", *J. Electron. Packaging*, vol. 135, Jun. 2013.

[18] D.B. Tuckerman, R.F.W. Pease, "High-Performance Heat Sinking for VLSI". *IEEE Electron Device Lett.,* vol. 2, no. 5, pp. 126-129, Mar. 1981.

[19] P. Gunnasegaran, H.A. Mohammed, N.H. Shuaib, R. Saidur, "The effect of geometrical parameters on heat transfer characteristics of microchannels heat sink with different shapes", *Int. Commun. Heat Mass,* vol. 37, pp. 1078-1086, 2010.

[20] X. Luo, Y. Liu, W. Liu, "A Honeycomb Microchannel Cooling System for Microelectronics Cooling", *Heat Transfer Eng.*, vol. 32, no 8, pp. 616-623, 2011.

[21] M. Ruiz, V. P. Carey, "Experimental Study of Single Phase Heat Transfer and Pressure Loss in a Spiraling Radial Inflow Microchannel Heat Sink," *J. Heat Trans-T ASME*, vol. 137, Jul. 2015.

[22] A. Bejan, S. Lorente, "Constructal Tree-shaped flow structures", *Appl. Therm. Eng.*, no. 27, pp. 755-761, 2007.

[23] W. Escher, B. Michel, D. Poulikakos, "Efficiency of optimized bifurcating tree-like and parallel microchannel networks in the cooling of electronics", *Int. J. Heat Mas. Trans.*, no. 52, pp. 1421 -1430, 2009.

[24] A. Mazloomi, F. Sharifi, M.R. Salimpour, A. Moosavi, "Optimization of highly conductive insert architecture for cooling a rectangular chip", *Int. Commun. Heat Mass*, no. 39, pp. 1265-1271, Jun. 2012.

[25] A. Rips, K. Shoele, A. Glezer, R. Mittal, "Efficient Electronic Cooling via Flow-Induced Vibrations", *33rd IEEE SEMI-THERM Symp.,* 2017, pp. 36-39.

[26] D. Yoo, Y. K. Joshi, "Energy Efficient Thermal Management of Electronic Components Using Solid-Liquid Phase Change Materials," *IEEE Trans. Device Mater. Rel.*, vol. 4, no. 4, pp. 641-649, Dec. 2004.